

2)

ANALYSES OF FAILURES OF FILLET WELDS

by

LI LIANG

B.S., Mechanical and Manufacturing Engineering
Beijing University of Aeronautics and Astronautics, Beijing, P.R. China
1988

Submitted to the Department of OCEAN ENGINEERING
in Partial Fulfillment of the Requirements for the Degree of

MASTER OF SCIENCE IN OCEAN ENGINEERING

at the

MASSACHUSETTS INSTITUTE OF TECHNOLOGY

FEBRUARY 1997

Copyright, ©Massachusetts Institute of Technology

Signature of Author _____
Department of Ocean Engineering
January, 1997

Certified by _____
Professor Koichi Masubuchi
Department of Ocean Engineering, Thesis Supervisor

Accepted by _____
Professor Kim J. Vandiver
Chairman, Committee for Graduate Studies

MASSACHUSETTS INSTITUTE
OF TECHNOLOGY

APR 29 1997

Eng.

LIBRARIES

Analyses of Failures of Fillet Welds

by

Li Liang

Submitted to the Departments Ocean Engineering
February, 1997, in partial fulfillment of the
requirements for the degree of
Master of Science in Ocean Engineering

Abstract

This thesis studied plastic failures of fillet welds in ship structures. Different rupture modes were studied separately. Purposes of the analyses were to simulate the failures of fillet welded ship structures which are subjected to extreme plastic deformations caused by collision or grounding accidents.

The numerical study of plastic failure of a cruciform fillet weld under tension was performed by finite element method (FEM) using ABAQUS software. The inhomogeneous material properties which are caused by welding heat affect were approximately simulated by hardness measurement. For the FEM model, the input contour line of the weld was made by measuring the fusion line from an etched specimen macro-photo.

In three point bending tests, with the pictures obtained from the video microscope and the video printer, the tearing work per unit length of the fillet weld was calculated. Also, the strain concentration factor of the end fillet weld caused by the geometry discontinuity of the end fillet weld and the undercut defect was studied. The tearing criterion of the end fillet weld around the pedestal on the base plate was calculated as a function of the deformed curvature of the base plate.

Thesis Supervisor: Koichi Masubuchi

Title: Professor of Ocean Engineering and Materials Science

Acknowledgment

I would like to express my deepest gratitude to my advisor, Professor Koichi Masubuchi, for his advice and support throughout the study. His practical insight in engineering and professional seriousness in research have been inspiring and will always be.

I also want to thank Professor Frank A. McClintock, for his enthusiastic support and encouragement in theory development.

My appreciation also goes to the sponsors of the Tanker Safety Program and Oil Tanker Side Collision Program. With their generous support, I was able to finish this thesis with two reports.

Thanks go to my laboratory mates Mr. Hideki Shimizu, Mr. Yunchin Hsiao, Mr. David Walworth, Lt. Athanasios G. Sampos, Mr. Eko Kuswanto, Lt. Robb Wilcox, Ms. Regina Midaugh, Ms. Juliana Atmadja, Mr. Akira Umekumuni, Mr. Akira Yamamoto, and Dr. Gokhan Goktug, for the friendship and fun we shared at the welding system laboratory. Their encouragement and help are priceless in the limited period of my staying at MIT. I am grateful to Mr. Tony Zona, our beloved technician, for his tremendous help in the research projects.

My special thanks go to Ms. Danielle Guichard-Ashbrook, the assistant dean of the international student office, for helping me pulling through the hard time in my life.

My gratitude goes to my dear parents, for their constant love and encouragement.

Table of Contents

Abstract	2
Acknowledgments	3
Table of Contents	4
List of Figures	7
List of Tables	9
Chapter 1 Introduction	10
1.1 Background.....	10
1.2 Objectives and Approaches.....	14
1.3 Organization of thesis.....	16
Chapter 2 Analysis of Cruciform Fillet Weld under Tension	17
2.1 Overview.....	17
2.1.1 Background.....	17
2.1.2 Basic approaches.....	18
2.2 Cruciform Fillet Weld under tension test Description.....	18
2.3 Material Properties Supporting Data.....	19
2.3.1 Power-law fitting of the uniaxial tensile test of EH 36 carbon steel from data of Kawasaki Heavy Industries.....	19
2.3.2 Hardness measurement.....	21
2.4 Calculation.....	22
2.5 Conclusions.....	23
Chapter 3 Tearing Work of the Side Fillet Weld	29
3.1 Overview.....	29
3.2 Theories Applied.....	29
3.3 Experiment Description.....	33

3.3.1 Specimen preparation and instrumentation.....	33
3.3.2 Experimental recording.....	35
3.3.3 Post failure specimen examination.....	37
3.4 Calculations.....	38
3.4.1 Calculation of R_c from load vs. displacement data.....	38
3.4.2 Calculation of R_c from post failure measurement data.....	39
3.5 Conclusions.....	40

Chapter 4 Strain and Stress Concentration Analysis of the End Weld with an Undercut Defect.....	55
4.1 Overview.....	55
4.2 Theories Applied.....	56
4.2.1 Linear elastic fracture mechanics.....	56
4.2.2 Dynamic fracture.....	58
4.2.3 Elasto-plastic fracture mechanics (EPFM).....	60
4.3 Experiment Description.....	63
4.3.1 Specimen preparation and instrumentation.....	63
4.3.2 Experiment observation.....	65
4.4 Calculations.....	66
4.5 Conclusions.....	68

Chapter 5 An Analysis of the Plastic Failure of the Base Plate near the End Fillet Weld.....	78
5.1 Overview.....	78
5.2 Theory Applied.....	79
5.2.1 Bending and tension combined load vs. pure bending moment	79
5.2.2 Tearing of the base plate at the web end.....	80
5.2.3 Low cycle fatigue for repeated loading.....	84
5.3 Experiment Performance.....	84
5.4 Calculations.....	87

5.5	Conclusions.....	89
Chapter 6	Conclusions and Recommendations.....	98
	References.....	101
	Appendices.....	110
	Appendix 1 Literature Review.....	110
	Appendix 2 Experiment Description.....	113
	Appendix 3 Calculation (Computer programs etc.)	118
	Appendix 4 Experiment Records.....	123

List of Figures

Figure 2-1	Cruciform testing specimen subject to tensile load.....	24
Figure 2-2	Computer simulated stress strain relation curve of EH36 steel.....	25
Figure 2-3	The hardness measurement of a weldment showing a narrow HAZ.....	26
Figure 2-4	The contour line measured from the specimen No. 6.....	27
Figure 2-5	An FEM model of the specimen No. 6.....	28
Figure 3-1	TWB specimen test configuration.....	41
Figure 3-2	Wide plate bending specimen dimension drawing.....	42
Figure 3-3	Slip line fields, crack tip opening displacement for initiation, $CTOD_i = u_i$, and alternating cracking and sliding off during growth to final separation at u_f	43
Figure 3-4	Geometry and definitions of a fillet weld	44
Figure 3-5	Control volume for the critical tearing work per unit length R_C in peeling.....	45
Figure 3-6	Peeling of an elastoplastic metal epoxy joint by an end force	46
Figure 3-7	Peeling of an elastoplastic metal-epoxy joint by an end couple	47
Figure 3-8	Beveled and unbeveled web.....	48
Figure 3-9	Wide plate bending experiment setup.....	49
Figure 3-10	Comparison of load vs. displacement diagrams of Specimen 1 and Specimen 4	50
Figure 3-11	Schematic drawing of the cracking process of the specimens during tests..	51
Figure 3-12	Post failure pictures of specimen 2.....	52

Figure 3-13	Post failure pictures of specimen 3.....	53
Figure 3-14	Schematic drawing bending moment of the specimen.....	54
Figure 3-15	Specimen 2 and specimen 3 load vs. displacement curves.....	55
Figure 4-1	Cross section of a fillet weld for hardness measurement, with an undercut exist at the vertical toe of the weld.....	69
Figure 4-2	Geometry difference of specimen 5 and specimen 6.....	70
Figure 4-3	Displacement vs. nominal strain for the geometry of the experiments simulated by FEM.	71
Figure 4-4	Definition of J-integral.	72
Figure 4-5	Load displacement diagram for cracked body of non-linear elastic material.....	73
Figure 4-6	Relationship between a surface crack dimensions and equivalent through thickness crack dimension.	74
Figure 4-7	Specimen 5 load vs. displacement curves.	75
Figure 4-8	Specimen 6 load vs. displacement curves.	76
Figure 4-9	Comparison between monotonic and cyclic stress-strain curves for ASTM A-36 structural steel.....	77
Figure 5-1	Specimen setup with the supporting blocks.....	90
Figure 5-2	Pictures of failed specimen 7 with the base plate shearing off at the toe of end weld.....	91
Figure 5-3	Schematic drawing of the base plate shearing off around the pedestal.....	92
Figure 5-4	Combined load of tension and moment diagram.....	93
Figure 5-5	The real case and idealized and model comparison.....	94
Figure 5-6	Load vs. displacement diagram of the test.....	95
Figure 5-7	Schematic drawing of post fracture measurement of specimen 7.....	96
Figure 5-8	Curvature vs. displacement diagram of specimen 7.....	97

List of Tables

Table 2-1	Stress-strain relation of the base metal.....	20
Table 2-2	Tensile strength of the weldment of a cruciform specimen.....	22
Table 3-1	The chemical composition and mechanical specifications of base metal AH-36 and weld metal TGS-50.....	34
Table 3-2	Specimen characteristics of Specimens 1,2,3 and 4.....	35
Table 4-1	Specimen characteristics of Specimens 5 and 6.....	64
Table 4-2	The end fillet weld dimension measurement of Specimen 5 and Specimen 6.....	64
Table 5-1	Dimensional descriptions.....	86
Table 5-2	Specimen 7 material descriptions.....	86
Table 5-3	The input parameters for calculation the coefficients.....	88
Table 5-4	Calculation result of the displacement criterion.....	88

Chapter 1 Introduction

1.1 Background

In the Joint MIT-Industry Project on Tanker Safety, the grounding damage of oil tankers has been extensively studied. Renewed consideration of the crash worthiness of oil tankers has demonstrated the need for the detailed characterization of the fillet welds that join the stiffeners to the hull platings due to grounding loads [Wierzbicki, et al, 1991]. This research program led to a later research program entitled “Rupture Analysis of Oil Tankers in Side Collusion” which was performed for the Volpe National Transportation System Center, the Department of Transportation.

Current fillet weld design standards in ship building industry only ensure safe performance under normal operating conditions. These fillet welds, generally speaking, do not withstand grounding forces [McDonald, 1993]. Investigation of the damages encountered in the grounding of the Exxon Valdez and the data of large-scale grounding tests, performed by Mitsubishi Heavy Industries Ltd., have shown failure of the fillet welds in the damage area. The welding team in the Joint MIT - Industry Project on Tanker Safety has been working to understand the failure of fillet weld and to provide the improvement of weld design.

During grounding accidents, The a ship with stiffeners integrated together with hull platings can take more energy than a ship with the stiffeners apart from the hull platings. Hence, increasing the tearing work or tensile strength of fillet welds so as to

shift the deformation and fracture to the areas away from the fillet welds is desirable in the grounding or collision of a ship. In the mean time, the understanding of initiation of the tearing off of the weldment is crucial to understand the whole process of the plastic rupture of the fillet welded ship structures.

Increasing welding penetration is a promising approach of increasing the strength of fillet welds subjected to tension loading [Masubuchi, 1968]. Commonly, penetration can be obtained by beveling plates. But, beveling plates raises the fabrication cost. Fortunately, penetration without beveling plates can be obtained by alternative methods. Relatively deeper penetration can increase joint strength without adding any weld materials [Wilcox, 1995]. Fifty six cruciform specimens welded by gas metal arc welding (GMA), under different welding parameters, were tested under tension had shown that deeper penetrating welds gave three to four times plastic extension as compared to welds without penetration. By increasing welding current and torch travel speed, a deeper penetration can be achieved without increasing the energy consumed compared with the manufacturer recommended welding parameters [Wilcox, 1995].

In the previous numerical studies on the strength of fillet welds, the geometry of the fillet welds was idealized as a triangle that virtually neglected the existence of penetration. The material was considered to be homogeneous [Atmadjia, 1995]. Both of these assumptions conflict with the real characteristics of fillet weld. Firstly, the materials of weldment are inhomogeneous due to the welding heat involvement. The mechanical properties vary substantially within a narrow region of weldment [Harrison,

JWS]. Secondly, the main purpose of cruciform fillet weld tensile tests is to test the effect of penetration effects on the tensile strength of different specimens that were fabricated by GMA welding under different welding parameters. The numerical model without penetration loses its vigorousness under such an assumption. Calculating the tensile strength without considering the penetration, will give a limit load much less than the test value. The error was about 15% compared with the experiment results as shown in by Atmadjia, 1995. This thesis studied the tensile strength of the cruciform fillet welds with the considerations of changing of material properties of different areas and penetration by inputting the fusion line of the fillet weld as a weld contour line. The fusion line of the fillet weld was measured from the etched macro surface of a slice of the fillet weld of a specimen.

Compared to a butt weld, a fillet weld has larger geometrical discontinuity that results to more severe stress and strain concentration. With a larger stress concentrator, the welded structures may fail in brittle mode that sustain much less energy. Seven relatively wide plate attached with a stiffeners by fillet welds were studied by standard three-point bending test. The test was performed to simulate the most severe situation of loading on still existing fillet weld structures. This relatively small scale test has been desired to predict the plane strain fracture toughness of the fillet weld. The tearing work per unit length R_c of the fillet weld fitted in the formula proved by a much larger scale test to separate the stiffener from the base plate by tearing [Koga, 1992].

Most of the brittle fractures initiated and occurred from and near the defects in the stress concentrated region of a welded structure. After the initiation of small cracks in the

structure, if the structure is subjected to extreme plastic deformation, the already existed cracks may become the source of the ductile fracture. The welding defects, including lack of penetration, undercuts, inclusions, and arc strikes, if located at the stress concentrated region, the combination of these contributions of defects and stress concentration caused by geometry discontinuity prescribes the undesirable fate of the fillet weld structure. To simulate the negative effect of a possible existing undercut, a notch was intentionally machined at the toe of the fillet weld. Theoretically, in the above mentioned the stress and strain concentration region, if the plastic zone size caused by the stress concentrator is larger than the defect size, the linear elastic fracture mechanics (LEFM) cannot be applied [Hagiwara, 1985]. Therefore, the general yielding fracture mechanics is the practical assessment in this thesis.

The plastic failure initiations at different for different weldments and load patterns are different. Three modes of tearing off the base plate from the fillet weld plastically were discussed by McClintock, 1997. The tearing mode of the base plate around a pedestal under the fillet weld at the end of the joint of base plate and the stiffener was studied in this thesis. A critical value of the vertical displacement of the pedestal material under the fillet weld at the end weld was obtained. This critical vertical displacement v_{pec} can be used to judge whether the base plate is going to be torn off or not at a certain curvature of the base plate caused by grounding or collision. Also, design of the weldment can be associated with this critical value because v_{pec} is a function of material parameter with respect of the power law exponent n , the structural dimensions of

the weldment, including the leg-length, the width of the half span between two stiffeners, the thickness of the base plate, and the thickness of the stiffener.

1.2 Objectives and Approaches

Tests are desired to give quantitative design and fitness-for-service data, such as limit load and tear resistance per unit length as a function of welding parameters and resulting leg length and penetration. A numerical computational method offers the advantages in predicting some factors that are difficult to measure accurately and were usually given by roughly approximated in empirical formula.

Finite element method makes it possible to calculate the weld structure with inhomogeneous material in the weldment. By using FEM, the geometry contour of the fillet weld can be accurately simulated as an input function. In this sense, a more realistic model can predict a lower limit load for the cruciform fillet weld under tension for the experiments. In this thesis, several attempts of gradually reducing the number of assumptions were made to check the results respectively. The first attempt was to change the fillet weld contour line only, and still applying the perfect plastic material property for calculation. This output was aimed to get the contribution of the penetration effect. The second trial was to transform the hardness measurement to the flow stress of the material, then extrapolate the mechanical properties of the materials by power-law rule [McClintock, et al, 1966a]. This model had been desired to check the inhomogeneous properties for the calculation.

The tear resistance of fillet welds crucial criterion to judge whether the welds are strong enough to hold the structure membranes together as an integrated structure after the crack initiated at a certain region. The tearing work per unit length of the fillet weld R_c determines the possibility of whether the stiffener plates of an oil tanker are integrated with hull platings, when the hull platings are penetrated by grounding rock or collision.

The studies of the notched wide plate specimen bending, is desired to give the designers and manufacturers of ships the quantitative evaluation of the role of the undercut welding defect. Therefore, industry rules can strictly warn people to avoid the welding defects at the stress concentration region. The weld shape effect was studied with the combined contribution of notch effect of an undercut at the toe of the end weld. FEM calculation of the plastic strain was performed to get an insight of the failure phenomena.

The tearing off of the base plate around the pedestal under the stiffener and the fillet weld was studied. A criterion, the critical vertical displacement of the pedestal v_{pec} , was obtained through experimental and analytical studies. This criterion was formulated as a function of the material power law exponent n and dimensions of the weldment. These dimensions include the thickness of the base plate t , the thickness of the web (stiffener) t_w , the horizontal leg-length of side fillet weld d , the width of the plate w . With the vertical displacement v_{pe} known as an important function, the curvature κ of the

base plate of the ship structure upon grounding or collision accidents is related to the failure of a certain kind of fillet welds which have sudden ends.

1.3 Organization of thesis

Chapter 2 focuses on the analysis of cruciform fillet weld under failure under tension. Chapter 3 focuses on the tearing work of the plated bending test. Chapter 4 discusses the effect of welding defect - undercut on the bending test. Chapter 5 studies the initiation of the tearing off of the base plate at the toe of the end fillet weld of the fillet welded structure. Chapter 6 draws conclusions on the failure studies of fillet welds. Relevant figures are attached to the end of each chapter. At the end of thesis Appendices are included

- Appendix 1 Literature survey
- Appendix 2 Experimental description
- Appendix 3 Calculation (computer programs, etc.)
- Appendix 4 Experimental results.

These appendices should be useful for those people who are interested in studying further details.

Chapter 2 Analysis of Cruciform Fillet Weld under Tension

2.1 Overview

2.1.1 Background

In the Joint MIT - Industry Project on Tanker Safety, the grounding damage of oil tankers has been extensively studied. The better understandings of fillet welds performance are needed. Investigation of the damages encountered in the grounding of Exxon Valdez and the data provided by Mitsubishi Heavy Industries' large-scale grounding tests have shown failure of the fillet welds in damage area. The welding team in the Joint MIT - Industry Project on Tanker Safety has worked to the understanding and the improvement of weld design.

Different methods can be applied to increase the strength of fillet weld under tension load. These methods are mentioned by Masubuchi. 1968. They are increasing the welding material strength, increasing weld sizes and increasing the penetration of a weld. Different regulatory agencies allow various amount of leg length reduction with the penetration increased. Usually in industries, penetration is obtained by beveling plates which will take more labor and material costs. However, penetration can be obtained without beveling plates by another method. Relatively deeper penetration can increase joint strength without adding substantial weld materials. More than 50 cruciform specimens welded under different welding parameters were tested under tension have shown that deeply penetrating welds showed three to four times plastic extension as compared to welds without penetration. By increasing welding current and torch travel speed, a deeper penetration can be achieved without increase the energy consumed compared with the manufacturer recommended welding parameters. [Wilcox, 1995].

From the experimental analyses, we are not very clear about the failure process that is the crack propagation procedure in the welds. By studying the macro fractograph or simply the failure surface of a tested specimen, it is hard to get more detailed

information of the crack propagating process before the crack makes the structure fail. In order to have some insight view of the failure mechanism of those fillet welds, a numerical method is used to get the information of crack initiation and propagation process. In this chapter, the failure test of specimen No. 6 from Wilcox tests [Wilcox, 1995] as a simulation prototype model was chosen because it has the optimal combination of strength and energy consumed to fabricate it.

2.1.2 Basic approaches

In the previous numerical studies of the fillet welds, the geometry of the fillet welds had been idealized as a triangle that neglecting penetration [Atmadjia, 1995] and the materials of base plates and weld had been assumed to be homogeneous. These assumptions are not appropriate for the study of the fillet welds when penetration and welding parameters that greatly affect the geometry and the materials of both weld metal and heat-affected-zone (HAZ) when mechanical properties are considered. By connecting hardness measurement to the mechanical properties of the fillet welds [Middaugh, 1995] and measuring the fusion line of the specimen No. 6, an FEM simulates the test more closer to the reality.

2.2 Cruciform Fillet Weld under Tension Test Description

Ideally, people want to perform a test on smaller scale than the real case. However, due to the metallurgical and geometric complexity of a fillet weld, a small scale test may not accurately interpret the actual fracture behavior of large welds. Thus, cruciform fillet tests were thus performed in real scale by Lt. Robb Wilcox. Figure 2-1 shows the dimensions of a tested specimen.

Test Materials

Base plate: EH-36 $t_b=25\text{mm}$ $B=127\text{mm}$

Weld metal: EXCEL-ARCO 71 flux cored wire

2.3 Material Properties Supporting Data

2.3.1 Power-law fitting of the uniaxial tensile test of EH36 carbon steel from experiment data of Kawasaki Heavy Industries

The true stress-strain relationship of the base metal EH-36 low-alloy carbon steel that the specimen were made from based on the Swift power-law

$$\sigma = \sigma_1(\varepsilon_0 + \varepsilon_p)^n \quad 2-1$$

From the experimental data obtained from Kawasaki Heavy Industries (Appendix-4), we can get the yield strength **YS**, tensile strength **TS**, and the uniform strain ε_u at tensile strength σ_u . The Yield strength **YS** is calculated as

$$YS = \sigma_1 \varepsilon_0^n \quad 2-2$$

Under necking condition, $dP=0$, thus the tensile strength is

$$\sigma = \frac{d\sigma}{d\varepsilon} \quad 2-3$$

Substitute Eqn. 2-1 into Eqn.. 2-3, we obtain

$$n = \varepsilon_u + \varepsilon_0 \quad 2-4$$

Knowing that tensile strength **TS** is the force divided by the original area, we have

$$TS = \frac{P}{A_0} = \frac{P}{A} \times \frac{A}{A_0} \quad 2-5$$

where $\log(A/A_0)$ is the uniform strain ε_u at σ_u . Here, we have the tensile as

$$TS = \sigma_1(\varepsilon_u + \varepsilon_0)^n e^{-\varepsilon_u} \quad 2-6$$

From Eqn. 2-2 and Eqn. 2-6, we obtain

$$\frac{TS}{TY} = \left(\frac{\varepsilon_u + \varepsilon_0}{\varepsilon_0}\right)^{\varepsilon_u + \varepsilon_0} e^{-\varepsilon_u} \quad 2-7$$

Applying Eqn. 2-7, we can solve ε_0 . Consequently, we use Eqn. 2-4 and Eqn. 2-6 to calculate **n** and σ_1 out respectively.

Based on the experiment data provided by Kawasaki Heavy Industries (Appendix -4), The material properties can be assumed as: $\varepsilon_0=0.014$, **n**=0.184, and $\sigma_1=705$ GPA. Equation 2-8 gives the numerical approximation with these parameters

$$\sigma(\varepsilon) = 705 * (\varepsilon + 0.0014)^{0.184} \quad 2-8$$

The tabular input material mechanical property (Table 2-1) is calculated based on Eqn. 2-

8. And Figure 2-2 shows draw fitted power-law of stress-strain curve.

Table 2-1 stress-strain relation of the base metal.

ε	$\sigma(\varepsilon)$	$\varepsilon_{pl}(\varepsilon)$
0.002	329.67	$4.301 \cdot 10^{-4}$
0.012	360.476	0.01
0.022	382.72	0.02
0.032	400.377	0.03
0.042	415.134	0.04
0.052	427.876	0.05
0.062	439.128	0.06
0.072	449.231	0.07
0.082	458.416	0.08
0.092	466.851	0.09
0.102	474.659	0.1
0.112	481.937	0.11
0.122	488.757	0.12
0.132	495.179	0.13
0.142	501.253	0.14
0.152	507.016	0.15
0.162	512.502	0.16
0.172	517.74	0.17
0.182	522.753	0.18
0.192	527.562	0.189
0.202	532.183	0.199
0.212	536.633	0.209
0.222	540.925	0.219
0.232	545.072	0.229
0.242	549.083	0.239
0.252	552.968	0.249
0.262	556.735	0.259
0.272	560.393	0.269
0.282	563.948	0.279

2.3.2 Hardness measurement

The Vickers hardness value H_v is obtained by dividing the load P on an indenter in kilograms by the contact area A_c of the impression in mm^2 , which can in turn be found from the diagonal d of the pyramid [McClintock et al, 1966]

$$H_v = \frac{P}{A_c} = \frac{1.8544P}{d^2}. \quad 2-9$$

We can approximate the tensile strength of the material using the relationship of hardness and tensile strength. This simple relationship, defined by McClintock et al, 1966, is suitable for perfect plastic material and can be used as an assumption of our weld metal and heat-affected-zone (HAZ) calculation. The relation is expressed simply as

$$TS(\text{ksi}) = 0.3 H_v. \quad 2-10$$

This is only a rough assumption of the material, ignoring the strain hardening effect of the material and assumes the material to be homogeneous. ASTM standards do not recognize it as an official conversion between hardness and tensile strength [ASTM 1994]. However, due to the difficulty of measuring the tensile strength in micro-scale, despite the imprecise nature of the hardness and tensile strength relationship, the hardness measurement still offers us an accessible approach for the detailed examination of weld and its vicinity areas. This micro-scale measurement is suitable for the finite element method when material has to be divided into dimensions.

From the data provided by Regina Middaugh, 1995, we can approximate the weld region into three areas. Namely, weld metal, base metal and heat-affected-zone (HAZ) (Figure 2-3). The weld metal has the hardness range from 270 to 332. The base metal has the hardness range from 185 to 222. The HAZ which here is simply considered as the small area extended from the fusion line to the base metal has the hardness range from 315 to 497. This area is the most complex area in microstructure of the material. And it has the highest hardness. In plastic analysis, however, because this area is very narrow and has much higher yield strength according to Eqn. 2-10, and the deformation is rather small, we can assume these three areas to be locally homogeneous and have uniform hardness. The assumption was made as follow :

hardness of base metal is 200, hardness of weld metal is 300, hardness of HAZ is 400. Based on the assumption. The tensile strengths of the materials are given as in Table 2-2.

Table 2-2 Tensile strength of the weldment of a cruciform specimen.

	HAZ	Weld metal
Base metal	120	90

2.4 Calculation

FEM geometry models were made by taking the advantage of symmetry of the cruciform specimen structure. The middle plane of the middle plate which was not clutched by the tension machine was “cut” in the middle.. The purpose of doing this is to save the calculation resource of a computer. The clutched plate could also be cut in the middle as symmetric reasons. However, the boundary conditions of that middle plane is not easy to define. So the cruciform specimen turned to a T form. And this middle plane we defined is fixed in 1,2,3,4,5,6 axes as boundary conditions. The weld contour lines were inputted by the fusion line measured from polished micro picture of the specimen No. 6 (Figure 2-4). The right side and left side of fillets were assumed exact same which in actual case there was a slight difference. A two dimensional (2-D) geometry model thus was built. In the weld, the elements was generated according to the grain growing direction. This approach will take metallurgical factors into consideration, although it was tedious to make a mesh like that. The material properties were inputted by field option which allowed none-linear plastic behavior of the material. Three models were run. First model just consider the weldment as a homogeneuos material. The result showed that the fracture path was in the weld. The second model assumed the material of the weld and the base metal were different. However, because the weld metal is softer than the base metal the fracture path was further moved to the fillet weld. The fact is the real fracture path of the specimen No. 6 test was moved to the base metal due to the penetration. And it took large force to break the specimen than the FEM models mentioned above. The FEM models consider the load pattern as displacement of the

clutched end of the specimen. After this calculation, the third model which considers the HAZ hardening effect was made. The HAZ area was approximately assumed to be just one element away from the fusion line which is not very accurate in this case. However, the calculation showed a satisfactory result. Figure 2-6 shows the von Mises plastic stress contour distribution of this model.

2.1 Conclusions

The FEM model can be used to calculate the plastic stress and strain field of the specimen in case the model is appropriately built. The consideration of the geometry of the weld contour line is crucial when the penetration is taken into account. The material properties is only an approximation. Micro scale properties of the material near the weld are needed. However, this will involve much more research than a middle scale project can afford. Due to the complexity brought by the welding process, it is still difficult to scale down the behavior of a weld. More fundamental research is needed.

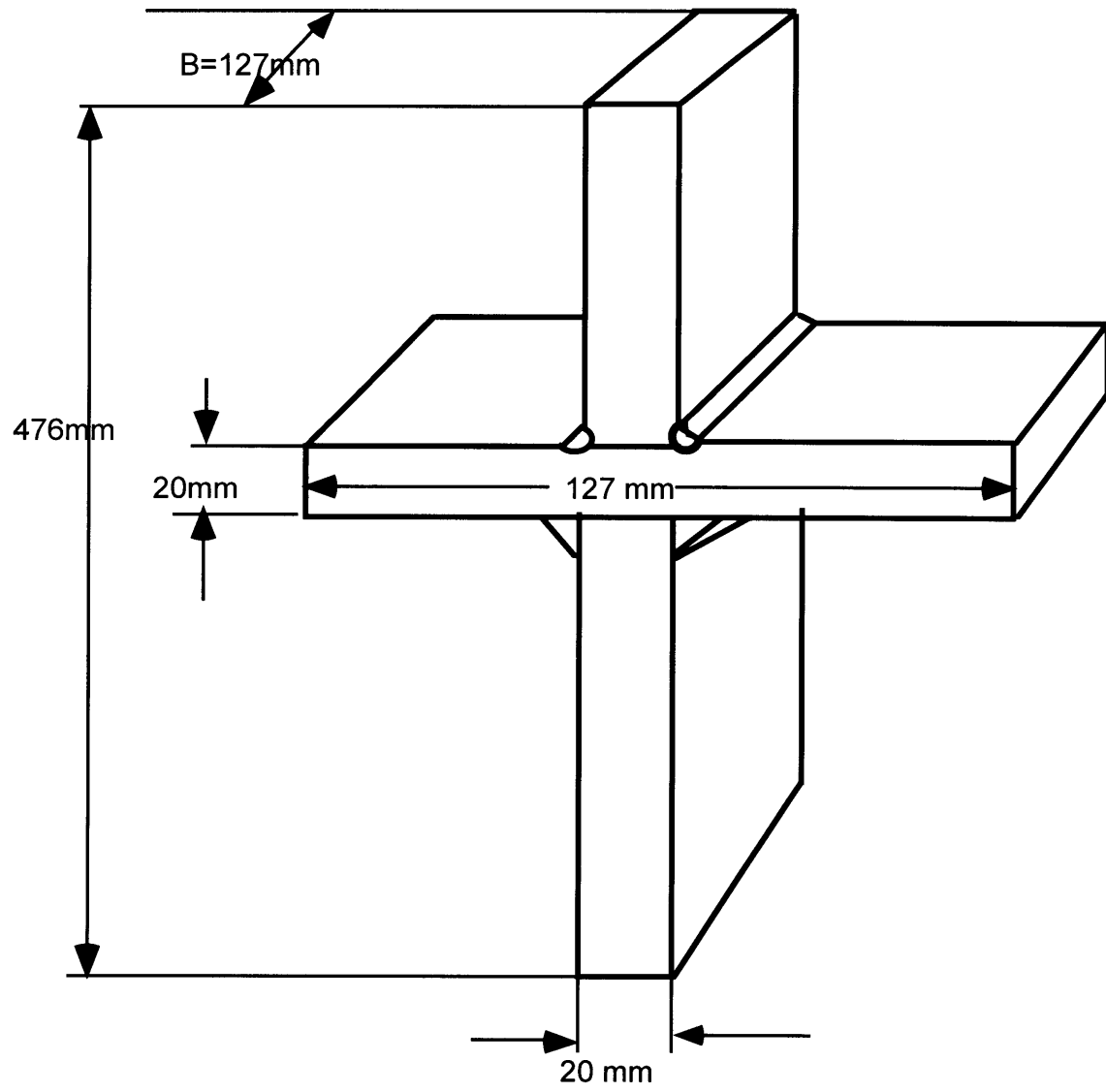


Figure 2-1 Cruciform testing specimen subject to tensile load [Wilcox,1995].

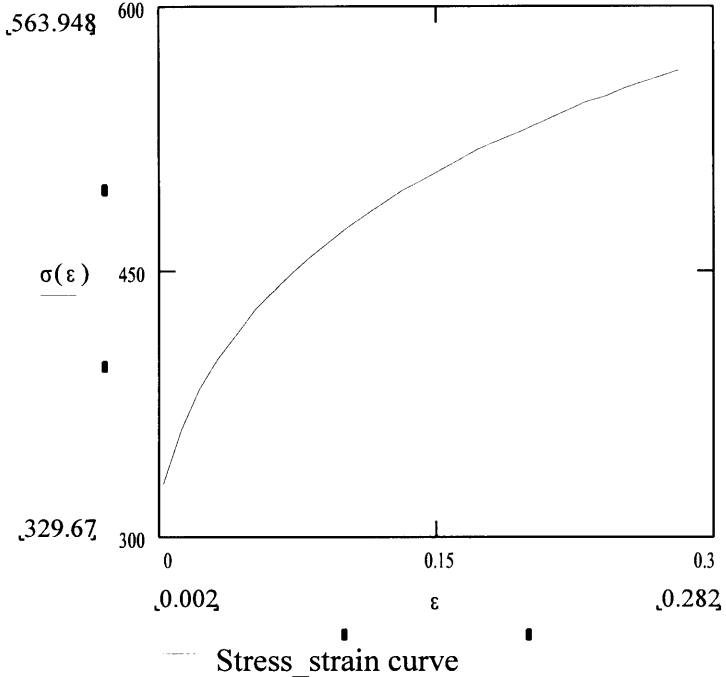
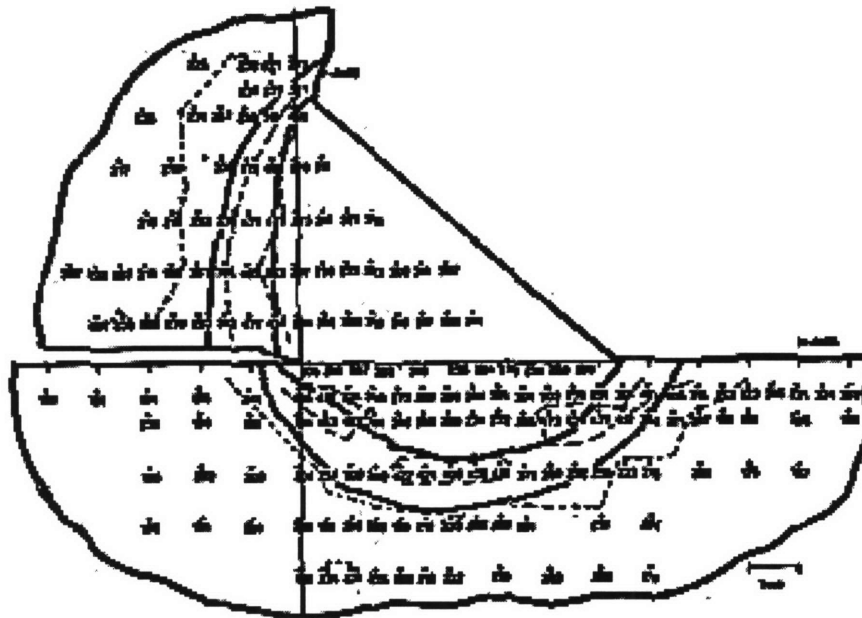


Figure 2-2 Computer simulated stress strain relation curve of EH36 steel.

Vicker's Microhardness Measurements for a Common Shipping Steel Welded with an E7016 Electrode



The weld metal is relatively homogeneous in the weld region. This behavior does not include the weld HAZ. For more information about this microhardness research, please refer to:

Figure 2-3 The hardness measurement of a weldment showing a narrow HAZ.

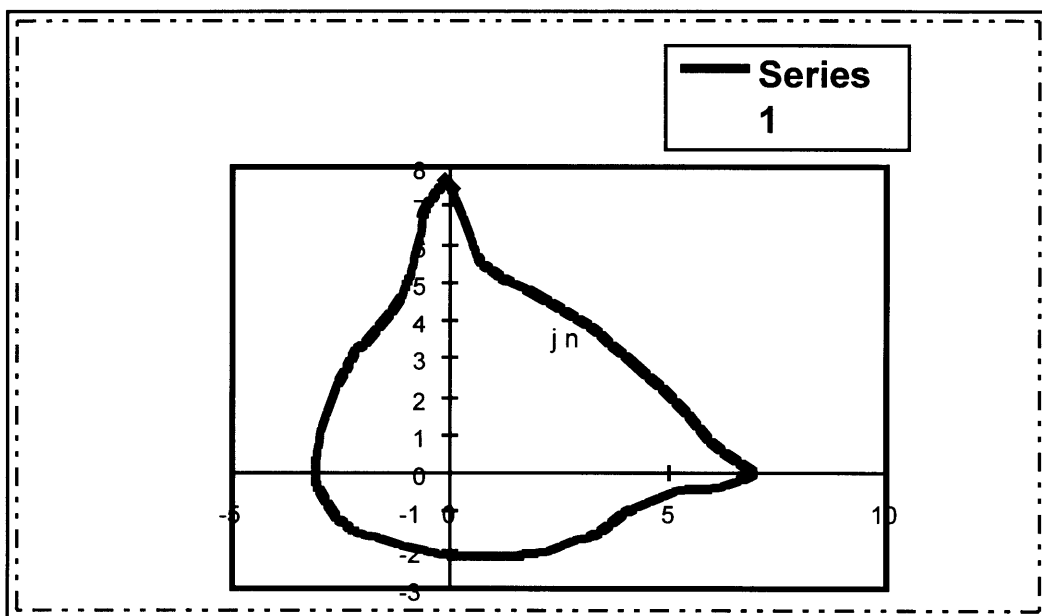


Figure 2-4 The contour line measured from the specimen No. 6.

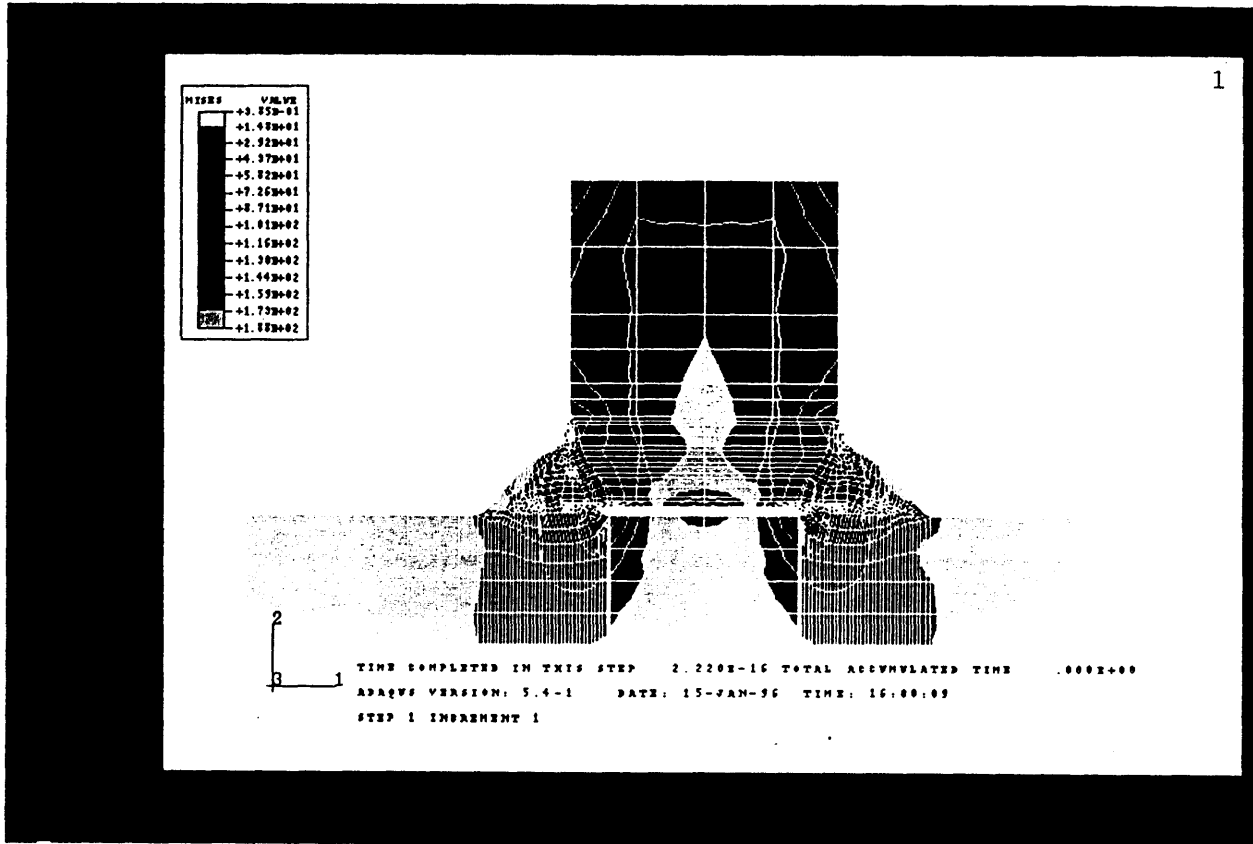


Figure 2-5 An FEM model of the specimen No. 6.

Chapter 3 Tearing Work Per Unit Length of the Side Fillet Weld R_c

3.1 Overview

This chapter is aimed at calculating the tearing resistance of fillet welds by relatively small scale tests. Three-point-bending-test data of Specimen 2 and Specimen 3 were used in calculations.

As discussed in chapter 2 (Figure 2-1), tearing is one of the most important fracture modes of T-joints found in service especially during accidents. The peeling of the stiffeners from hull platings, or vice versa, is important in estimating the amount of damage that would occur upon grounding or collision of an oil tanker. Substantial studies have been performed by the team of the MIT-Industry Tanker Safety Program. The tearing work per unit length R_c has proved to be one of the key criteria in analysis of the mechanism of the peeling of the fillet weld [Kirkov, 1994].

In the tanker safety report (TSR) #29, Kirkov performed experiments on the transversely welded beam (TWB) specimens. Specimen configuration is shown in Figure 3-1. However, this experiment requires large capacity bending machine and not intuitively simulate the tearing the base plate from the stiffener phenomenon.

Tearing work per unit length R_c was studied in this experiment. Specimen 2 and Specimen 3 which have different weld sizes were tested simply by a three point bending test of a wide plate with a reinforcement of a web joined by fillet weld. Figure 2-2 shows the configuration of the specimen. Two approaches were tried to calculate the tearing work per unit length R_c . And the results are within 3% difference. This experiment was proved to be practical in studying R_c in a relatively small scale test.

3.2 Theories Applied

The slip line analysis is frequently used in analyzing the plastic failure problems. It is based on the ideas of the material blocks of the structures would slide along a certain orientations which the stress of shearing in the term of K reaches yield. Figure 3-3 gives the slip line fields of an idealized situation that no penetration of is made on the double fillet welded structure.

By using the slip line field theory the plastic failure path of a two-sided fillet weld may be predicted. Slip lines represent the orientations of maximum shear in a stress field, along which deformation is expected to occur. Considering a T-joint in tension and using the upper bound theorem a limit transverse load that will ensure the weld deformation can be calculated.

Such solutions have been obtained for homogeneous, non-hardening fillet welds with arbitrary crack tips and weld angle [McClintock, TSR 26]. For the special case of the 45° weld angle the limit load per unit length is given by

$$P_L = 2kd, \quad 3-1$$

where k is the shear strength of the weld and d is the minimum leg length (Figure 3-4). In fracture mechanics, k is approximated by: $k = TS / \sqrt{3}$, where TS is the tensile strength of the weld metal. Experimental results have shown that a value of $k = 0.75 \cdot TS$ gives a better approximation in the case of the fillet welds, reflecting the effect of plastic instability absence [Krumpfen, 1983].

The tearing resistance of a fillet weld can be determined by the work required by a transverse load to cause separation of the web from the base plate, normalized per unit length of the fractured weld. Assuming negligible elasticity effects, the ideal work per unit length can be estimated as

$$R_{ideal} \approx 1/2 P_L d = kd^2 \quad . \quad 3-2$$

This work is ideal, since, besides plastic sliding, fracture also takes place and slip occurs at an angle to the vertical. Assuming that cracking initiates at a displacement u_i and fracture is completed at a displacement u_f , the fracture work per unit length ("tearing resistance") can be approximated by

$$R_C = P_L(u_i + u_f)/2 \equiv P_L u_c, \quad 3-3$$

where

u_c is defined as an effective critical displacement (Figure 3-3)
[McClintock, TSR26].

Regarding the peeling fracture of a double sided fillet weld the control volume of Figure 3-5 can be considered. Assuming that a critical bending moment M_C is applied, resulting to a critical curvature κ_C , then as an element material moves by δL the slope changes by $\delta\theta$. The work that the moment does is $M_C \delta\theta = M_C \kappa_C \delta L$. Assuming that there is little interaction between the work to bend the plate and that to tear the weld. Then, as in McClintock, TSR 26, we have

Total work = Plate bending work + Weld tearing work,

$$M_C \kappa_C \delta L = \left(\int_0^{\kappa_C} M d\kappa \right) \delta L + R_C \delta L ; M_C \kappa_C = \int_0^{\kappa_C} M d\kappa + R_C \quad . \quad 3-4$$

From this the tearing resistance can be found

$$R_C = M_C \kappa_C - \int_0^{\kappa_C} M d\kappa = \int_0^{\kappa_C} \kappa dM \quad . \quad 3-5$$

Peeling fracture has been investigated based on the idea of an elastic-perfectly plastic beam glued on a rigid block. Chang et al. considered an end force loaded beam (Figure 3-6), whereas Atkins and Mai [Atkins et. al., 1987] assumed an end-couple

loading (Figure 3-7). Both of those works result to closed form solutions of the fracture work which can be adapted to the case of peeling fracture.

The tearing resistance of a fillet weld for an end loaded beam is

$$R = \left[\begin{array}{l} \frac{\sqrt{2}(1-\nu^2)b^{1/2}\sigma_Y^{3/2}Pl}{3E\sqrt{6\sigma_Y bh^2 - 3Pl}} - \frac{\sqrt{2}(1+8\nu^2)b^{3/2}\sigma_Y^{5/2}h^2}{6E\sqrt{6\sigma_Y bh^2 - 3Pl}} \\ - \frac{\sqrt{2}(11+16\nu^2)}{36E}\sqrt{6\sigma_Y bh^2 - 3Pl}b^{1/2}\sigma_Y^{3/2} + \frac{(1+2\nu^2)b\sigma_Y^2 h}{E} \end{array} \right], \quad 3-6$$

where

P is the end load,

l is the length of the beam plus the crack length,

b is the half beam width,

h is the half beam height

and σ_Y , E and ν the flow stress (yield strength), Young's modulus and elastic Poisson's ratio of the beam material.

The formula is valid when

$$2\sigma_Y bh^2 > Pl \geq \frac{4}{3}\sigma_Y bh^2. \quad 3-7$$

For the moment loaded case, which actually corresponds to that described also by McClintock in TSR26, fracture occurs under a critical moment

$$M_C = (Bh^2\sigma_Y) \left[1 - \frac{3}{4} \left(1 - RE/\sigma_Y^2 h \right)^2 \right], \quad 3-8$$

so,

$$R_C = (Bh\sigma_Y^2 / E) \left[1 - \sqrt{\frac{4}{3} \left(1 - M_C / B\sigma_Y h^2 \right)} \right], \quad 3-9$$

where

B is the full beam width.

This formula is valid for

$$M_C \leq B\sigma_y h^2 = M_L, \quad 3-10$$

where

M_L represents a limit bending moment where plastic collapse of the base plate precedes fracture.

3.3 Experiment Performance

3.3.1 Specimen preparation and instrumentation

AH36 base plates of 3/8" (9.5mm) thick and the web plates of 20mm or 9.5 mm thick were cut to desired dimensions in the machining shop at MIT. The chemical composition and mechanical specifications of AH36 are listed in Table 3-1 [ABS, 1985]. Also, see Fig. 3-2 for the details of specimen dimensions. Because the ductile strength of a weld is mainly determined by the weld size and penetration, deeper penetration can give a stronger weld [Wilcox. TSR50]. In this experiment, the penetration had been experimentally controlled by beveling the web before welding was performed. See Figure 3-8 for the beveled and unbeveled web. Weld size was controlled by applying multi-passes of welding when the specimens were fabricated. GTAW welding was applied at the Welding System Laboratory at MIT using the XMT^{IT} 300 CC/TIG DC INVERTER ARC WELDER welding machine. The welding material used in this experiment was TGS-50 manufactured by Kobe Steel that is equivalent to AWS A5.18. Specifications of TGS-50 are also listed in Table 3-1. The specimen preparation before welding for each specimen and welding conditions are listed in Table 3-2.

Bending of the specimens was performed using the Baldwin TEG Univ. bending machine located at the Remergence Laboratory in the Department of Civil Engineering at

MIT. The maximum loading capacity of this bending is 60,000 lbs. In Appendix-2, the calibration reference for the Baldwin TEG Univ. Machine-60,000 bending machine is attached. The video microscope (HI-SCOPE COMPACT MICRO VISION SYSTEM MODEL KH-2200 MDR) and a VCR video recorder were used to record and monitor the crack formation and propagation process during the tests. See the Appendix-2 for more detailed description of video microscope. Figure 3-9 shows the picture of experimental setup of three point bending with two ends simply supported by two roller.

Table 3-1 The chemical composition and mechanical specifications base metal AH-36 and TGS-50.

	Base metal	Weld metal
$\sigma_y (N / mm^2)$	281	340
$\sigma_{TS} (N / mm^2)$	346	470
Reduction in area (%)	61.1	36
Charpy energy absorption (-30° C) (Joules)	Not assigned	220
C (%)	0.29 max	0.080
Si (%)	-	0.700
Mn (%)	0.60-0.90	1.310
P (%)	-	0.011
S (%)	-	0.010

Table 3-2 Specimen Characteristics

SPECIMEN #	1	2	3	4
Plate length (mm)	400	400	400	400
Plate width (mm)	130	130	130	130
Plate thickness	9.5	9.5	9.5	9.5
Web length (mm)	130	130	130	130
Web height (mm)	50	50	35	35
Web thickness	9.5	9.5	20	20
Weld angle (deg.)	AW	AW	AW	AW
Beveled	No	Yes	No	Yes
Notched	No	No	No	No

- AW means as welded without any post welding machining.

3.3.2 Experimental recording

The displacements were read from the displacement gauge placed at the end of one piston arm of the bending machine. The loads were read from the meter on the bending machine. At each recording point, by pressing the timing button of the video recorder, the picture was obtained of the focused area of the specimen that was recorded at the same time as displacement and load data were being read. The crack phenomena of Specimens 2 and 3 can be schematically described in Figure 3-9. Specimens 2, 3 and 4 all sustained the first loading which means they didn't show any visible crack on the screen of video monitor through the microscope. However, Specimen 1 failed at the beginning of the first loading. A crack formed at the toe of the weld of Specimen 1, and the load dropped drastically from that point. This phenomenon can be clearly seen from the recorded load vs. displacement diagram. In Fig. 3-10, the load vs. displacement curves of Specimen 1 and Specimen 4 were put together for comparison. The early stage load drop of Specimen 1 compared with Specimen 2, Specimen 3 and Specimen 4 clearly

demonstrates the crack forming in Specimen 1 at the low displacement stage. This was because the weld angle at the toe of the weld at the end of the web is about 90° and the fillet weld of Specimen 1 has a convex contour. In other words, the result was the worst weld for Specimen 1. The large geometry gradient may theoretically be considered to have an infinite concentration factor. And consequently, it caused the fillet weld crack at the early stage of the loading of Specimen 1. This explanation offered a reason to take Specimen 1 as a singular case that is beyond the scope of this study assuming people in the practical world should have the common sense to reject weldment with such an extreme convex geometry. Since Specimens 2, 3 and 4 all didn't show any crack at the surface during the first load, and the Baldwin TEG Univ. Machine 60,000 bending machine has the limitation for the displacement that didn't allow an possibility to continuously load beyond 20° , a reverse load had to be applied to flatten the plates and then to apply the second load. In the real collision accident, the deformation of the plating may not need to reach 20° to get fracture. This is because in the real ship structure, the plating is constrained by periphery as an integrated structure. Tension will be created inside the plate which will lower the critical limit load of fracture of the weldment. In an experiment, it is hard to simulate the three dimensional (3-D) load effect. In the later part of this report, Chapter 5, the combination of bending and tension loads was tested in Specimen 7. Both Specimen 2 and Specimen 3 were found to have cracks during the second load. Specimen 4 did not show any observable crack even after the second load because it has both larger weld leg length and larger penetration which was guaranteed by multi-pass welding and beveling the web before welding.

Figure 3-11 was drawn from the video recorded data to show the observation of cracking formation and propagation procedure. In Figure 3-11, the crack started from a certain point of the root of the weld O^r then went through the weld to a point of the surface of weld O^s . This process was not observed by the micro video because it had been hidden beneath the weld metal before the crack broke through to the surface. However, it is safe to assume this procedure as mentioned above because from the FEM model we made we found that at the root of the fillet weld there was a large stress

concentration if the root gap existed. Strictly speaking, every fillet weld has root gap if it does not have complete penetration. At this moment, we still don't have the experimental method to get the inside information. In the future, further studies are needed. The crack then grew to the corner of the web point C, turned 90° to tear the web apart following the path $s\vec{r}$. This particular process was well recorded and can be accurately correlated with the load and displacement recordings. By studying the portion we have good record data on, regardless the progress of crack from point O' to point O^s that we still need further information about, the weld tearing process can be fairly well studied.

The crack propagating history from O^s point to point C occurred in a very short period of time and was unstable. Further studies on this initiation period are discussed in the next two chapters. In Report 3 of Rupture Analysis of Oil Tankers in Side Collision program, by A.F McClintock, mathematical models were built. Neglecting this unstable period which is from O^s to C, the calculation was performed as described later in this chapter, Sec.3.4. A Matlab program that fulfills this calculation task is attached in Appendix-4 of this report.. The test records of loads and displacements for each specimen are listed in Appendix-3.

3.3.3 Post failure specimen examination

After the loading experiment, Specimens 2 and 3 were cut and ground for post failure analysis. The cut was made close enough to the tip of the crack such that we could measure the displacement of the web to the base plate by assuming the measurement was close to the data of the crack tip displacement. A video microscope was applied to fulfill this measurement because it reduced the measurement error by the factor of its magnification. A ruler was put under the scope to get the scales of measurements. Figure 3-12 shows that the displacement at the crack tip of Specimen 2 is approximately 0.46 mm. Figure 3-13 tells that the displacement at the crack tip of Specimen 3 is about 0.32 mm. With these displacement measurements, calculations based on Elastic-plastic-Fracture mechanics theory were carried out in Sec. 3.4. below.

3.4 Calculations

3.4.1 Calculation of R_c from load vs. displacement data

Two assumptions were made to carry out the calculation. First, a constant moment applied at the crack tip with the crack advancing was assumed. Secondly, The separating base plate is considered as an continuously elongating cantilever beam. With the above two assumptions, each load was extrapolated by a second order curve extrapolation with respect to each displacement point. for the load with respect to each displacement point. These load points are imaginary loads that could give and energy consumed by bending a continuous elongated cantilever beam as shown in Figure 3-14. Equations 3-11s from Eqn. 3-11a through Eqn.3-11d is a set of equations used to calculate the load $P'_{i,m}$

$$M_0 = P_0 \times L_0, \quad 3-11a$$

$$L_{im} \cong a_i + L_0, \quad 3-11b$$

$$a_i = \sum \Delta a_i, \quad 3-11c$$

$$M_i = P'_{im} \times L_{im}, \quad 3-11d$$

where

M_0 is the initial moment when the crack just started,

P_0 is the load when crack began to propagate to the web side weld,

L_0 is the initial arm length for the moment applied at the crack tip,

L_{im} is the arm length for the moment applied at the crack tip for the imaginary ith load and displacement after crack started,

M_i is the moment applied at the crack tip for the imaginary the ith load and displacement after crack started,

a_i is the crack length at the ith load and displacement after crack started,

Δa_i is the crack growth length at the ith load and displacement after crack started,

P'_{im} is the imaginary the ith load needed to be calculated by extrapolating.

The work W_{b0} for bending a beam with crack propagating can be calculated by integrating the load-displacement curve as Eqn. 3-12

$$W_{b0} = \int_{a_i} P_i \bullet dc = \sum \frac{1}{2} P_i \bullet (c_{i+1} + c_i) \quad . \quad 3-12$$

It should be stated that M_0 in Eqn. 3-12 is the calculated at point O. This point can be assumed to be the point when load began to stably drop in the measured load displacement diagram. For Example, in Figure 3-14, it is indicated by the arrow.

The imaginary work W'_{im} can be calculated also by Eqn. 3-12 with the imaginary load P_{im} vs. displacement c_i . Thus, the difference between W'_{im} and W_{b0} gives the total tearing work W_{tear} that consumed by the crack propagating at the weld up to a certain measured length. As Eqn. 3-13 shows below

$$W_{tear} = W'_{im} - W_{b0} \quad . \quad 3-13$$

The tearing work per unit length which is an important criterion for judging the strength of fillet weld R_c then can be calculated by Eqn. 3-14 as below

$$R_c = W_{tear} / a_i \quad . \quad 3-14$$

For Specimen 2, this calculation gives $R_c = 658$ Nmm/mm, while for Specimen 3, $R_c = 852$ Nmm/mm. The calculation was performed by Matlab. See Appendix-4 for the programs. Figure 3-15 schematically shows the calculations of the R_c using the load vs. displacement diagrams for Specimens 2 and 3.

3.4.2 Calculation of R_c from post failure measurement data

McClintock, 1995, gave an model to calculate the tearing work of plastic failure by measuring the displacement u_f and assuming perfect plastic for the material behavior for the weld metal. Also, the assumption of homogeneity was made for the weld metal [McClintock, TSR 56]. This offered us another approach to check our calculation results for tearing work per unit length R_c . Equation 3-1 $P_L = 2 k d$, $k = TS / \sqrt{3}$. and Eqn.3-3 $R_c = P_L(u_i + u_f) / 2 \equiv P_L u_c$ give the calculation algorithm for the tearing work per unit length for the fillet weld.

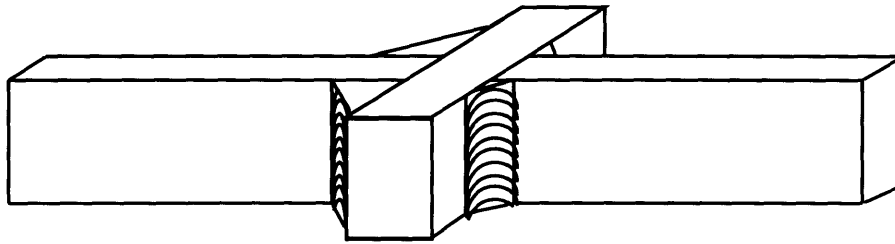
For Specimen 2, the leg length is 3 mm, and from the post fracture specimen, the $u_i + u_f$ was measured as 0.42 mm (Fig. 3-1). For Specimen 3, the leg-length is

approximately 4 mm, and the $u_i + u_f$ was measured as 0.35 mm (Fig. 3-1). The calculated R_c Specimen 2 and Specimen 3 are 627 N mm/mm and 839 N mm/mm, respectively.

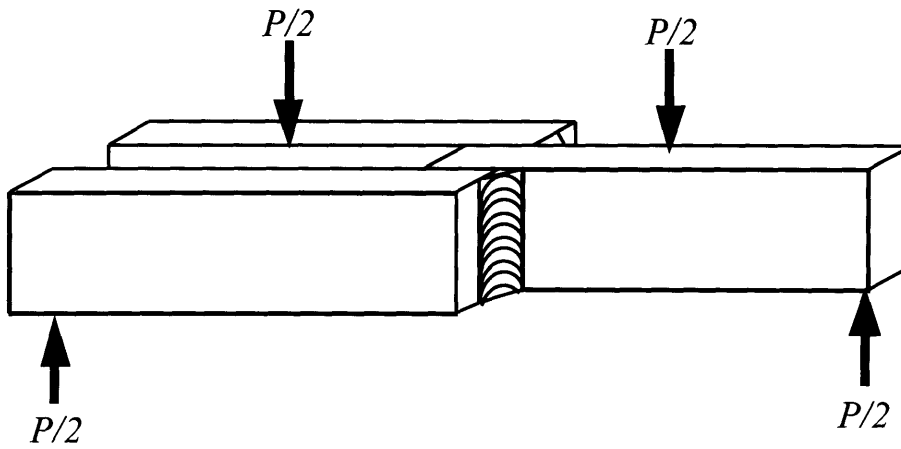
The reason for the lower values calculated by the post fracture analytical approach rather than by the integration method could be caused by the assumptions that the weld metal is homogenous and non-strain-hardening. The calculation from the experimental load vs. displacement curve included the strain-hardening effect for the weld metal.

3.5 Conclusions

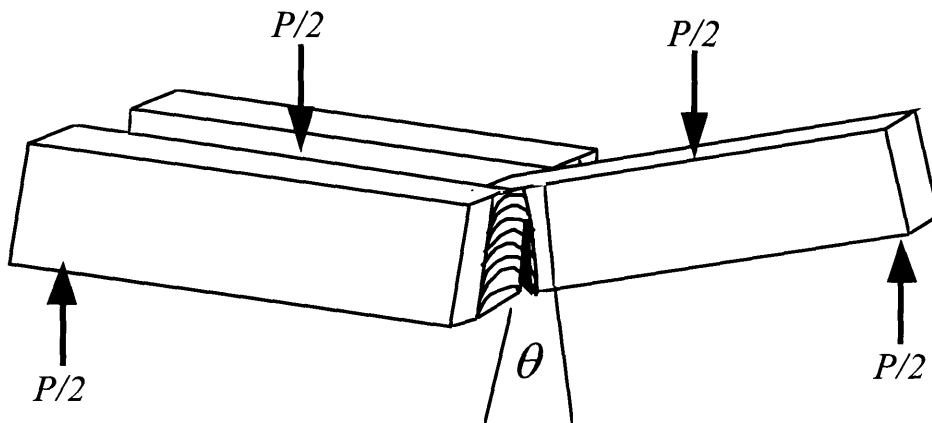
The tearing work per unit length of the fillet weld calculated from the experiment data and post failure analysis are close to each other within 5% difference. Additionally, by using the calculation approach of load vs. displacement integration, in which bending of a continuously elongated cantilever beam is assumed as the crack tip advances, the two idealized assumptions for the material namely homogeneity and perfect plasticity vanished. This confirms that the small scale test (three point bending of a fillet welded wide plate structure) can give fairly reasonable data. It is easier to perform than the traditional tearing test. The requirement for the ordinary bending machine is less than the huge tension machine and easier to operate. And the video microscope recording offers advantages for the new approach for doing fracture analysis experiments. For the design of the ship structure, the conclusion can be made that people can increase the tearing strength of a fillet weld by either increasing the weld metal strength (TS) or by increasing the weld size. In other words, the tearing work per unit length of fillet weld is a function of material properties and weld size. Even the data from Specimen 1 and Specimen 4 were not used in quantitative calculation, they offered qualitative criteria of the weld performance by geometry contour and size.



(a) Recommended

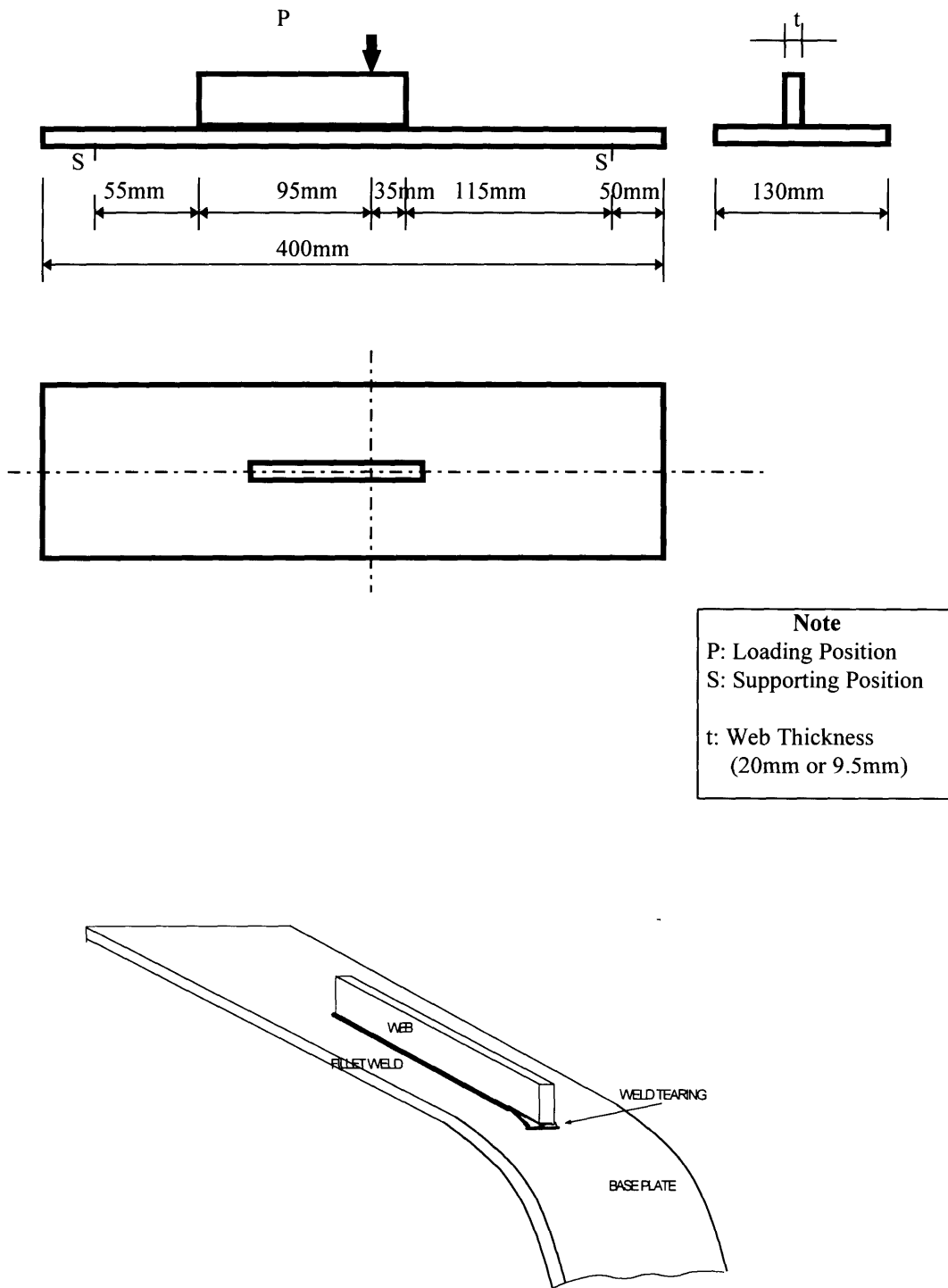


(b) As fabricated



(c) Cracked

Figure 3-1 TWB specimen test configuration (Kirkov, TSR 29).



Note
P: Loading Position
S: Supporting Position
t: Web Thickness
(20mm or 9.5mm)

Figure 3-2 Wide plate bending specimen dimension drawing.

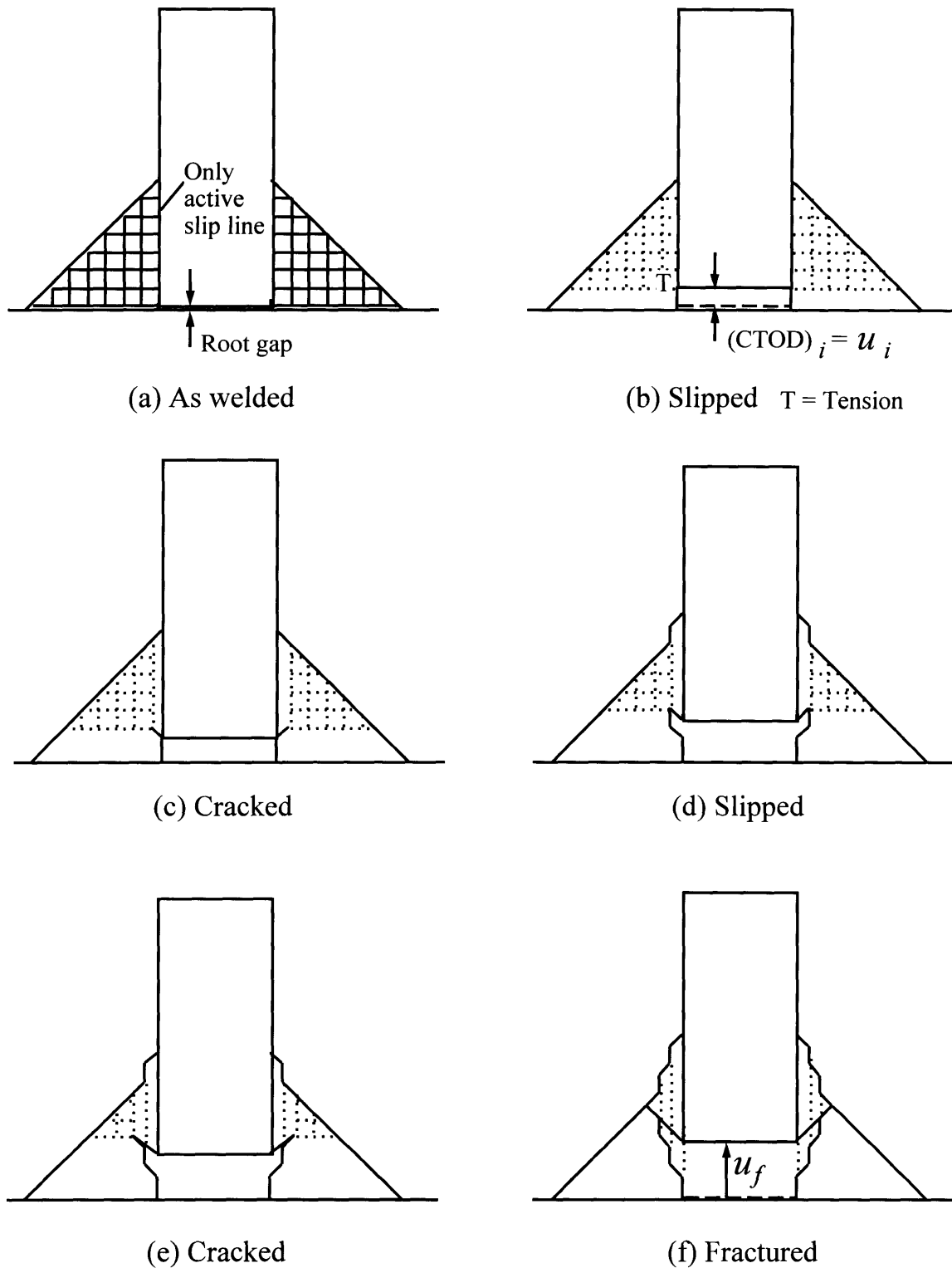


Figure 3-3 Slip line fields, crack tip opening displacement for initiation, $CTOD_i = u_i$, and alternating cracking and sliding off during growth to final separation at u_f .

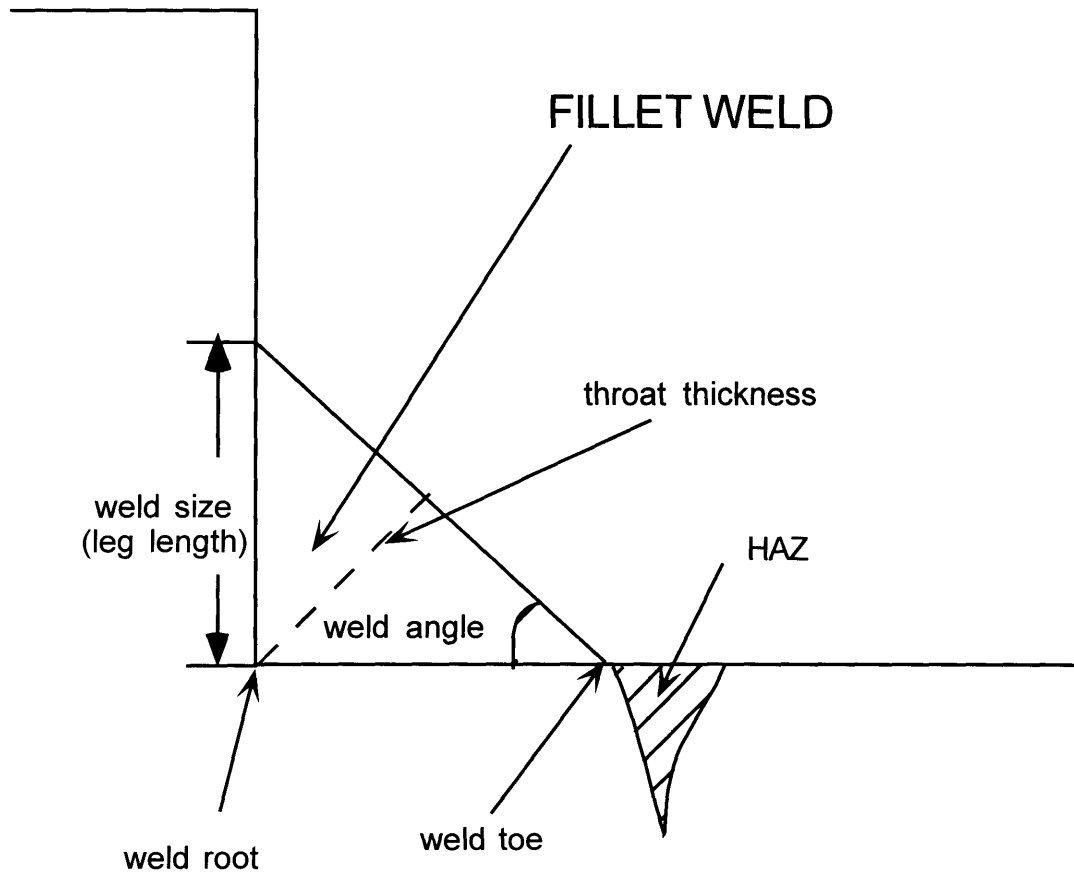
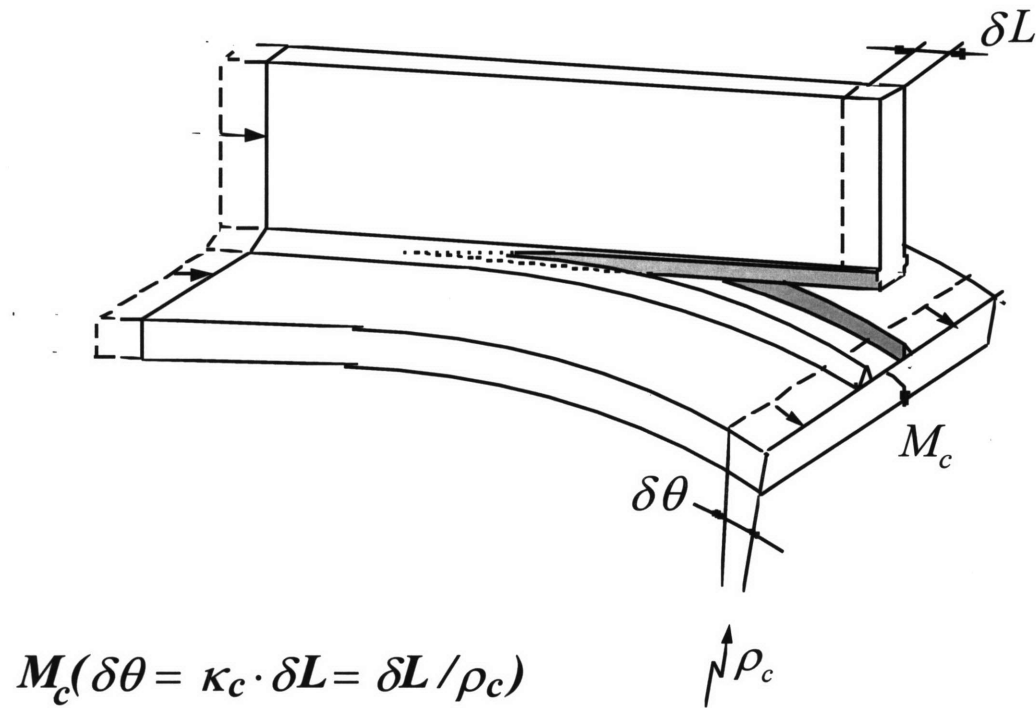


Figure 3-4 Geometry and definitions of a fillet weld (Sampos, 1996).



(little interaction)

$$M_c \kappa_c \delta L = \left(\int^{\kappa_c} M d\kappa \right) \delta L + R_c \delta L$$

Figure 3-5 Control volume for the critical tearing work per unit length R_c in peeling. Note that an oblique crack front leads to crack growth through the weld in locally plane strain conditions (TSR 26, McClintock, 1994).

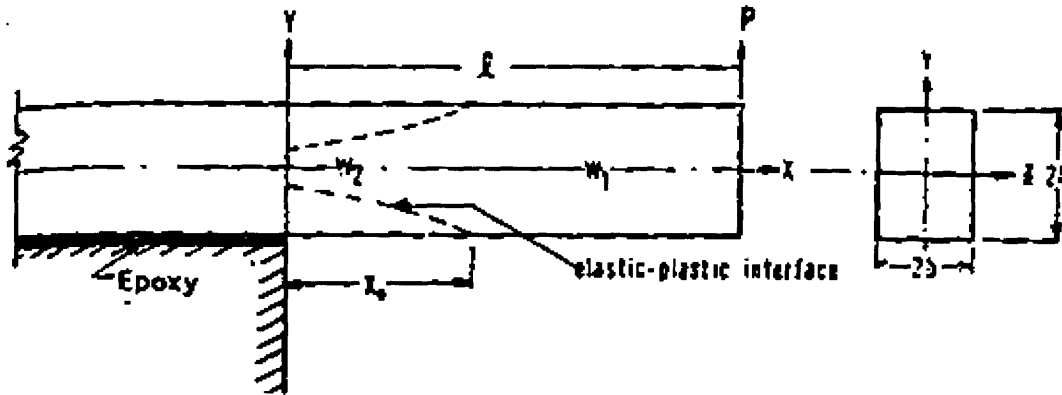


Figure 3-6 Peeling of an elastoplastic metal epoxy joint by an end force
(Atkins and Mai, 1987).

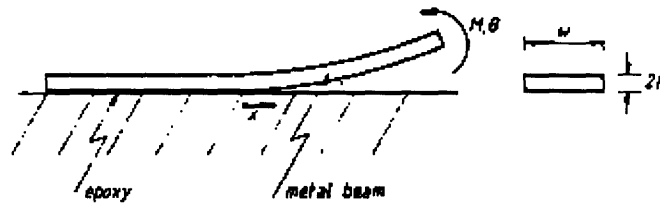


Figure 3-7 Peeling of an elastoplastic metal-epoxy joint by an end couple (Chang et al, 1972)

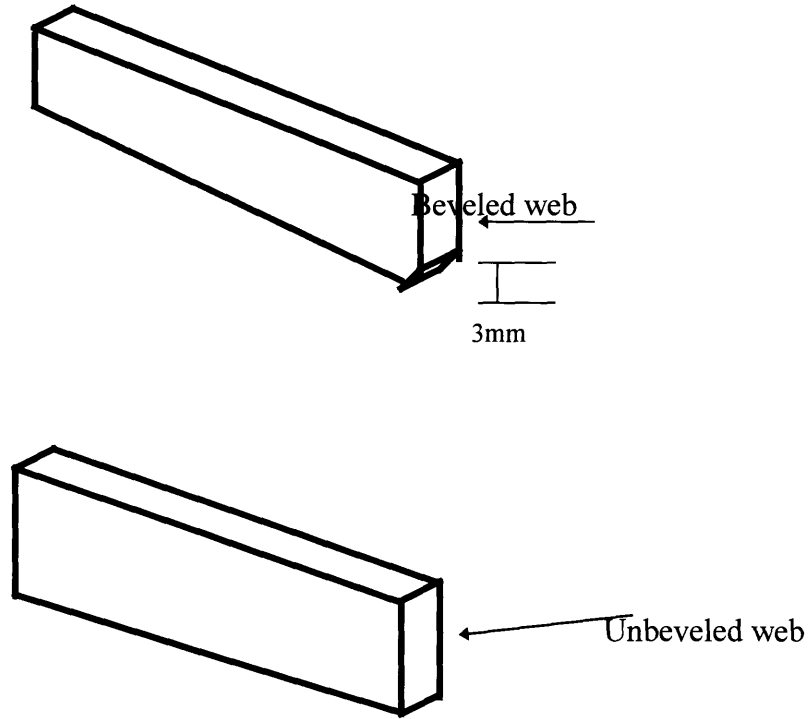


Figure 3-8 Beveled and unbeveled web.

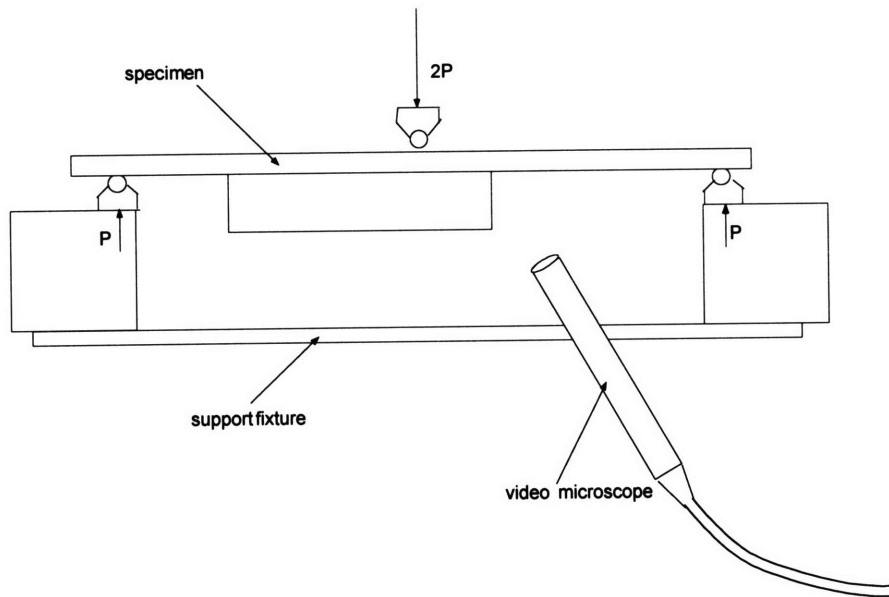
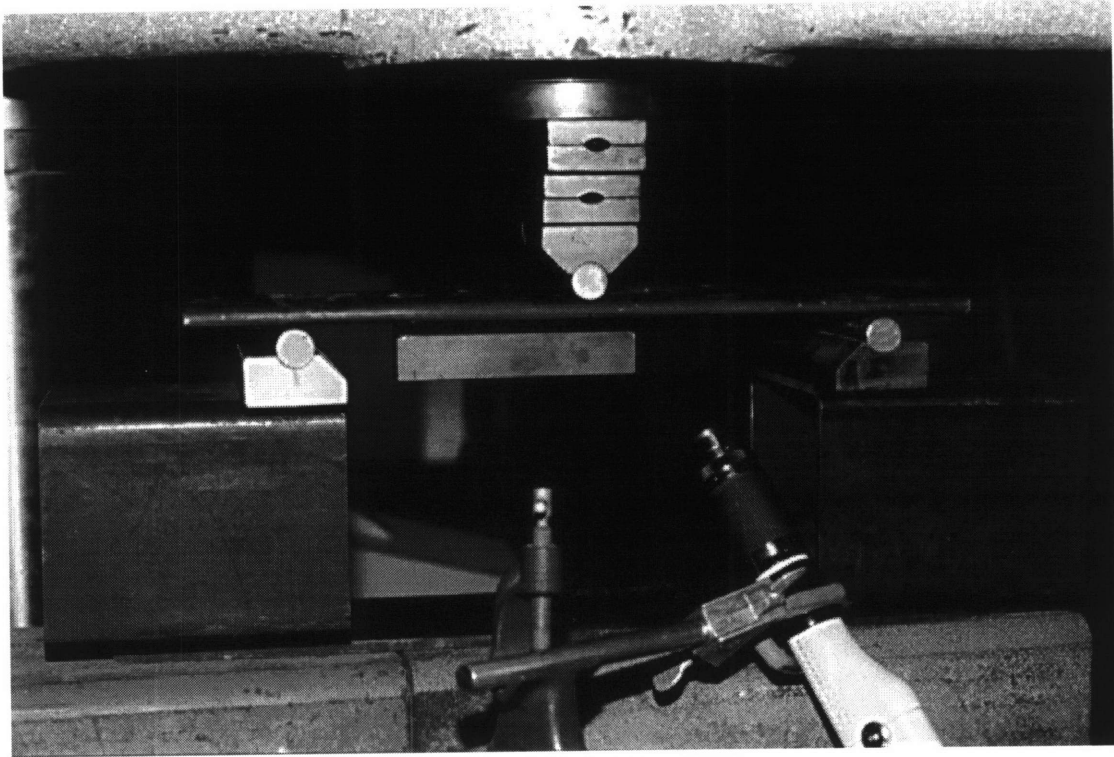


Figure 3-9 Wide plate bending experiment setup.

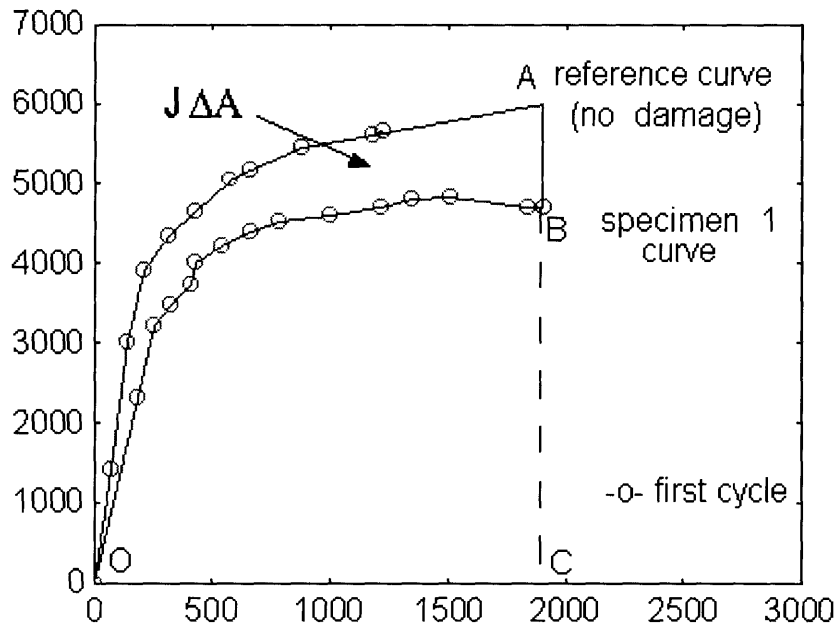
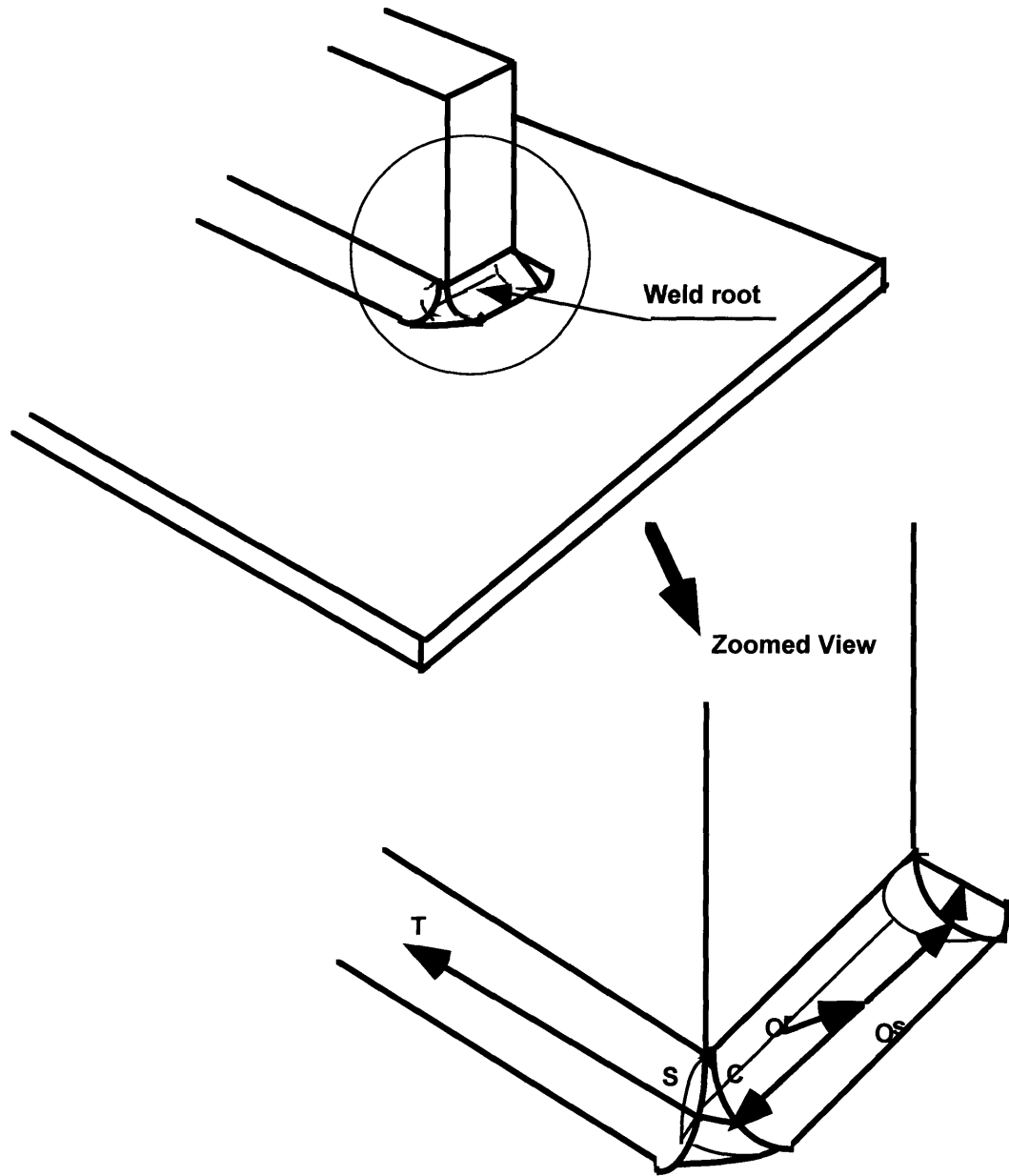
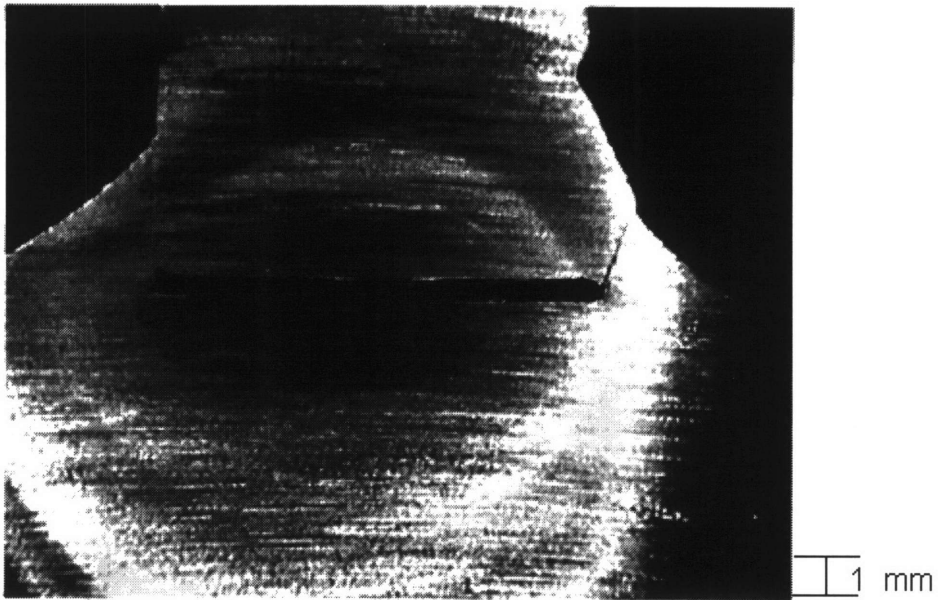


Figure 3-10 Comparison of load vs. displacement diagrams of Specimen 1 and Specimen 4

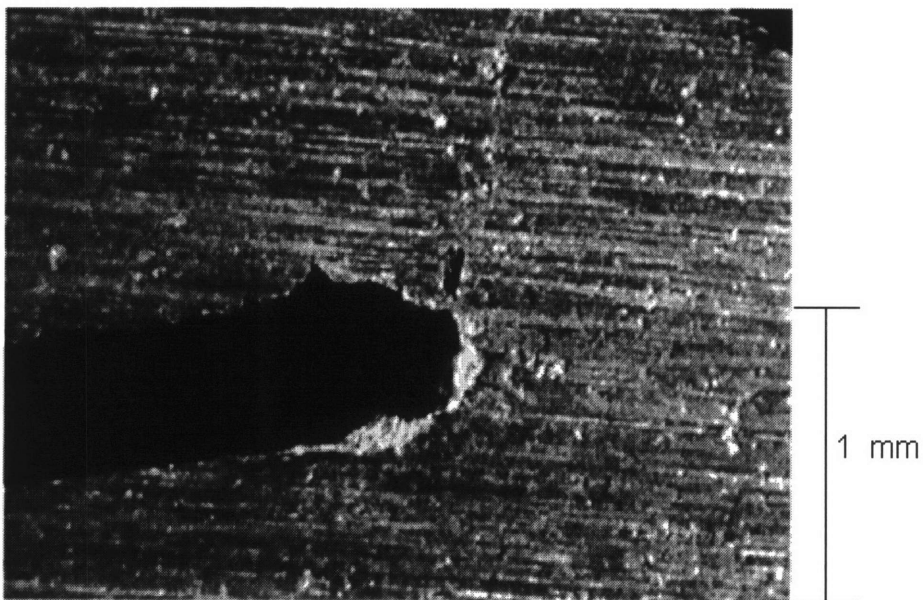


- O^r: Crack originated at the root of the weld.
- O^s: Crack appears to the surface of the weld.
- C : Crack propagate to the corner of the weld.
- S: Crack propagate to the web side fillet weld.
- T: Crack propagation tip at the fillet weld.

Figure 3-11 Schematic drawing of the cracking process of the specimens during tests.

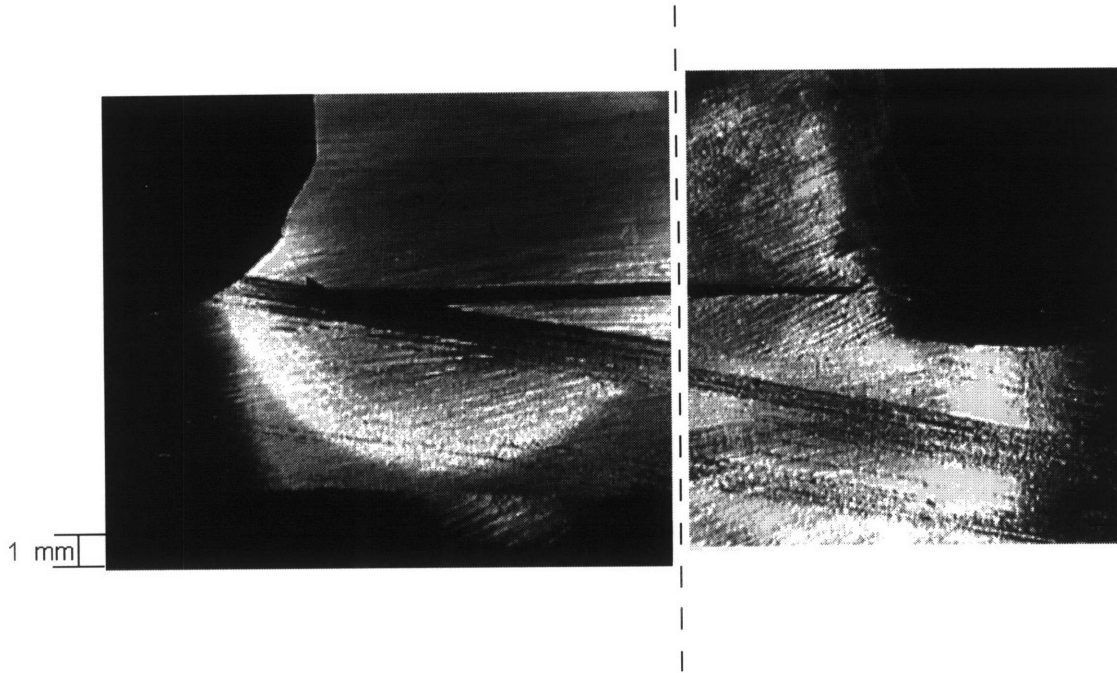


a) Specimen 2 cross sectional view of the fillet weld after fracture.

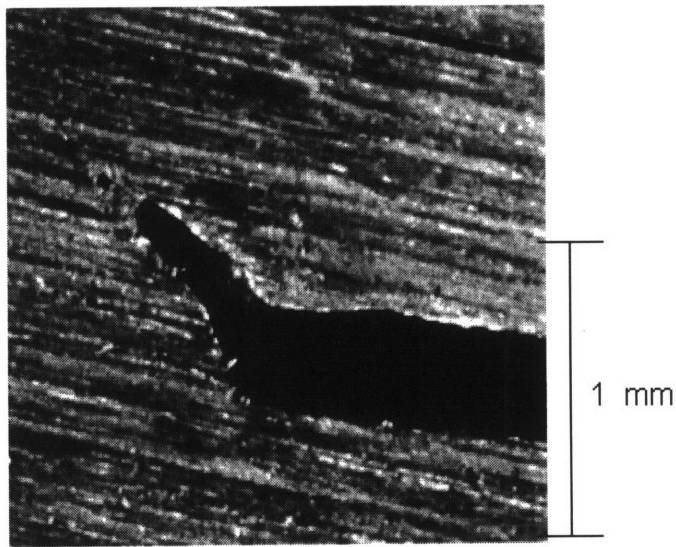


b) Displacement of the web from the base plate for specimen 2.

Figure 3-12 Post failure pictures of Specimen 2.

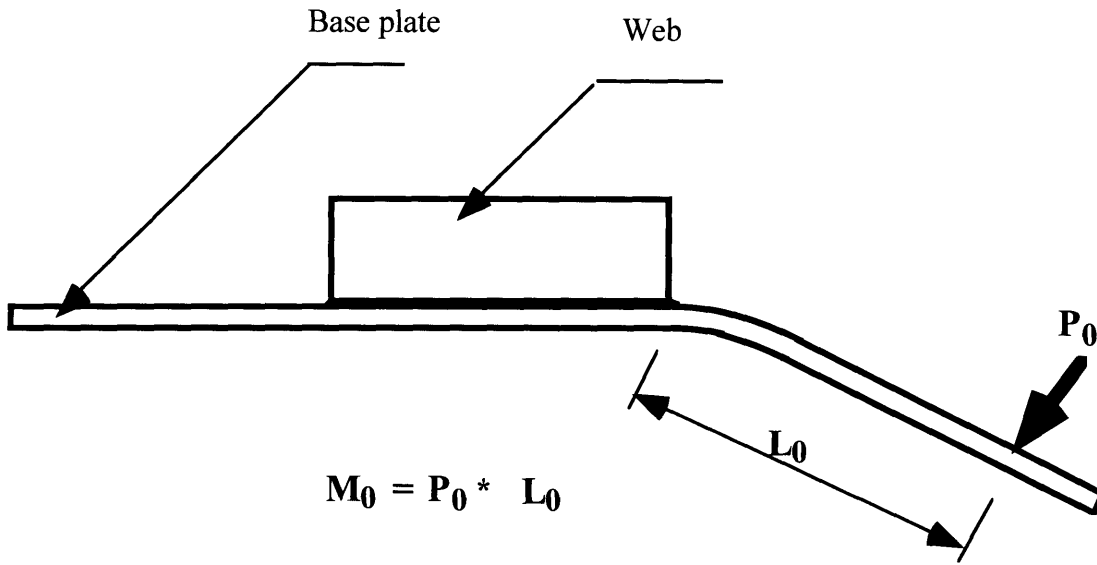


a) Specimen 3 cross sectional view of the fillet weld after fracture

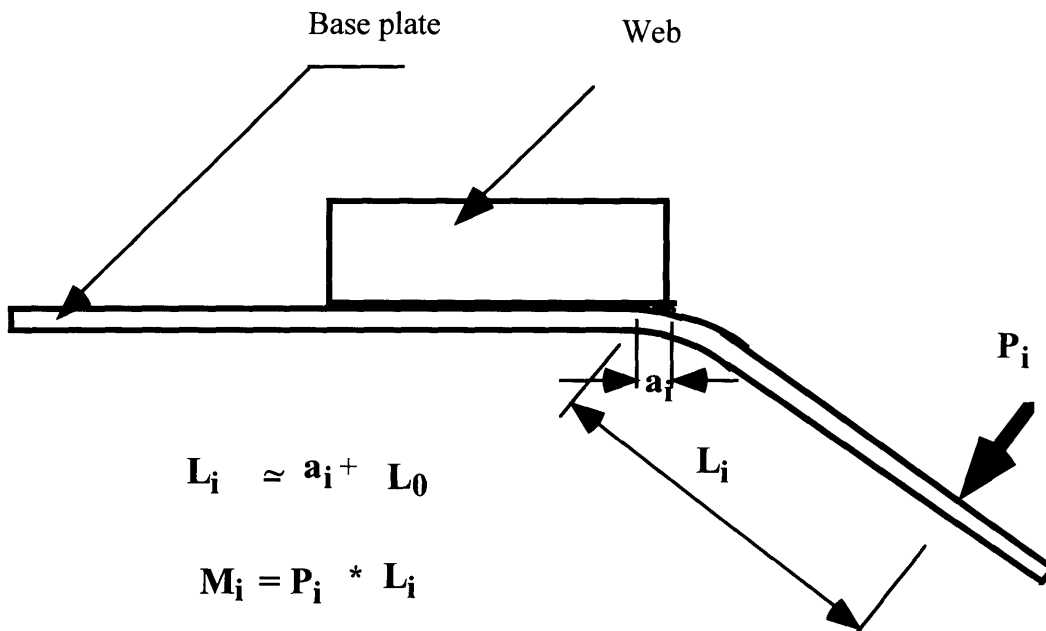


b) Displacement of the web from the base plate for specimen 3.

Figure 3-13 Post failure pictures of specimen 3.



a) Bending moment before the crack goes to the side fillet



b) Bending moment after the crack goes to the side fillet

Figure 3-14 Schematic drawing bending moment of the specimen.

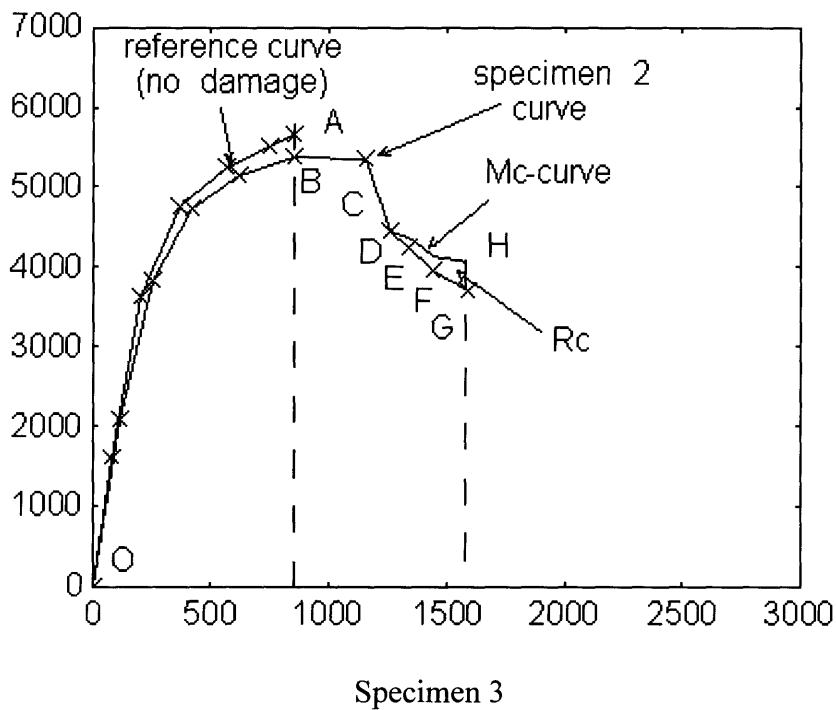
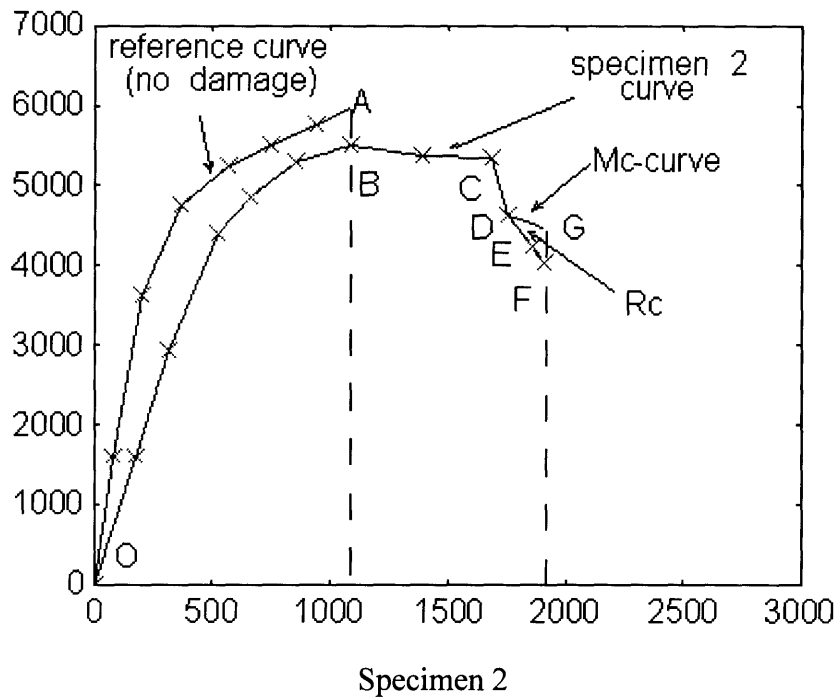


Figure 3-15 Specimen 2 and specimen 3 load vs. displacement curves (Mc means the constant moment).

Chapter 4 Strain and Stress Concentration Analysis at the Fillet Weld Toe with Simply Supported Boundary Condition

4.1 Overview

This chapter discusses results of a study of the strain and stress concentration effect on the toe of end fillet weld with a machined notch that simulates the undercut defect. Three point bending tests of Specimen 5 and Specimen 6 with different welding angle geometries were performed.

Undercut is a common defect in fillet welds. Undercut is usually caused by either improper welding performance or by too high welding current. A severe undercut would deteriorate the mechanical performance of the structure. Figure 4-1 shows the typical undercut occurrence [TSR 56, 1996]. Figure 4-1 is a hardness distribution diagram of a fillet weld. An undercut exists at the vertical toe of the fillet weld. Due to the multiple causes for the undercut, it is hard to totally eliminate undercuts in production welds. Various non destructive test (NDT) methods can be applied to find undercut of a weld. However, most NDT tests are time consuming. And repairing welding for the defect weld is not hasty either. The purpose of this study is to point out the priority level of undercuts that may give a guidance to the manufacturer to pay more attention at the more vulnerable structure parts during welding. Or, when the NDT test is performed, more efforts should be spent to those particularly locations.

Little literature is available on the notch effect at the real weld which is subjected to large plastic deformation. The crack tip opening displacement (CTOD) test is designed for small strains. Nevertheless, in collision or grounding accidents, ships structures have had large plastic deformation before they failed. In other words, the strains at the local area of the welds in ship structures upon accidents may go far beyond the elastic strain range.

In this chapter, by applying the available theory combining the experimental results and numerical simulation, a quantitative plastic strain value (ε_f) is calculated with the relation of the weld angle. See Figure 4-2 for the weld angle of specimens 5 and 6. Results show that Specimen 5 which has a welding angle of 57° sustained much less displacement compared to Specimen 6 with a smaller welding angle of 42° . The FEM simulation shows that the fracture happened at $\varepsilon = 16\%$ at the toe of the end fillet weld when displacements reached the failure points for both Specimen 5 and Specimen 6. See Figure 4-3 of FEM calculation result.

4.2 Theories Applied

4.2.1 Linear elastic fracture mechanics

The linear elastic fracture mechanics (LEFM) theory can be usefully applied as long as the plastic zone is small compared to the crack size. This is usually the case in materials where fracture occurs at stresses appreciably below the yield stress and under conditions of plain strain. Under conditions of general yield the plastic zone spreads through the entire cracked region. The crack will propagate if the plastic strain at the crack tip exceeds a critical value. Assuming negligible strain hardening, the stress at the crack tip hardly increases after general yield. Consequently, the fracture condition is more strain controlled. A commonly used but not strictly correct measure for the plastic strain at the crack tip is the crack tip opening displacement (CTOD). Therefore, it can be argued that fracture occurs at the exceedance of a critical CTOD [Broek, 1991].

Using a model derived by Dugdale (1960), which assumes a crack with a tip plastic field replaced by a crack with an effective length and no plasticity, the CTOD δ is given by

$$\delta = \frac{8\sigma_y\alpha}{\pi E} \ln \sec\left(\frac{\pi\sigma}{2\sigma_y}\right), \quad 4-1$$

where

α is the real crack length,

σ_y is the yield strength,

E is the Young's modulus of the material,

σ is the applied stress.

Crack extension or propagation is assumed to occur when the CTOD reaches a critical value δ_c . In the case of LEFM, the CTOD is given by

$$\delta = \frac{4}{\pi} \frac{K_I^2}{E \sigma_y} \quad . \quad 4-2$$

and δ_c is equivalent to K_{Ic} according to Broek. The limitation of the above theory is that it may not give good estimation when strain goes to plastic domain.

An alternative method to characterize elastic plastic fracture mechanics (EPFM) is by the use of the J-integral. This integral is defined as

$$J = \int_{\Gamma} \left(W dy - T \frac{\partial u}{\partial x} ds \right) \quad , \quad 4-3$$

with

$$W = W(x, y) = W(\varepsilon) = \int_0^{\varepsilon} \sigma_{ij} d\varepsilon_{ij} \quad , \quad 4-4$$

where

Γ is a closed contour followed counter clockwise direction in a stressed solid,

T is the tension vector (traction) perpendicular to Γ in the outside direction, $T_i = \sigma_{ij} n_j$, u is the displacement in the x -direction,

ds is an element of contour line Γ .

See Fig. 4-4. W is the strain energy per unit volume. Rice has shown that the J-integral, as defined along a contour around a crack tip, is the change in potential energy for a virtual crack extension da :

$$J = -\frac{\partial V}{\partial a}, \quad 4-5$$

where

V is the potential energy.

This relationship holds whether loading takes place under fixed displacement or constant load. For the first case, Eqn. 4-5 can be written as

$$J = -\left(\frac{\partial V}{\partial a}\right)_u = -\int_0^p \left(\frac{\partial P}{\partial a}\right)_v dv. \quad 4-6$$

This case is shown schematically in Figure 4-5. Crack initiation occurs when J reaches a critical value J_{IC} . At steady state stable crack growth is described by

$$J \geq J_R, \quad 4-7$$

where

J_R represents the fracture resistance of the material [Broek, 1991].

4.2.2 Dynamic fracture

In some fractures, time is an important variable. The most general case of dynamic fracture involves three features which are included in LEFM and EPFM theories: inertia forces, rate-dependent material behavior, and reflected stress waves. Determining a fracture characterizing parameter, such as the stress intensity factor, for rapid loading can be very difficult. For the case where the size of the plastic zone around the crack tip is small a Mode I near tip stress field can be given by

$$\sigma_{ij} = \frac{K_I(t)}{(2\pi r)^{1/2}} f_{ij}(\theta, V) \quad . \quad 4-8$$

where

$K_I(t)$ denotes function of time,

V the crack is the speed.

From recent work done by Nakamura et al. it was found that there was a transition time, above which inertia and stress waves effects may be neglected, and a quasi-static approach may be applicable [Anderson, 1995].

If the effects of inertia and reflected stress waves can be ignored, one of the three the features mentioned above left is the rate-dependent material response. High strain rates tend to elevate the flow stress of the material. The effect of the loading rate on the fracture toughness of a material depends on the failure mechanism. If failure occurs by cleavage, which is stress controlled, the fracture toughness decreases as the strain rate increases. If the failure is strain controlled, the higher flow stress results to larger energy absorption, which is translated to increased fracture resistance [Anderson, 1995].

Drar in 1994 proposed a model that predicts the fracture toughness of plain carbon steel for different temperatures and strain rates. The increase in loading rate shifts the quasistatic transition curve to higher temperatures, reduces the cleavage fracture toughness both on the lower shelf and in the temperature-dependent regime and increases the crack growth resistance. The main difference between impact and slowly applied load can be explained by the greater volume of metal deforming at low rates. However, the sensitivity to strain rates varies for different materials, being largest for body centric cubic (BCC) metals and smallest for face centric cubic (FCC) metals. The rate sensitivity arises from the fact that at high rates there is not enough time for the thermal energy caused by the plastic deformation to assist the dislocation movement. Due to the

limitation of our experiment conditions, this features were not physically tested at MIT. Literature review deems to cover the features that real ship fractures preserve.

4.2.3 Elasto-plastic fracture mechanics (EPFM)

The Japan Welding Engineering Society (JWES) standard WES2805 has been widely used to evaluate the fracture safety of structures. It is based on elastic-plastic fracture mechanics (CTOD criterion), because most brittle fracture incidents may occur from a defect at a structural stress concentration where plastic zone is generally greater than the defect size. This approach has been used for the fracture strength assessment of the fillet welds and its validity has been accepted [Hagiwara, 1985], [Machida, 1991]. The condition for fracture is expressed by

$$\delta \geq \delta_c , \quad 4-9$$

where

δ is the applied CTOD,

δ_c is the fracture toughness of the material.

δ_c can be determined by a three-point CTOD test in accordance to existing testing standards. In this approach, the applied CTOD is taken from a CTOD design curve which is formulated by

$$\delta = \begin{cases} 2e_y \bar{\alpha} (e/e_y)^2 & : e/e_y \leq 1.0 \\ e_y \bar{\alpha} (3.5 e/e_y - 1.5) & : e/e_y \geq 1.0 \end{cases} , \quad 4-10$$

where

e is the applied local strain,

e_y is the yield strain,

$\bar{\alpha}$ is LEFM-based equivalent through-thickness crack flaw.

In Eqn.4-10, an "average local strain" \tilde{e} is defined and used as applied strain (e). \tilde{e} is the strain value averaged over the cracked area and is given by

$$\tilde{e} = \tilde{K}_\varepsilon e_{nom} , \quad 4-11$$

where

\tilde{K}_ε is the average local strain concentration factor.

In the case of $\sigma_{net} < \sigma_Y$, the nominal strain is given by

$$e_{nom} = \sigma_g / E , \quad 4-12$$

where

σ_g is the gross stress at the crack area,

σ_{net} is the stress without considering the crack.

Assuming a power law hardening stress strain relation $\tilde{\sigma} = F\tilde{e}^n$ the nominal strain e_{nom} for the case that $\sigma_{net} > \sigma_Y$, is given by

$$\tilde{\sigma} = F\tilde{e}^n \exp(-\tilde{e}), \quad \tilde{e} = \ln(1 + e_{nom}) . \quad 4-14$$

The strain hardening exponent n can be expressed as a function of the yield stress of the material σ_Y

$$n = 0.12 \ln(1392 / \sigma_Y), \quad \sigma_Y: \text{MPa} . \quad 4-15$$

The average local strain concentration factor \tilde{K}_ε can be estimated from the average elastic stress concentration factor given below

$$\tilde{K}_\varepsilon = \begin{cases} \tilde{K}_t & \tilde{K}_t \sigma_g \leq \sigma_Y \\ \tilde{K}_t + A(\sigma_g / 1.125\sigma_Y - 1 / \tilde{K}_t) & \sigma_{net} \leq \sigma_Y \leq \tilde{K}_t \sigma_g \\ \tilde{K}_t^{2/(1+n)} & \sigma_{net} \geq \sigma_Y \end{cases} , \quad 4-16$$

where

$$A = \alpha(\tilde{K}_t^{2/(1+n)} - \tilde{K}_t)/(1 - \alpha/\tilde{K}_t),$$

$$\alpha = \sigma_{net}(\text{no crack})/\sigma_g.$$

The average stress concentration factor \tilde{K}_t is the value of the elastic stress concentration factor K_t averaged over the crack area, and it can be estimated by elastic stress analysis.

That kind of analysis has been performed for two-dimensional T-joints, and empirical formulas have been constructed. In order to evaluate stress concentration factors that they could be used for brittle fracture and fatigue assessment [Niu, 1987], [JSNA,170,171,1985]. Considering the geometry in Figure 3-7 the stress concentration factor for bending is given by

$$K_t = 1 + 0.5121 \cdot \alpha^{0.572} \left(\frac{t}{\rho} \right)^{0.469} \quad 4-17$$

$$\text{for } \frac{\pi}{6} \leq \alpha \leq \frac{\pi}{3} \text{ and } \frac{1}{50} \leq \frac{\rho}{t} \leq \frac{1}{15} \text{ [Niu,1987].}$$

The effect of a defect such as an undercut is to magnify K_t . The amount of this magnification for an undercut with 1 mm radius of curvature at the toe of a 45° weld has been calculated by Onozuka et al. for various undercut depths [JSNA,170,171,1985]. It was found that the stress concentration factor increases greatly until the depth of 0.1 mm, slower until the 0.3 mm and gradually over 0.3 mm. The stress concentrations that they calculated for a 10 mm thick beam under bending were about 2.63 at depth=0.1mm, 3.0 at depth=0.3 mm and 3.58 at depth=1 mm. Without the undercut, the stress concentration can be calculated from Eqn. 4-17 and is equal to 2.58. Therefore, it can be said that the existence of an undercut with 1 mm depth magnifies the stress concentration by a factor of 1.39.

The JWES approach mentioned above can be applied for the geometry of the Specimen in order to investigate the case where fracture at the fillet weld toe will initiate. At large strains the effect of a small surface crack on the stress profile is negligible and it can be assumed that $\sigma_{net} = \sigma_g$ for $\sigma_{net} \geq \sigma_y$. Then the applied CTOD will depend on

$$\tilde{K}_g = \tilde{K}_t^{2/(1+n)}.$$

4.3 Experiment Performance

4.3.1 Specimen preparation and instrumentation

AH36 base plates of 3/8" (9.5mm) thick and the web plates of 20mm or 9.5 mm thick were cut to desired dimensions in the machining shop at MIT. The chemical composition and mechanical specifications of AH36 are listed in Table 3-1 [ABS, 1985]. Also, see Figure 3-2 for the details of specimen dimensions. Because the ductile strength of weld is mainly determined by the weld size and penetration, deeper penetration can give a stronger weld [Wilcox, 1995]. In this experiment, the penetration had been experimentally controlled by beveling the web before welding was performed. See Figure 3-8 for the beveled and unbeveled web. Weld size was controlled by applying multi-passes of welding when the specimens were fabricated. GTAW welding was applied at the Welding System Laboratory at MIT using the XMT^{IT} 300 CC/TIG DC INVERTER ARC WELDER welding machine. The welding material used in this experiment was TGS-50 manufactured by Kobe Steel that is equivalent to AWS A5.18. Specifications of TGS-50 are listed in Table 3-1. The web preparation before welding for each specimens and welding parameters are listed in Table 3-2. A half cylindrical notch was made at the toe of the end fillet weld. The 1/32" diameter ball type milling cutter was used on a vertical milling machine. The notch was cut 1" Length and 1/32" deep. See Figure 4-7 for the details of the specimen with a notch. Before the bending load was applied the leg lengths of the Specimen 5 and Specimen 6 were measured and the weld angle was calculated. Table 4-2 below gives the weld dimensions of Specimen 5 and Specimen 6.

Table 4-1 Specimen Characteristics

SPECIMEN #	5	6
Plate length (mm)	400	400
Plate width (mm)	130	130
Plate thickness	9.5	9.5
Web length (mm)	130	130
Web height (mm)	35	35
Web thickness	20	20
Weld angle (deg.)	57	42
Beveled	Yes	Yes
Notched	Yes	Yes

Table 4-2 The end fillet weld dimension measurement of Specimen 5 and Specimen 6

	leg length on the web side	leg length on the base pate side	weld angle
Specimen 5	9.55	6.2mm	57°
Specimen 6	7.02mm	7.8mm	42°

Bending of the specimens were performed using the Baldwin TEG Univ. bending machine located at Remergence Laboratory in the Department of Civil Engineering at MIT. The maximum loading capacity of this bending is 60,000 lbs. In Appendix-4, the calibration reference for the Baldwin TEG Univ. Machine-60,000 bending machine is attached. The video microscope (HI-SCOPE COMPACT MICRO VISION SYSTEM MODEL KH-2200 MDR) and a VCR video recorder were also used to record and

monitor the crack formation and propagation process during the tests. Also, see the Appendix-2 for more detailed description of video microscope. Figure 4-7- shows the picture of experimental setup of three point bending with two ends simply supported by two roller.

4.3.2 Experiment observation

During the test, for Specimen 5, one of the notch ends coincides with an area where the toe of the weld has a discontinuity. This increases significantly the stress concentration. For this reason cracking initiated very early at that point, whereas the other side of the notch did not show any indication of cracking. At that side fracture started at the second cycle and specifically at point A2 in Figure 4-7.

Figure 4-8 shows the load displacement curves for Specimen 6 with reference to points that correspond to photos shown in Appendix D. The identification of crack initiation was very difficult for Specimen 6. Many small surface cracks were created (point A1). Those cracks became clearly visible only at large deformations (points B1, C1). At point C1 multiple cracking appeared also at the notch end at the surface of the base plate.

Multiple cracking occurs because the existence of flow stress distributes strain to a large area. Referring to Figure 4-9, it can be seen that this does not happen at the second cycle. The power law material behavior, during that cycle, caused strain concentration at points where stress concentration existed. For that reason only one crack grew during the second cycle in Specimen 6 (points B2 through D2). See .appendix-4 for the experiment data.

This observation indicates the importance of the second cycle in a structure subjected to large deformation. Fracture in the case of very low cycle fatigue is strain

controlled. Weld defects and geometric discontinuities can cause large stress concentrations which can be interpreted to strain concentrations. Research on methods that could be used to reduce stress concentration in a structure has been extensively performed for the case of high cycle fatigue [Radaj,1990]. It can be concluded that any design practice that reduces the stress concentration, used for fatigue prevention, will favor the resistance of a structure to very low cycle fatigue.

4.4 Calculations

Although the average stress concentration factor \tilde{K}_t for the whole cross section of the plate is not known the local K_t at the toe of the weld can be given by Eqn. 4-17. This result must be multiplied by a factor that will take into account the influence of the undercut. For the case of a 45° weld, the magnification factor is 1.39 for an undercut depth of 1 mm. Assumption was made that the same magnification occurs at specimens 5 and 6. The radius of curvature at the toe of the of weld is taken equal to the radius of curvature of the notch, which is $1/32$ of an inch. It has been assumed that Eqn.4-17 can be extrapolated for the case of $t/\rho = 12$. The values of K_t that were calculated for specimens 5 and 6 are 3.66 and 3.32, respectively.

Using K_t instead of \tilde{K}_t will underestimate the total fracture resistance of the base plate but it will represent the case for fracture initiation at the toe of the weld. Whether the fracture will propagate to catastrophic failure depends on the fracture properties of the material under the specific loading conditions and the size of the initial crack. The case is the same as that analyzed for Specimen 1.

The relationship between the actual flaw geometry and the LEFM-based equivalent through thickness crack flaw can be found from Figure 4-6 [Harrison,1978]. If we assume an initial flaw with depth 0.1 mm it will be found that \bar{a} is approximately 0.1

mm also. Using Eqn. 4-10 for large deformations, the critical strain to fracture will be given by

$$e_f = \frac{\left(\frac{\delta_c}{a} + 1.5 \cdot e_y \right)}{3.5K_I^{2/(1+n)}}, \quad 4-18$$

where

δ_c is the critical CTOD and e_y is the yield strain.

It has been mentioned that fracture takes place in the base metal rather than in the HAZ. The case differs from that of Specimen 1 because the strain concentration is not any more in the toe of the weld. The wide notch causes strain concentration in the base metal, which deforms more easily. For this reason δ_c values that correspond to the base metal must be used, instead of values that correspond to the HAZ. For mild steel typical δ_c value can be taken to be 0.15 mm. The strain hardening exponent was taken equal to 0.24 [Kardomateas,1985]. Using those numbers, we find that the critical strain is 0.054 for Specimen 5 and 0.063 for Specimen 6.

A finite element modeling (FEM) had been performed model of the experiments. From that model the relationship between the applied displacement and the nominal strain at the toe of the weld has been found Figure 4-3. During the experiments, the displacements at which cracking initiated were approximately 17 mm for Specimen 5 and 20 mm for Specimen 6. Those displacements correspond to nominal strain values of 0.057 and 0.067 respectively.

It can be seen that there is a good agreement between the predicted critical strain range and the experimental results. This supports the validity of the JWES method for fracture assessment and therefore the validity of Eqn. 4-18 for the case of large strains. This formula proves the strong influence of the stress intensity factor on the value of the critical strain to fracture. It also shows the reason why alternating plasticity may become

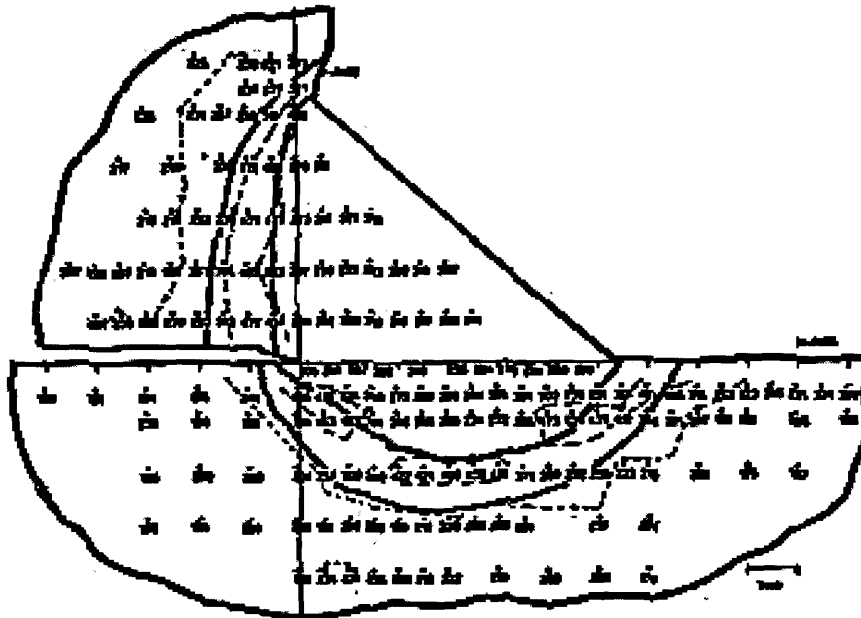
catastrophic. After each cycle the equivalent crack length \bar{a} increases which reduces the e_f . If the cyclic loading is displacement controlled, reduction of e_f will result to increase of the crack growth per cycle.

Another parameter that changes with alternating plasticity is the strain hardening exponent n . For mild steel it has been found that the cyclic strain hardening exponent is equal to 0.19 [Schwartz,1988]. The smaller value of n results to larger strain concentrations for the same stress concentration at the second cycle than at the first. Consequently, the ability of the structure to sustain large deformations without fracture is reduced during cyclic loading.

4.5 Conclusion

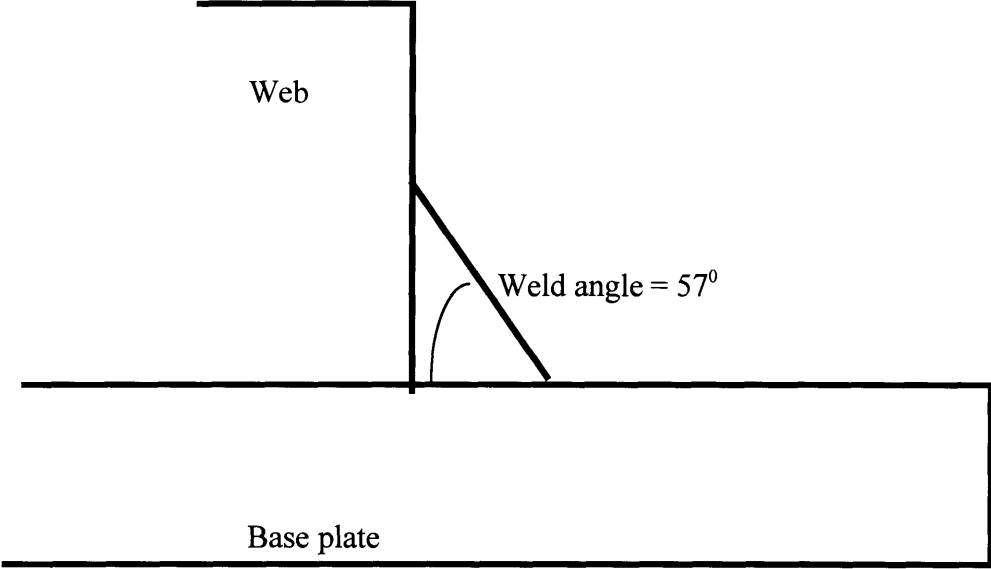
From the calculation in the above section, we can see the contour of end fillet weld plays an important role for the strain concentration. Specimen 5 which has larger weld angle (57°) sustain less displacement than Specimen 6 which has smaller weld angle (42°). The simulated the undercut also causes a significant role in the strain concentration. Structures can sustain larger displacement if locally improvement the weld quality and reduction of the weld angle are feasible.

Vicker's Microhardness Measurements for a Common Shipping Steel Welded with an E7016 Electrode

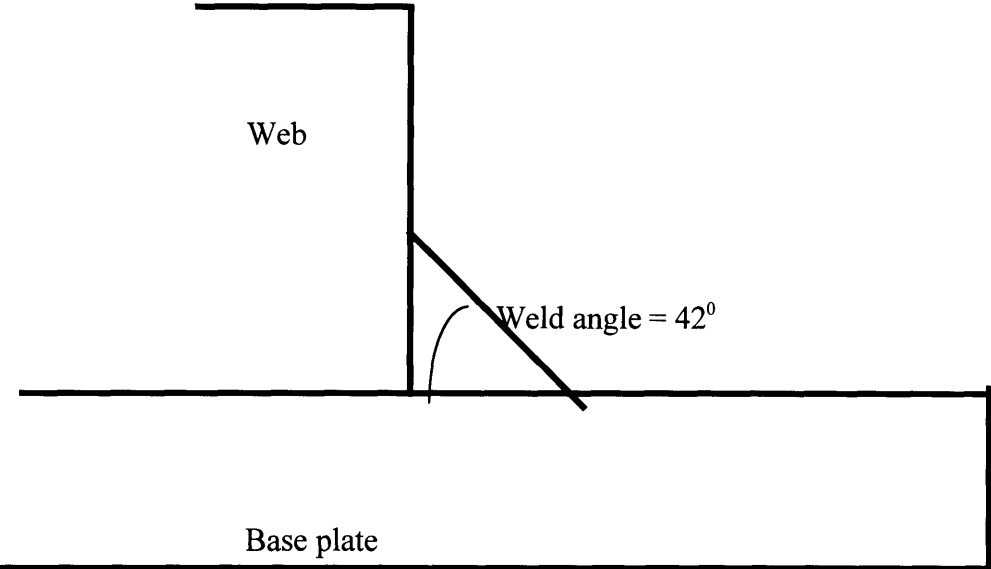


The weld metal is relatively homogeneous in the weld region. This behavior does not include the weld HAZ. For more information about this microhardness research, please refer to:

Figure 4-1 Cross section of a fillet weld for hardness measurement, with an undercut exist at the vertical toe of the weld (TSR 56, 1996).



a) Specimen 5



b) Specimen 6

Figure 4-2 Geometry difference of Specimen 5 and Specimen 6.

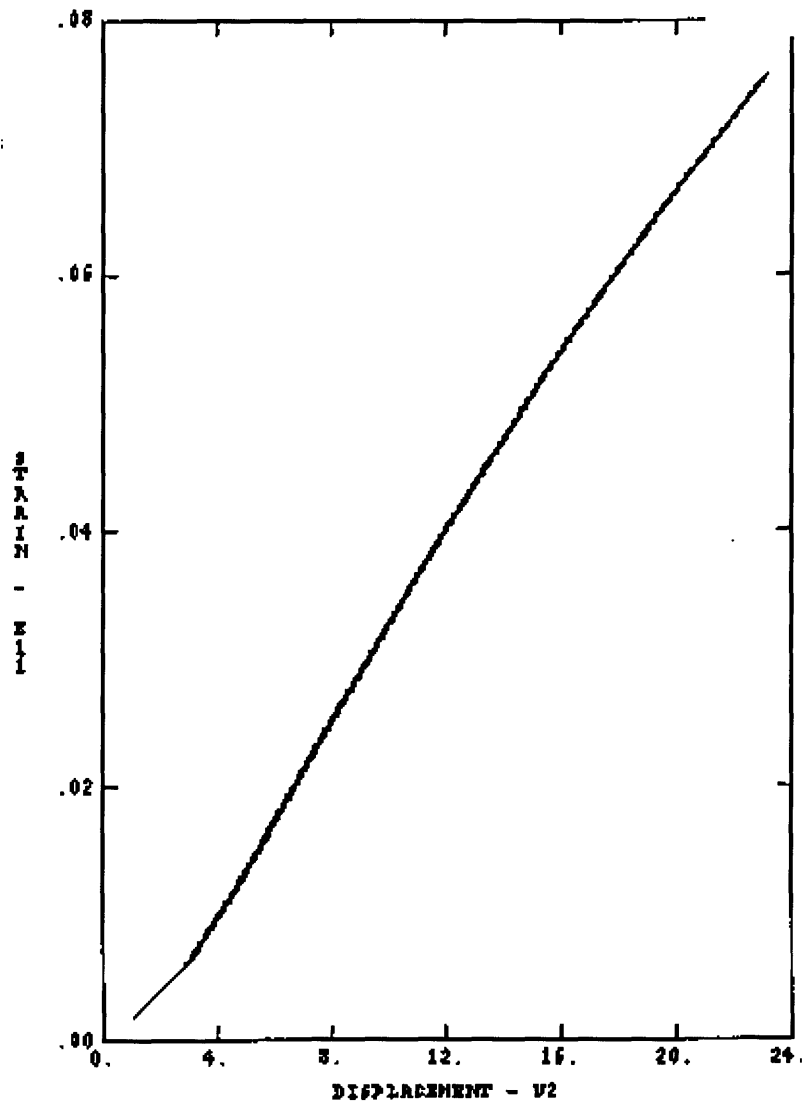


Figure 4-3 Displacement vs. nominal strain for the geometry of the experiments simulated by FEM.

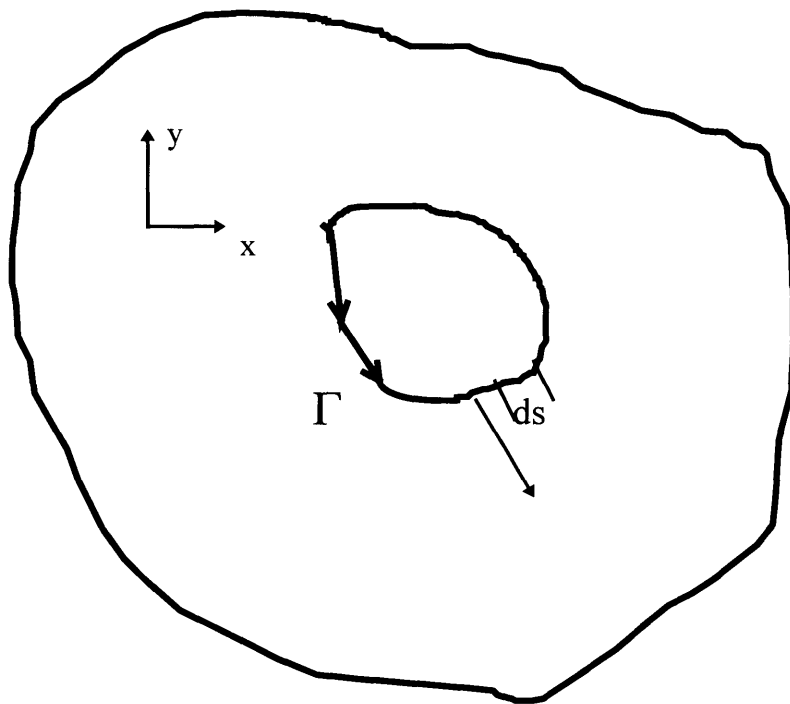


Figure 4-4 Definition of J-integral.

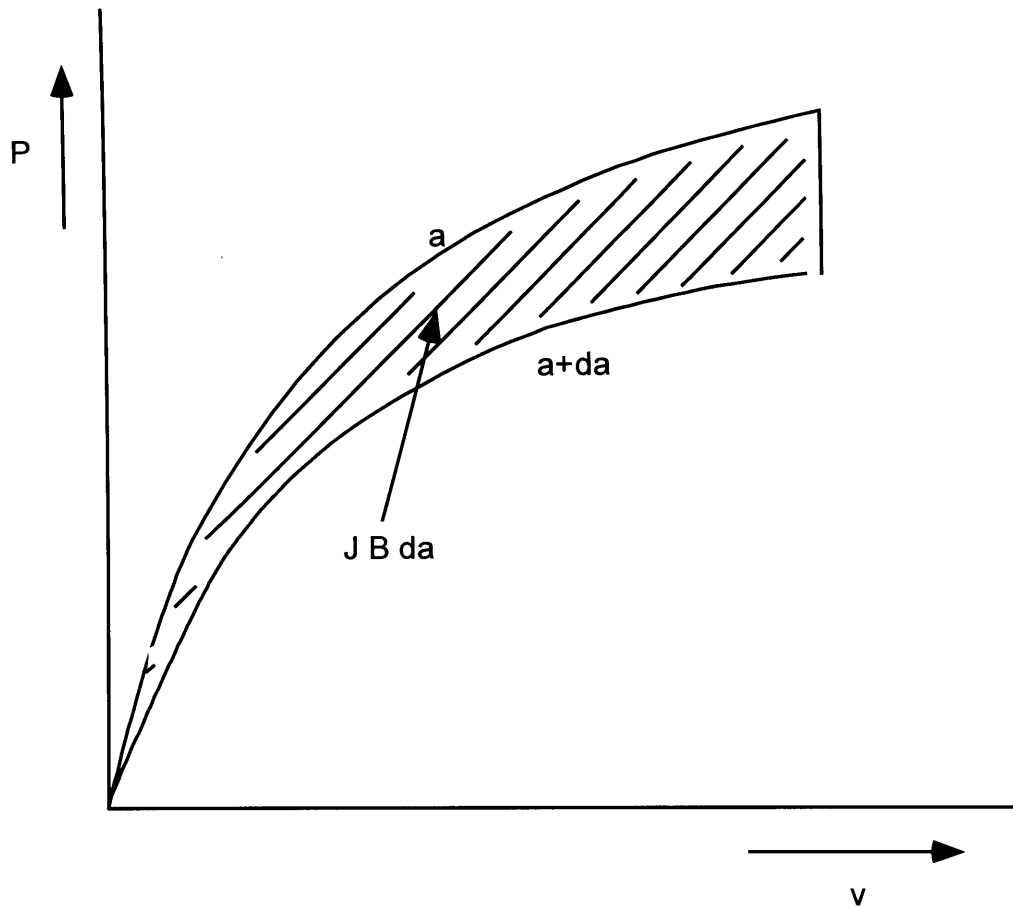


Figure 4-5 Load displacement diagram for cracked body of non-linear elastic material.

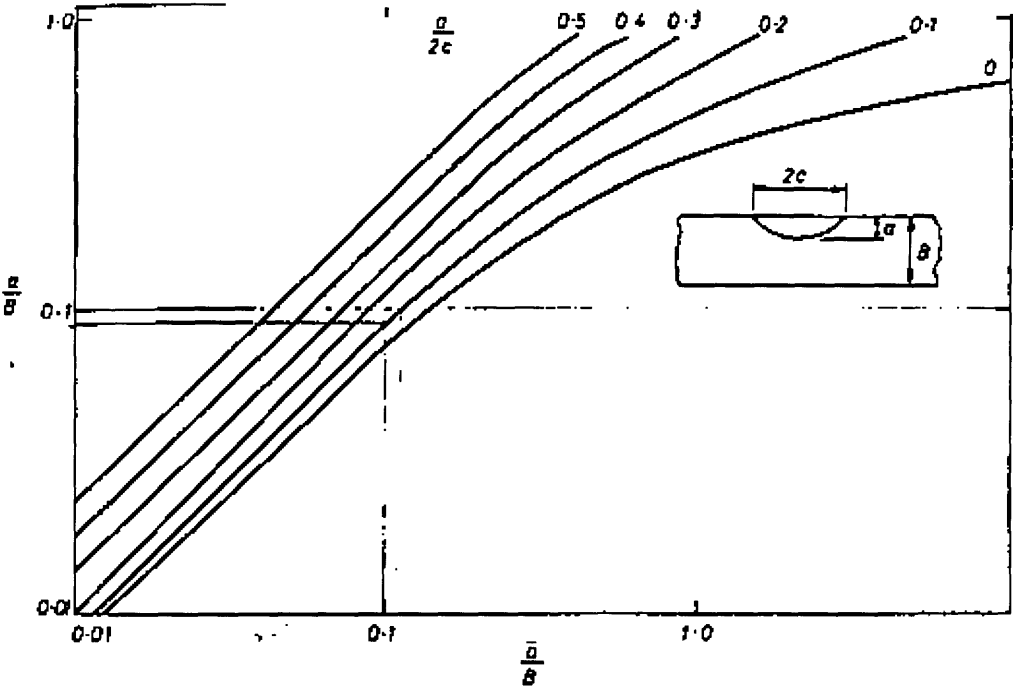


Figure 4-6 Relationship between a surface crack dimensions and equivalent through thickness crack dimension [Harrison,1978].

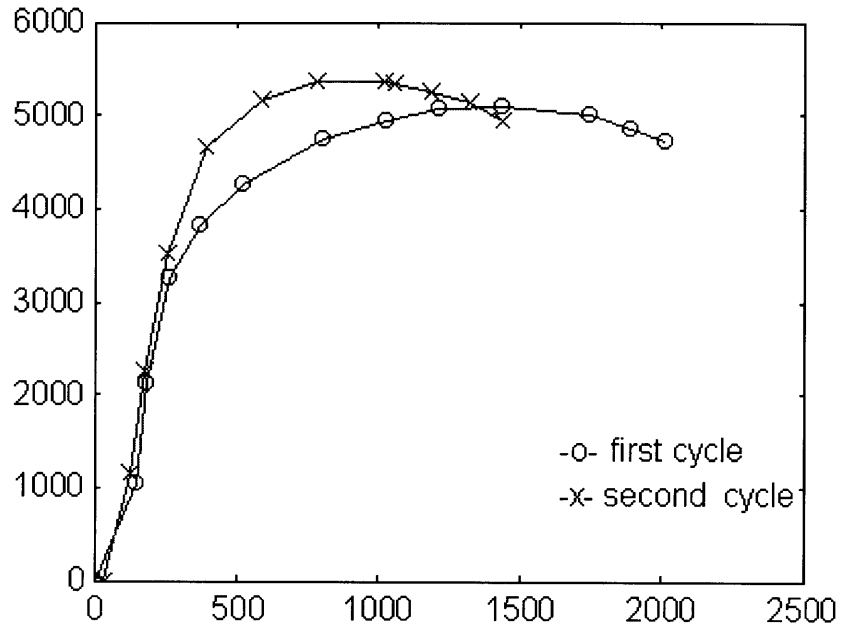


Figure 4-7 Specimen 5 load vs. displacement curves.

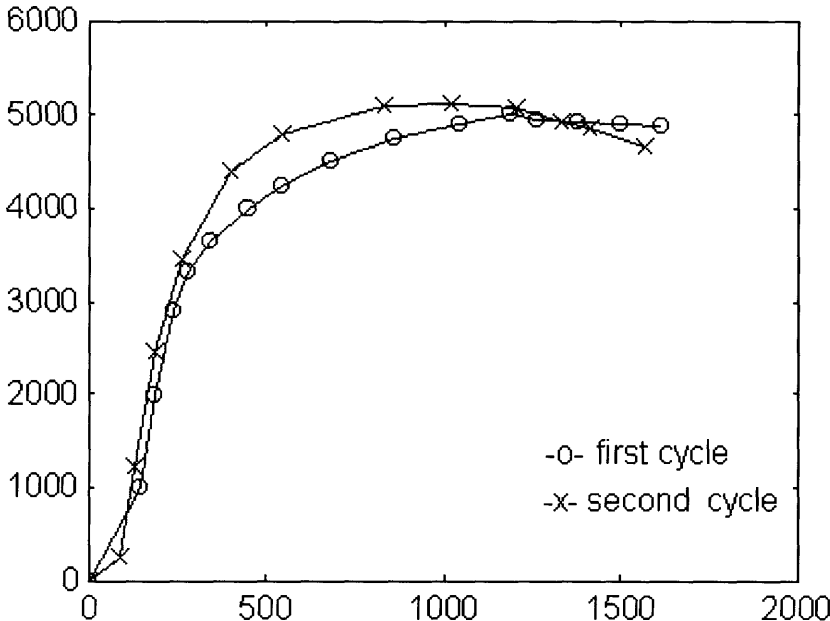


Figure 4-8 Specimen 6 load vs. displacement curves.

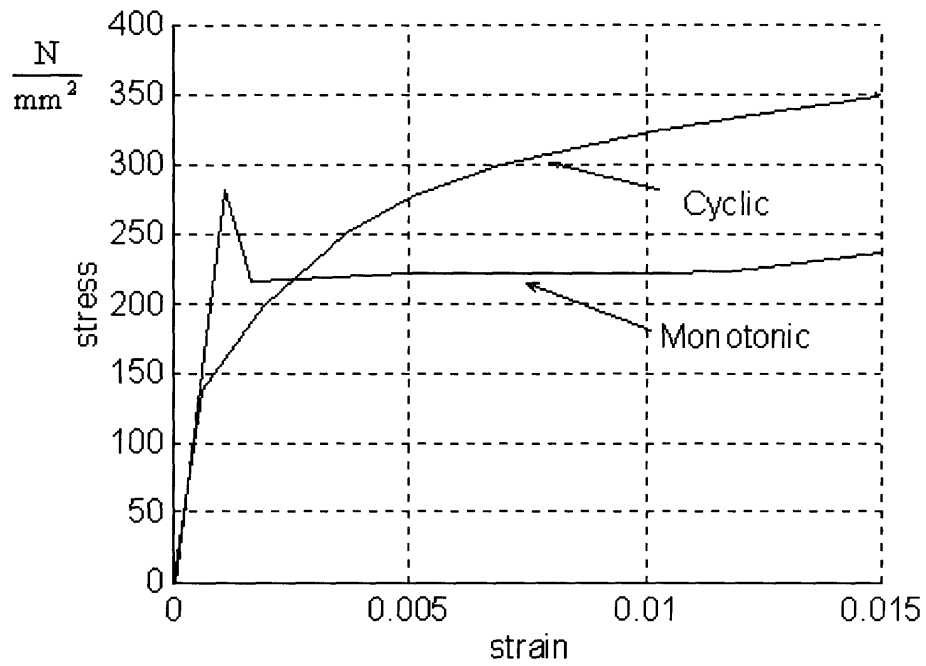


Figure 4-9 Comparison between monotonic and cyclic stress-strain curves for ASTM A-36 structural steel [Radaj,1990].

Chapter 5 An Analysis of the Plastic Failure of the Base Plate near the End Fillet Weld

5.1 Overview

This chapter is a study of the phenomena of the failure which happened near the vicinity of the end fillet of a weld caused by a large strain concentration due to discontinuity of the weldment. Larger constraint in the form of tensile to bending ratio was applied to Specimen 7 compared to the Specimens 5 and 6 studied in Chapter 4. To achieve this purpose, the specimen dimensions were modified and the ends of the base plate were bolted down while applying a three point bending deformation and end moment due to bending.

In Chapter 2, as shown by Figure 2-5 and Figure 2-6, the fracture might have started on the structure plates from the area very close to the fillet weld when load or displacement was applied to or transferred to these local areas. The picture of failure of the scalloped end of a steel beam during the Kobe earthquake shows that the crack started from a diaphragm plate near a weld (Figure 2-7) [Toyota, 1995]. The fatigue crack on the side longitudinal of the very large crude oil carrier also gave us the same information (Figure 2-5 and Figure 2-6) [Nobutaka, 1996]. However, the details of loads applied to those local areas are still unknown.

Assumptions are made as the load is a combination of bending and tension, whereas the bending is dominant. In the experimental test, the ends of the specimen were bolted on the supports when the displacement load of the bending was applied. Figure 5-1 shows the specimen setup with the supporting ends bolted tightly on the specimen. The web thickness was also increased from 9mm (3/8 inches) to 38mm (1.5 inches) compared to Specimen 5 and Specimen 6 in the previous chapter. Also, the leg length of the end fillet weld was increased from 7~8 mm for specimens 5 and 6 to 16mm for Specimen 7. The purpose of dimensional changes was to increase the constraint near the local area of end weld. With these changes of the experimental setup and Specimen

dimension design, we were able to have the rupture happen at the “desired” location simulating the actual failures of steel structures on the base plate. The final failure picture of Specimen 7 in Figure 5-2 shows the plastic fracture of the base plate near the end fillet weld. In this chapter, an analytical approach is applied in this chapter and checked with the experimental data by applying the failure criterion of a critical displacement v_{pe} for tearing of a base plate from the end of a stiffener model [McClintock et. al.,1996; McClintock, 1997].

5.2 Theories Applied

In another report of this oil tanker collision project, entitled “An Analysis of the Tearing of a Base Plate from the End of a Stiffener”, McClintock suggests three modes for the rupture of bending of a reinforced plate, which are described in Sec. 5.2.1. (Figure 5-3). In addition, in order to relate the repeated load effects on the specimen to the monotonic loading, the very low cycle fatigue theory is used in this study.

5.2.1 Bending and tension combined load vs. pure bending moment

The theory of pure bending of elastic-plastic beams can be extended to beams subjected to the axial force P , and the bending moment M . This theory is based on the assumption that the deflection is so small that the additional bending moment resulting from the axial force acting over the deflection, the so called $P-\Delta$ effect, is negligible [Shakir-Khalil and Tadros, 1973]. In order to investigate the effect of the axial force P on our specimen, this theory was applied to our specimen which was bolted at both ends. For a rectangular beam of non hardening material with width w and depth t , the moment and axial force can be calculated as

$$\begin{aligned} M &= \sigma_Y w (t^2/4 - y_0^2) , \\ P &= 2\sigma_Y w y_0 . \end{aligned} \quad 5-1$$

By defining normalized moment (m), load (p), and offset (η) of the neutral axis by $m=M/(\sigma_Y w t^2/4)$, $p=P/\sigma_Y w t$, and $\eta=2y_0/t$, Eqn. 5-1 gives

$$m=1-\eta^2, \quad p=\eta . \quad 5-2$$

In this case, the yield locus can be described in explicit form

$$m=1-p^2 \quad . \quad 5-3$$

This relation can be seen in Figure 5-4 [Lubliner,1973]. We assumed the friction coefficient between the supporting blocks and the testing machine support table to be $\mu=0.15$. By calculating the friction force as a function of normal force, which is one half of the loading force P , the axial force existing in the specimen in Specimen 7 setup can be calculated. Using Figure 5-4 or applying Eqn. 5-3, the actual applied bending moment of this combined loading can be calculated (for calculation, see Sec. 5.4).

5.2.2 Tearing of the base plate at the web end

As shown in Figure 5-3, most of the plate bends around an axis perpendicular to the web. The part of the base plate beneath the web and fillet weld is defined as a pedestal [McClintock,1997]. In Mode I, the deformation is considered as purely bending the specimen across the entire width of the plate length L_e . This mode obviously gives an upper bound to the bending load on the specimen. In case of collision, Mode I is the most desirable scenario to be expected. In Mode II, the base plate is assumed to slide off around the pedestal. This mode may give us an approximation of a lower upper bound to the bending load before the formation of plastic failure on the base plate at the end weld. In this case, the fillet weld has to be relatively large enough to ensure that the weld does not fail before the locally strain concentrated base plate is torn off.

A simple judging criterion was given for the condition of shearing off along the end of the web fillet weld by McClintock, 1997

$$t_w+2d_{sp}>t \quad . \quad 5-4$$

In this inequality, t_w is the thickness of the web, d_{sp} is the horizontal leg length of side fillet weld, t is the thickness of the base plate. This was proved by simply substituting the dimensions of Specimen 7 into the inequity above ($t_w=38\text{mm}$, $d_{sp}=7\text{mm}$, $t=19\text{mm}$, $38+2 \times 7=52>t$). Our Experiment showed that the pedestal was sheared off along the end of the weld on the base plate rather than the weld. Another criterion was given for the condition of sliding off along the sides of the web fillet welds as below

$$\frac{d_{ew}}{t} \left(\frac{\kappa_{fe}}{\kappa_p} \frac{t_w}{t} + 2C_{vs} \frac{\kappa_{fs}}{\kappa_p} \frac{d_{sw}}{d_{ew}} C_L \right) < \frac{1}{2} \frac{t_w}{t} \frac{1}{C_v C_L} \quad . \quad 5-5$$

where

d_{ew} is the vertical leg length of the fillet weld at the web end,

t is the thickness of the base plate,

C_{vs} is a number which is chosen as 1/4,

C_L is 1,

C_v is a 1/3,

d_{sw} is the vertical leg length of the fillet weld along the side of the web,

t_w is the web thickness,

κ_{fe} is the shear strength of the end fillet weld,

κ_p is the shear strength of the plate,

κ_{fs} is the shear strength of the side fillet weld.

By substituting the numbers from the test, the left hand side of the inequality is about 2.65, whereas the right hand side is 3, which means that the condition of the shearing off along the sides of the web fillet welds is not held in the test situation. Using the above two inequities (Eqns.5-4 and 5-4), we can estimate where the fracture will happen.

It seems that Mode II failure often happens when the weld is designed to be strong enough upon collision or grounding accidents. However, Mode II simplifies the situation by assuming that the tearing path is closely along the web or pedestal after the crack tips turn over the corners of the web. Figure 5-5 schematically shows the difference between this model and the real situation. To simplify the calculation in 2 dimensions, the difference caused by this assumption was tolerated in our study. As discussed above, when the criterion of shearing off the end fillet weld is satisfied, the interest was mainly focused on the shearing the base plate off at the toe of the end fillet weld. The third mode is the shearing off weld from the web which requires much higher load force and curvature. We assume that mode III has the least chance of happening during the ship collision and grounding accidents. Due to the limits of the machine, in our experiments,

we were not able to get the third mode phenomenon unless the weld sizes could have been scaled down.

The above arguments show that the second mode is the closest to our experiment design and results. Thus, the second mode criterion v_{pec} is applied to judge whether the specimen fails or not on the base plate near the end fillet weld. In “An Analysis of Tearing a Base Plate from the End of a Stiffener” (1997), McClintock defines the initial displacement at the end weld v_{pe} as a criterion to judge when the crack on the base plate at the end weld starts. This displacement can be calculated from the curvature of the bent base plate at the end weld.

For a power law material with $\sigma = \sigma_1 \varepsilon^n$, the curvature κ of a plate being bent of width w and thickness t is defined as the below Eqn.5-6 (Chakrabarty,1987). In Eqn.5-6 x is defined as the position coordinate within the peeling region L

$$\kappa = \frac{1}{t/2} \left[\left(1 + \frac{n}{2} \right) \frac{M_L (2x/L - (x/L)^2)}{\sigma_1 t^2 / 4} \right]^{1/n} . \quad 5-6$$

In Eqn. 5-6, κ can be dimensionally normalized by $t/2$, and the bending moment by $\sigma_1 t^2 / 4$, which are shown in Eqn. 5-7

$$\kappa = \left[\left(1 + \frac{n}{2} \right) M_L (2x/L - (x/L)^2) \right]^{1/n} . \quad 5-7$$

In order to further simplify calculation, a less complicated empirical form was introduced by McClintock (1997)

$$\kappa = \left[\left(1 + \frac{n}{2} \right) M_L (x/L)^a \right]^{1/n} . \quad 5-8$$

In Eqn. 5-8, the exponent a is an empirical number which ranges from 0.1 to 1 (In this study, $a=0.3$). Eqn. 5-8 gives a simpler relationship between the curvature and the bending moment as a function of position coordinate x within the peeling region L (See

Figure 5-3). Material properties are taken into account by incorporating the strain hardening factor n , which is the exponent of power law simulation in $\sigma = \sigma_1 \varepsilon^n$.

If only the moment and curvature at the end fillet weld are considered, $x/L=1$ gives

$$\kappa = \left[\left(1 + \frac{n}{2} \right) M_L \right]^{1/n} \quad 5-9$$

According to McClintock (1997), the relation between the displacement and bending moment M of unit width can be solved by the following equation below

$$v_{pe} = C_{Lpe} \left(\frac{w - t_w - 2d}{t_w + 2d} \right)^{1/(1+n)} \frac{\theta_L^{(1+2n)/(1+n)}}{a/n + 2} \quad 5-10$$

where

t_w is the web thickness of the specimen,

d is the horizontal leg length of end fillet weld,

w is the width of the base plate,

n is the strain hardening exponent of the material,

a is the empirical number which is 0.3,

θ_L is the bending angle of the plate at L position,

C_{Lpe} is a coefficient which is a function of material exponent n .

C_{Lpe} is defined by Eqn 5-11 to simplify the expression of the Eqn. 5-10

$$C_{Lpe} \equiv \left(\frac{nC_b}{C_e} \right)^{1/(1+n)} \quad 5-11$$

$$C_b = \frac{\left(\frac{a}{n} + 1 \right)^{1+n}}{(1+n)(1+0.5n)\left(\frac{a}{n} + a + 1\right)}$$

$$C_e = \frac{1.5n^n e^{-n}}{\frac{a}{n} + 2}$$

where

C_b is the coefficient of the bending moment resistance,

C_e is the end resistance coefficient.

The relation between θ_L and the bending moment M is given in Eqn 5-12

$$\theta_L = \frac{(wM/C_{Mpe})^{1+1/n}}{(t_w + 2d)(w - t_w - 2d)^{1/n}}, \quad C_{Mpe} \equiv \frac{1+2n}{1+n} \left(\frac{C_h}{C_{Lpe}^n} + C_e C_{Lpe} \right). \quad 5-12$$

With Equations from Eqn. 5-10 through Eqn. 5-12, v_{pe} can be expressed by a function of bending moment, and the numerical calculation can be performed with the help of Maple software. By substituting κ with M by Eqn. 5-8, the relation between the displacement v_{pe} and curvature κ of the base plate at the end of the weld can be obtained. This is a function of dimensions of weldment and material characteristics in term of coefficient C_{Lpe}

$$v_{pe} = C_{Lpe} \frac{\kappa^{1+2n}}{\left(\frac{t_w + 2d}{w}\right)^2 \left(1 - \frac{t_w - 2d}{w}\right)^{1/n}}. \quad 5-13$$

This relation can be applied directly for grounding or collision of oil tankers as a criterion for the rupture of welded structure, if the curvature of the indentation is known.

5.2.3 Low cycle fatigue for repeated loading

It should be stated that in the second mode of tearing of base plate from the end of a stiffener, monotonic loading is assumed. Nevertheless, in the experiment, the fracture of the base plates happened after 3.5 cycles of loading. In order to incorporate the effect of cyclic loading, the theory of very low cycle fatigue, which relates load cycles n_f and strain, was applied to very low cycle fatigue calculations. Here, ε_f is the failure strain. $\Delta\varepsilon_{rev}$ stands for the amplitude of reversible strain. The number of cycle of the fatigue failure is denoted as n_f

$$1 = n_f (\varepsilon_f / \Delta\varepsilon_{rev})^{0.5}. \quad 5-14$$

Assuming this relationship would still hold for the displacement, we build our a new equation which gives the relation between displacement and number of cycles as shown in Eqn.5-15

$$1 = n_f (v_f / \Delta v_{rev})^b, \quad 5-15$$

where

v_f is the failure displacement,

Δv_{reve} is the reverse displacement,

n_f is the number of load,

b is an exponent which should be of the order of 0.2 to 0.8.

In our study, b is set to be 0.5. The base plate of our specimens was relatively narrow when it is compared to the thickness of the web. We can neglect the compound curvature and assume that the curvature of the bent plate is one dimensional and the plate is a beam in the calculation [McClintock, 1997].

5.3 Experiment Performance

This experiment was similar to the previous ones except that there were dimension changes of the specimen. As shown in Table 5-1, Specimen 7 was welded by GTAW welding process. The welding current was set to be about 140 A. Four passes were applied to bring both the vertical/horizontal leg lengths of the side welds and one end weld of lower load of this asymmetrical structure up to 9.5 mm. The size of the end weld, where the maximum load was applied to and in which we were particularly interested, was accumulated by seven passes. The 7 welding passes resulted in the increases of the horizontal leg length to be 11.7 mm and of the vertical leg length, 9.5 mm. The larger weld size is desirable to guarantee the weld not to fail if the specimen is subjected to extreme loading conditions. In addition, the web was beveled 3 mm to assure penetration when the first pass of weld metal was deposited. After welding, the area of interest was ground by a sand wheel to make a geometrically smooth surface. A one inch long notch, with a width of 1/16" (1.6 mm) and depth of 1/32" (0.8 mm), was machined on the base plate at the toe of the end fillet weld by an end mill. Two I-shape supporting blocks were also made using GTAW of 3/4" thick plates. The detail dimensions can be seen in Fig 5-1b. Two 5/8" holes were drilled on each of the supporters. Detail description of the specimen is listed in Table 5-1.

Table 5-1 Dimensional descriptions

base plate dimensions (mm)	web plate (mm)	leg size of side weld (mm)	leg size of end weld (mm)
316x127x19	101x63x38(beveled)	9.5	11.7
notch at the toe of end weld milling machine: depth 0.8mm (1/32"), length=19mm (3/4")			
effective arm length of the bending moment after bolted with supporters at the ends: 95mm.			
Specimen was welded by GTAW of current 140A.			

The material properties were obtained from the LUKENS STEEL's test certificate and MIT class 13.15 class handout. The tensile of the base material was chosen as 524MPA. Table 5-2 gives detailed information.

Table 5-2 Specimen 7 material descriptions

Material			
web and base plate		filler wire	
web: *EH36 equivalent		TGS-50 (AWS A 5.18 ER70S-G)	
σ_Y :406MPA	σ_T :519MPA	σ_Y : 340 MPA	σ_T 470 MPA

*Provided by NAVY without specifications, only labeled as EH-36 equivalent (Lt. Lee Boone, 1996).

Four 1/2 " diameter bolts were used to tighten the specimen with the supporters. 1mm x 1mm spacing grid was marked on the surface of the base plate near the toe of the end weld. This grid was designed to be used to measure the plastic strain history of the local area of the specimen during the period prior to occurrence of failure. The change of grid size was recorded by the video microscope while it was monitoring the failure process. With the measurement of still pictures printed out from the video printer, we obtained the surface strains at the toe of the end weld during different stages (Appendix-4).

The loads and displacements were read from the bending machine (Baldwin 60000) and gauge, and recorded simultaneously with the VCR recording. After the test, the still pictures of Specimen 7 were printed out from the video color printer. Each still picture corresponds to one loading moment. The load vs. displacement data were analyzed with Matlab software, and the moment vs. displacement curves were plotted.

After the fourth deformation (3.5 loads), the specimen was ruptured severely at the toe of the end weld at the base plate. The fracture surface was studied with higher magnification lens microscope of the video microscope. From the appearance of the fracture surfaces, conclusion was drawn that the failure is a plastic failure. Thus, the plasticity theory applied.

The load vs. displacement diagram (Figure 5-6) indicates that the second cycle load curve is higher than the first cycle load curve. This is caused by the strain hardening effect of the material. The reason that curve 3 and curve 2 dropped below curve 1 was because the crack had already started inside the base plates of specimen. However, curve 4 rose up again could be explained that more energy was needed to propagate the crack to the surface.

5.4 Calculations

From the load vs. displacement curves recorded during the test of the specimen, the bending moment vs. displacement curve for this test can be calculated. Figure 5-6 and Figure 5-7 show the load vs. displacement curves and the bending moment vs. displacement curves, respectively. The calculation of moment is similar to that as described in Chapter 3. A small Matlab program is attached in Appendix -3 for more detail information. In Figure 5-6, the maximum moment M_L is 55239 Nmm/mm. The exponent n for power law relation for the base plate steel is assumed to be 0.2 (0.17~0.24) in all the calculations in this chapter. We also assume the parameter $a = 0.3$ [McClintock, 1997].

The vertical leg length of the end fillet weld d is measured as 9.5mm; thickness of the web $t_w = 38 \text{ mm}$ (1.5"); the width of the base plate $w = 127 \text{ mm}$ (5"). With this known information, the coefficients C_b , C_e , C_{Lpe} , and displacement v_{pe} are calculated by using Maple V release 4 software (Appendix-3).

Table 5-3 The input parameters for calculating the coefficients

a	t_w	w	d (side fillet weld leg length)
0.3	38mm	127mm	9.5mm

As the material hardening exponent is assumed to be $n=0.2$, all the coefficients and displacement v_{pe} were calculated out as listed by Eqn. Maple V release 4 software which is attached in Appendix -3.

Knowing the bending moment when the crack started, the coefficients, curvature and v_{pe} are calculated out and listed in Table 5-4

Table 5-4 Calculation result of the displacement criterion

M_L and κ	$C_b(0.2)$	$C_e(0.2)$	C_{Lpe}	v_{pe}	$v_{pe}' = v_{pe} * t/2$ actual
$M_L = 6.425$ MN-mm				normalized value by $t/2(9.5 \text{ mm})$	dimensional value of the displacement of the pedestal at the end weld
$\kappa = 0.1475$	0.8124	0.2543	0.6885	0.14	1.33mm
Calculated from the measurement of failed specimen's fracture surface displacement $v_{pe}'' = a + b - c = 2.0 + 1.7 - 1.5 = 1.2 \text{ mm}$					

The numbers a, b, and c were measured from the post fracture surface of Specimen 7 (Figures 5-2 and 5-7).

If we take the mean value of $(v_{pe}'' + v_{pe}')/2 = 1.265 \text{ mm}$ as our measured displacement when the shear of the pedestal at the end weld started, we were able to define a critical

criterion to judge whether the base plate could be sheared $(v_{pe}'' + v_{pe}')/2$. Normalizing the $(v_{pe}'' + v_{pe}')/2$ by $t/2$, we got the dimensionless critical value v_{pec} (0.133) (Figure 5-8). The v_{pec} value is a critical criterion to judge whether the base plate can be sheared off. We draw this value in the displacement and curve diagram as a threshold line as shown in Figure 5-8.

5.5 Conclusions

The critical displacement of the shearing off the base plate from the end fillet weld, v_{pec} , can be calculated with rather simple equations. The vertical displacement of the pedestal v_{pe} is a function of structure geometry dimensions and the material properties including the yield strength power law exponent. We can use the plotted curve in Figure 5-8 in Section 5-4 to make our judgement that whether the base plate of the stiffener would be plastically shear off or not.

If the design of the oil tanker structure is fixed, the dimensions of the plate thickness (t), stiffener thickness (t_w) and the stiffener the half span between two stiffeners (w), are fixed, given that a certain curvature (κ) of the oil tanker structure upon grounding or collision, we can calculate the weld leg length (d) to make sure that the calculated v_{pe} is under the design of critical value v_{pec} . In this case, the failure of the fillet weld will not happen. However, the practically usable v_{pec} value should be obtained from more experiments.

On the other hand, if all the dimensions of weldment are fixed, we can easily estimate whether the base plate would be sheared off by a certain curvature κ , which is the product of tanker collision or grounding.

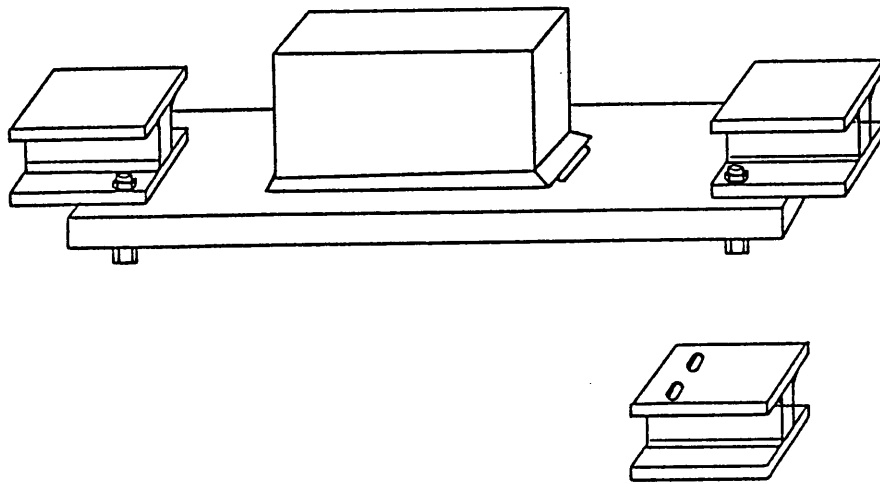
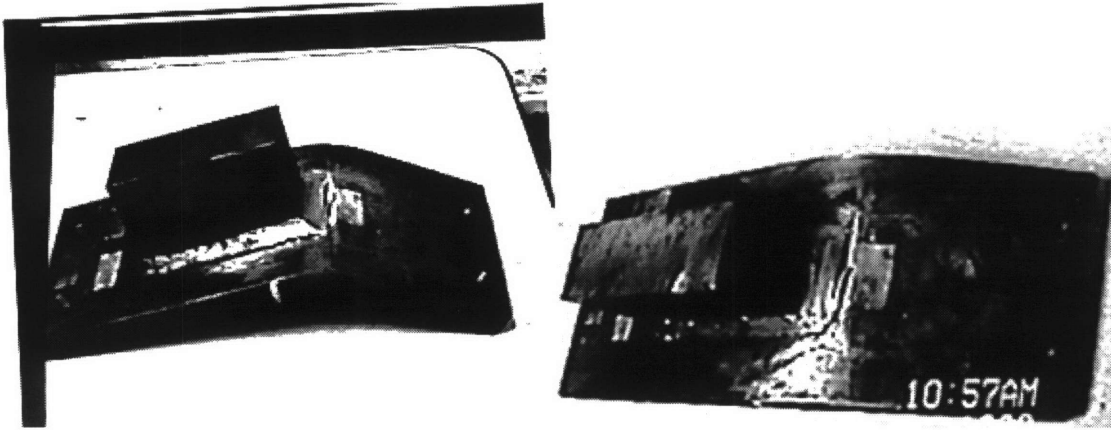
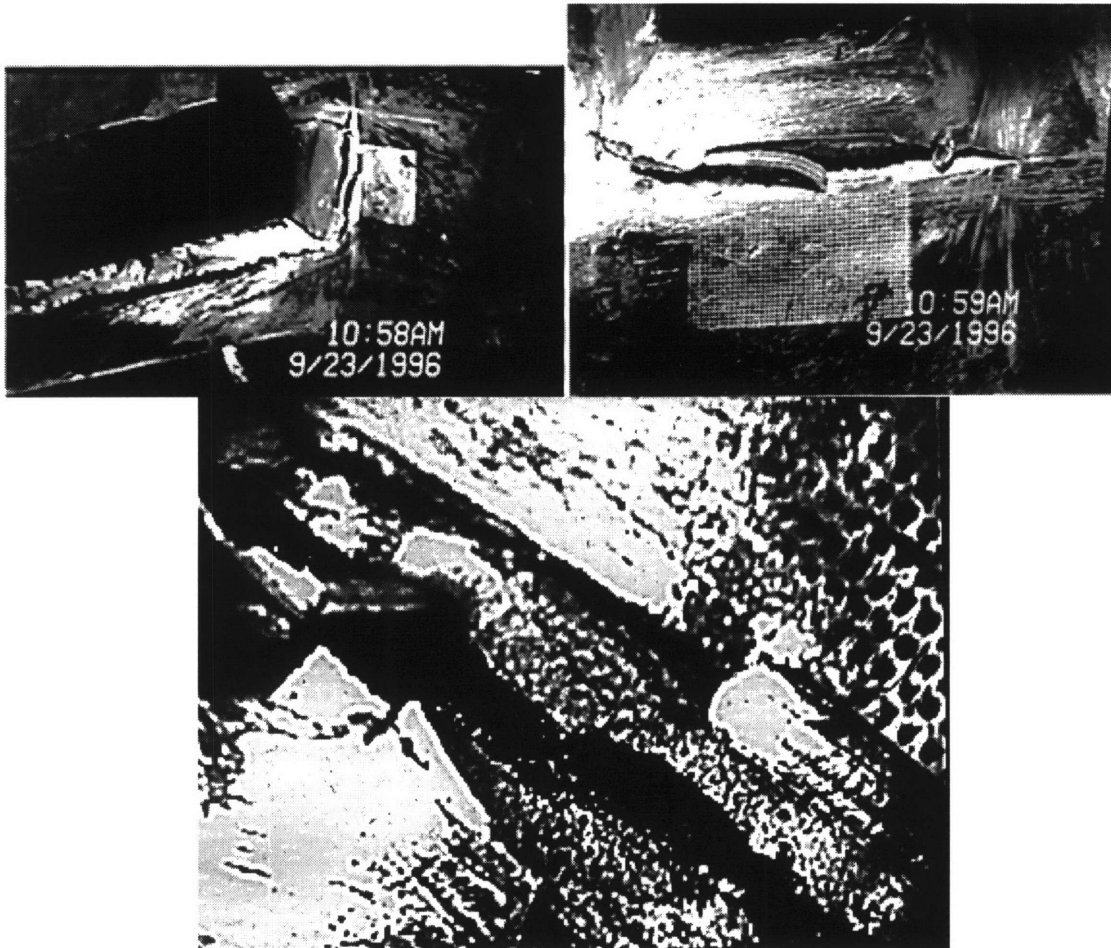


Figure5-1 Specimen setup with the supporting blocks.



a) Side view and Bird's eye view of Specimen 7 that failed after 4th cycle load



b) Closer views of the fracture of 7 specimen on the base plate near the toe of fillet weld

Figure 5-2 Pictures of failed Specimen 7 with the base plate shearing off at the toe of end weld

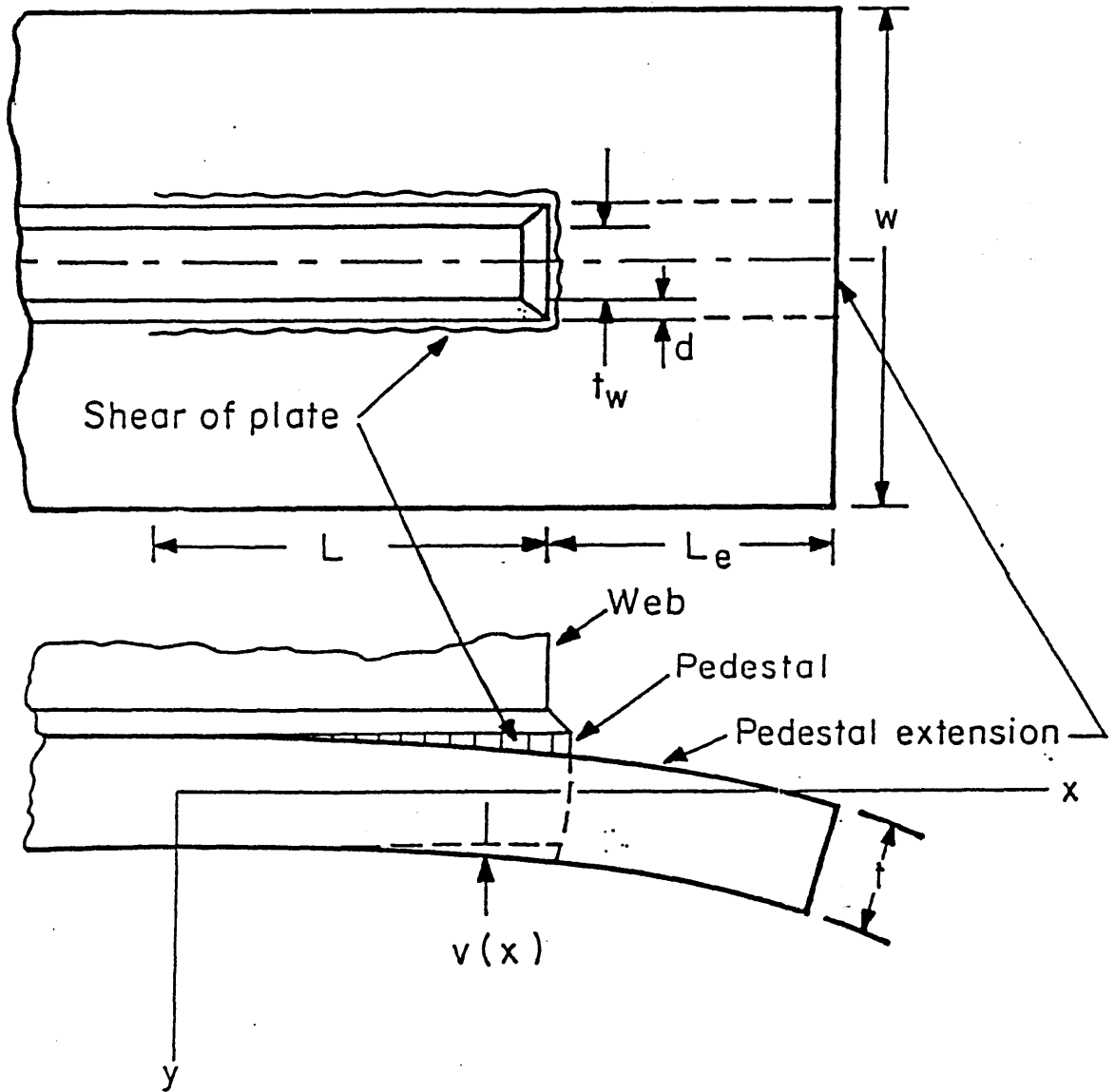


Figure 5-3 Schematic drawing of the base plate shearing off around the pedestal

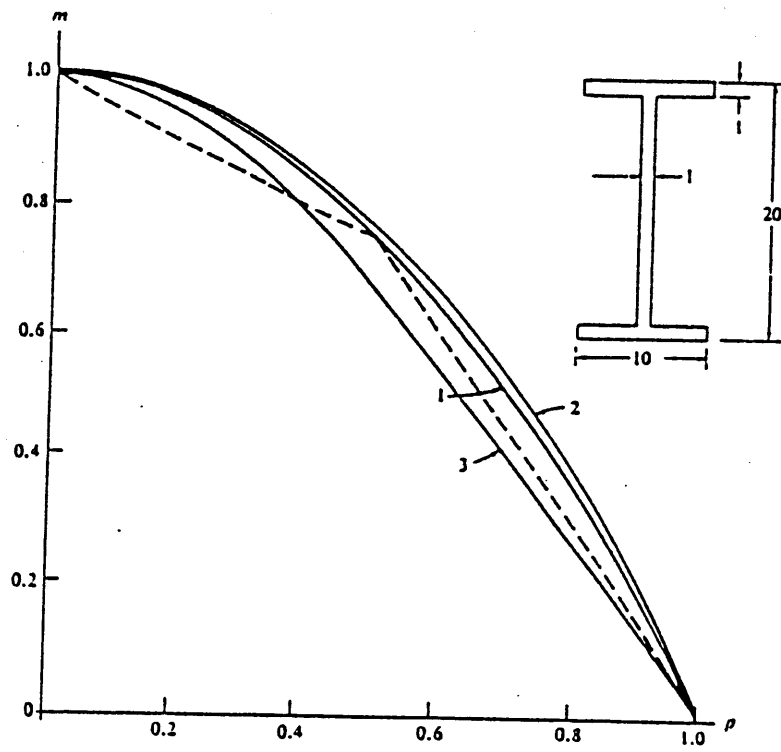
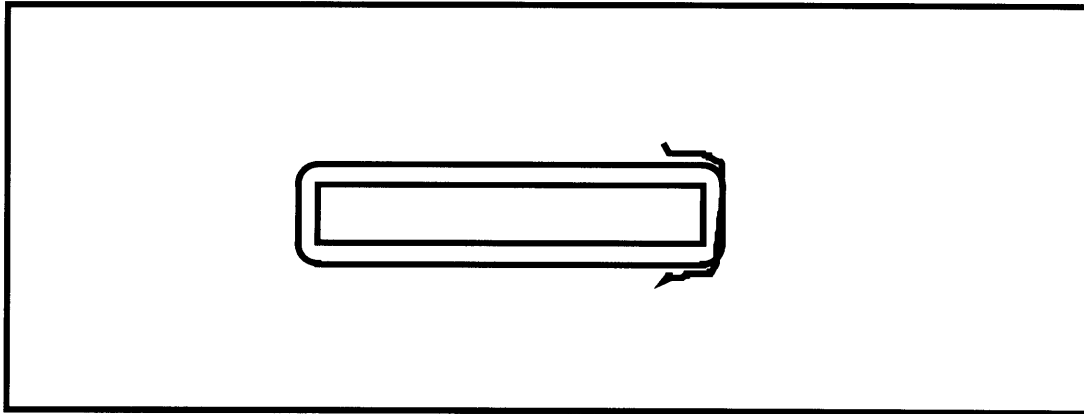
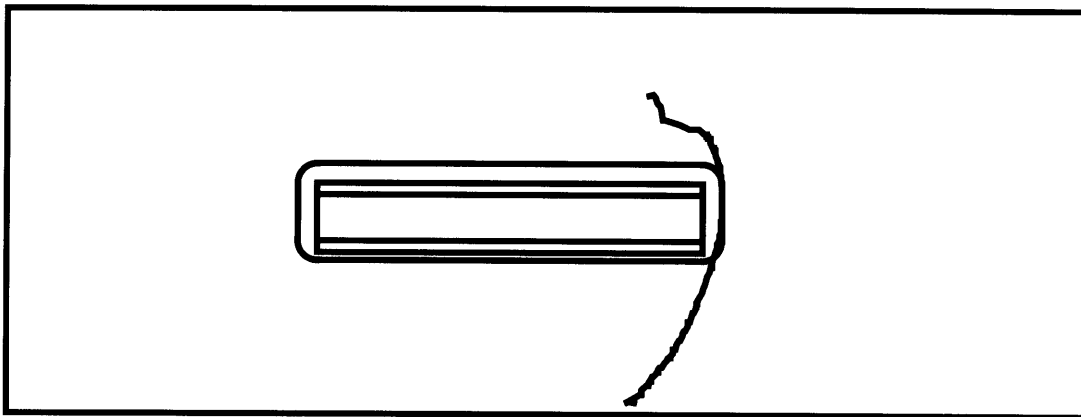


Figure 5-4 Combined load of tension and moment diagram.



a) Idealized tearing of the base plate is around the web which is easier for calculation



b) Real case of tearing of the base plate which the fracture path is not necessary along the web geometry.

Figure 5-5 The real case and idealized and model comparison

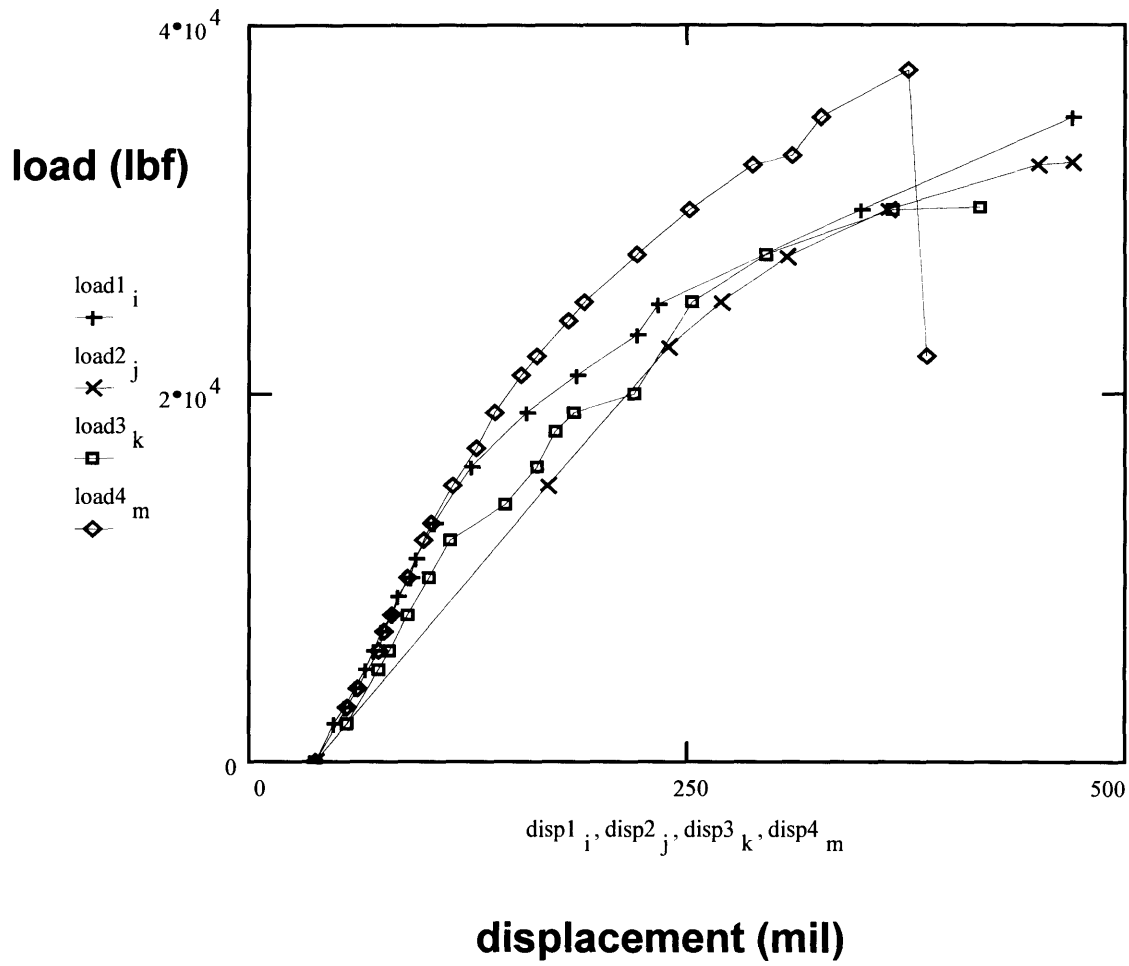


Figure5-6 Load vs. displacement diagram of the test

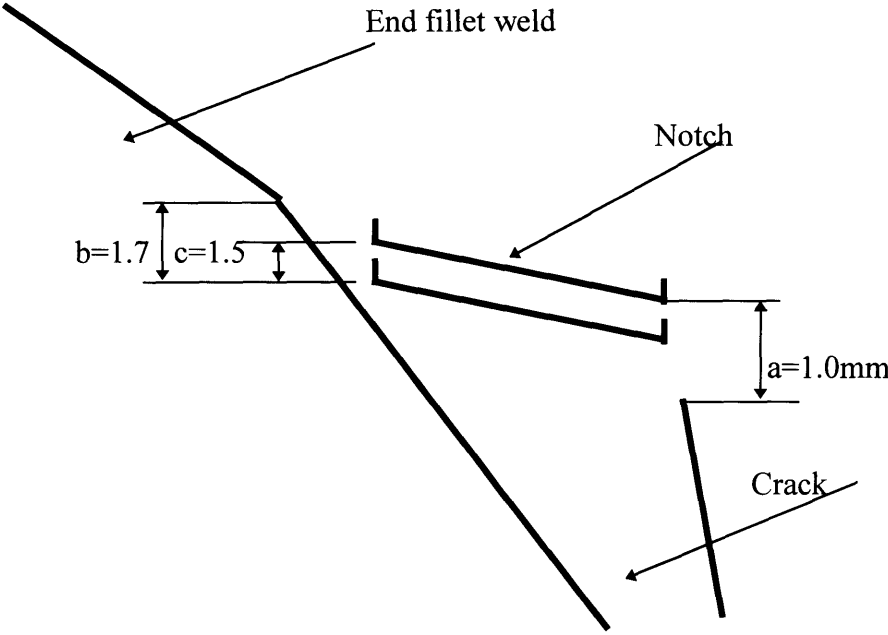


Figure 5-7 Schematic drawing of post fracture measurement of Specimen 7.

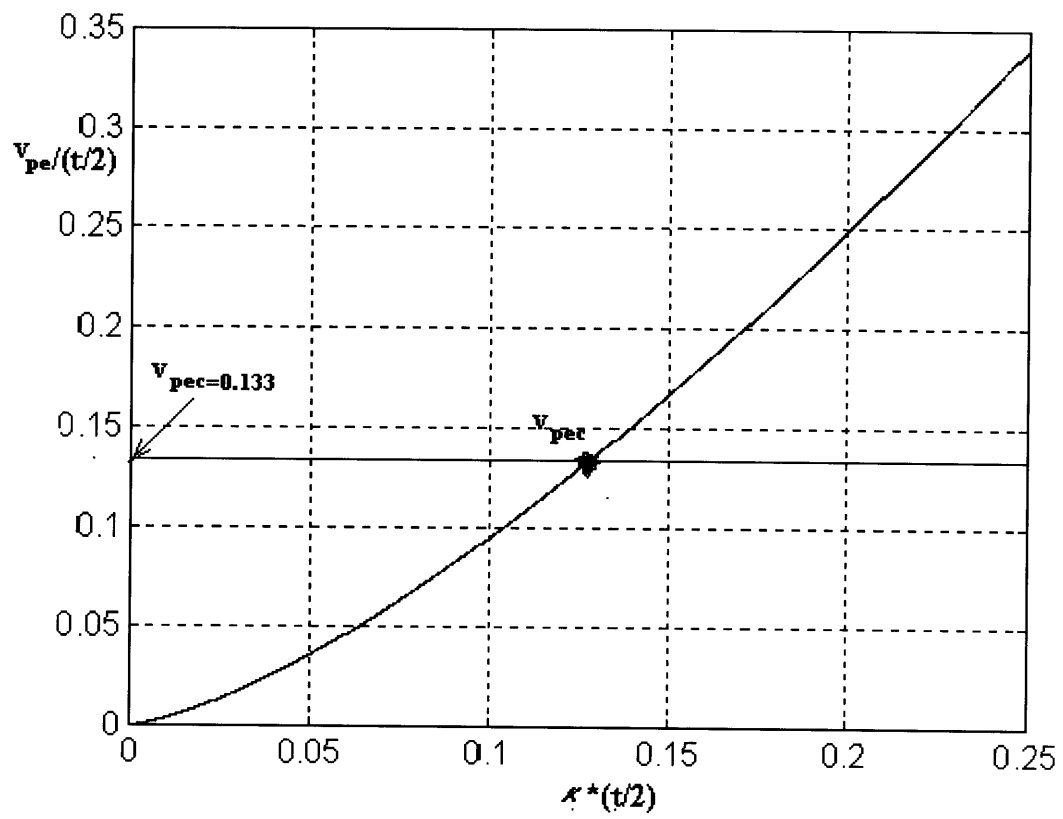


Figure 5-8 Curvature vs. displacement diagram of Specimen 7.

Chapter 6 Conclusions and Recommendations

6.1 Conclusions

1. Increasing the penetration of the fillet weld can increase the tensile strength of the fillet weld without increase much cost.
2. The numerical calculation (FEM) results matches the experiment results better if the penetration is considered. The measurement of the fusion line of the weld is an applicable method to give an accurate input of the weld contour line especially with the penetration.
3. Material characteristics can be simulated by the power law approach. However, this power law simulation is an approximation of the real materials.
4. Both experiments and calculation results have shown that fillet weldments that end suddenly are vulnerable when the structures are subjected to loading.
5. Locally increasing the penetration and weld size at the end weld may increase the strength of the fillet welded structure with a sudden end.
6. The geometrical parameters of the end fillet including weld angle and curvature of the weld toe are important for the fatigue strength of the structure.
7. An undercut at the end fillet weld toe has large negative effects on the fatigue strength of the structure.

8. Different loading patterns give different overall strengths of the structure.
9. The critical vertical displacement of the pedestal v_{pec} can be used to judge the tearing of the base plate when curvature of the plate is given.
10. The vertical displacement of the pedestal v_{pe} curves can also be used as design curves when the weldment dimensions need to be changed.

6.2 Recommendations

1. The material property of the heat affected zone (HAZ) and the weld metal should be more precisely divided with more accurate hardness measurement of the specimen. The reason of this recommendation is that the different specimen may have different hardness if the welding conditions are not exact the same. The micro hardness measurement is still too rough to simulate the material property of the narrow area including weld metal and HAZ. A better simulation of the material might be needed for the FEM calculation.
2. The tear work per unit length of the weld metal is an average number. This calculation has not considered the geometry dimension effects of the weldment. It does not relate the curvature of the base plate to the failure of the fillet weld directly. The tearing off on the side fillet weld mode of failure presented in [McClintock, 1997],

might be an approach to check the results. However, new experiments and calculation need to be performed.

3. To make the criterion of the vertical displacement v_{pec} a valid criterion for practical use, more experiments are needed to be done. A simple device which can measure the vertical displacement of the pedestal v_{pe} may be suitable to get more data for the calculation. An ordinary camcord is enough to monitor this device simultaneously with the micro video recorder.
4. The dimension parameters of the v_{pec} criterion function might be able to be separated by performing more experiment with different dimensions for specimens. This experiment may give more intuitive understanding for design purpose if the data are carefully checked with the calculations.

References

1. Robert Taggart. *Ship Design and Construction*. SNAME, 1980.
2. Jordan, C. R., Cochran, C. S., *In-Service Performance of Structural Details*. SSC-272. Ship Structure Committee, 1978.
3. O. H. Burnside, S. J. Hudak, E. Oelkers, K. Chan, R. J. Dexter. *Long Term Corrosion Fatigue of Welded Marine Steels*. SSC-326. Ship Structure Committee, 1984.
4. Petershagen, H., Fatigue problems in ship structures. *Advances in Marine Structures*. C. S. Smith, R. S. Dow. Elsevier Applied Sciences, 1986.
5. Munse, W. H., Fatigue Criteria for Ship Structure Details. *Extreme Loads Response Symposium*. SNAME, 1981.
6. H. A. McDonald. *Required Strength and Tear Resistance for Fillet Welds in Ships Exposed to Grounding or Collision Loads*. M.S. Thesis, M.I.T. Department of Ocean Engineering, May, 1993.
7. Kunihiro Iida. Very low cycle fatigue life influenced by tensile or compressive prestrain. *Low Cycle Fatigue*. ASTM STP 942. H. T. Solomon, G.R. Halford, L. R. Kaisand, B. N. Leis. American Society for Testing and Materials, 1988.
8. Owen F. Hughes. *Ship Structural Design*. SNAME, 1988.
9. Bradley Dodd, Yilong Bai. *Ductile Fracture and Ductility*. Academic Press, 1987

10. D. Broek. *Elementary Engineering Fracture Mechanics*. Kluwer Academic Publishers, 1991.
11. T. L. Anderson. *Fracture Mechanics*. CRC Press, 1995.
12. Drar, H., On predicting the temperature and strain rate dependences of the fracture toughness of plain carbon steels. *Materials Characterization*, 31, 91-97. Elsevier Science Publishing Co, 1994.
13. H. O. Fuchs, R. I. Stephens. *Metal Fatigue in Engineering*. Wiley, 1980.
14. Djiubinski J. , Adamiec P., Brunne W. A Welded joint microstructure effect on low-cycle fatigue. *Low Cycle Fatigue and Elastoplastic Behavior of Materials*. K.-T.Rie. Elsevier Applied Science, 1987.
15. K. Shimada, J. Komotori, M. Shimizu. Fracture mode transition and damage in extremely low cycle fatigue. *Low Cycle Fatigue and Elastoplastic Behavior of Materials*. K.-T.Rie. Elsevier Applied Science, 1987.
16. Havas I., Czoboly E.. Effect of low-cycle fatigue on the brittle characteristics of a structural steel. *Low Cycle Fatigue and Elastoplastic Behavior of Materials*. K.-T.Rie .Elsevier Applied Science, 1987.
17. M. Schwartz, J. C. Crespi. Fracture of pearlite under conditions of high deformation fatigue. *Low Cycle Fatigue*. ASTM STP 942. H. T. Solomon, G.R. Halford, L. R. Kaisand, B. N. Leis. American Society for Testing and Materials, 1988.

18. B. N. Leis. A nonlinear history-dependent damage model for low cycle fatigue. *Low Cycle Fatigue*. ASTM STP 942. H. T. Solomon, G.R. Halford, L. R. Kaisand, B. N. Leis. American Society for Testing and Materials, 1988.
19. T. Kunio, M. Shimizu, N. Ohtani, T. Abe. Microstructural aspects of crack initiation and propagation in extremely low cycle fatigue. *Low Cycle Fatigue*. ASTM STP 942. H. T. Solomon, G.R. Halford, L. R. Kaisand, B. N. Leis. American Society for Testing and Materials, 1988.
20. T. Nakatsuji, T. Fujimori. A study on engineering critical assessment of weld defects in steel building constructions-Behavior of welded joints including weld defects under ultra-low cyclic large strain deformations. *Criteria For preventing Service Failure in Welded Structures*. The Third International Symposium of the Japan Welding Society, 1978.
21. Taijiro Nonaka, Satoshi Iwai. Failure of bar structures under repeated loading. *Structural failure*. Thomasz Wierzbicki, Norman Jones. Wiley, 1988.
22. Helmut Krawlinkler, Mahmud Zohrei. Cumulative damage in steel structures subjected to earthquake ground motions. *Computers & Structures*. Vol. 16, No 1-4. Pergamon Press, 1983.
23. Tsai, C. L., Itoga, K., Malliris, A. P., McCabe, W. C., Masubuchi, K., *Review of Fillet Weld Strength Parameters for Shipbuilding*. SSC-296. Ship Structure Committee, 1980.

-
24. R. P. Krumpfen, Jr. and C. R. Jordan. *Updating of Fillet Weld Strength Parameters for Commercial Shipbuilding*. SSC-323. Ship Structure Committee, 1983.
 25. Koichi Masubuchi. *Analysis of Welded Structures*. Pergamon Press, 1980.
 26. Frank A. McClintock. *Fully Plastic Mechanics of Welded T-Joints*. Report 26, Joint MIT-Industry Program on Tanker Safety, 1994.
 27. A. G. Atkins, Y.W. Mai. Residual strain energy in elastoplastic adhesive and cohesive fracture. *International Journal of Fracture*, 33:285-295, 1987.
 28. Min Du Chang, K. L. Devries, M. L. Williams. The effects of plasticity in adhesive fracture. *Journal of Adhesion*. 4:221-231, 1972.
 29. Yukito Hagiwara. Evaluation of brittle fracture strength from surface notch at fillet weld toe based on CTOD criterion. *J.S.N.A. Japan*. 157:223-232, 1985.
 30. Susumu Machida, Hitoshi Yoshinari, Yukito Hagiwara. Study on fracture strength assessment. *J.S.N.A. Japan*. 171:113-126, 1992. Masakazu Onozuka, Osamu Ushirokawa, Yasushi Kumakura, Isamu Tsuji.
 31. The influence of bead toe shapes on the fatigue strength of fillet welded joints- Fabrication acceptance criteria for undercut depth. *J.S.N.A. Japan*. 170,171:85-98, 1992.
 32. X. Niu, G. Glinka. The weld profile effect on stress intensity factors in weldments. *International Journal of Fracture*, 35:3-20, 1987.

33. J. D. G. Sumpter. Fracture avoidance in submarines and ships. *Advances in Marine Structures-2*. C. S. Smith, R. S. Dow. Elsevier Applied Sciences, 1991.
34. J.D.G. Sumpter & A. J. Caudrey. Fracture toughness of Steel Plate from MV Kowloon Bridge. *Marine Structures*. Elsevier Science Limited, 6:443-460, 1993.
35. A. Kent Shoemaker. Fracture characteristics of steel under extremely high loading rates. *Extreme Loads Symposium*. SNAME, 1981.
36. J.D.G. Sumpter & A. J. Caudrey. Recommended fracture toughness for ship hull steel and weld. *Marine Structures*. Elsevier Science Limited, 8:345-357, 1995.
37. Takeshi Kanazawa, Susumu Machida, Hiroshi Yajima, Hajime Kawano. Study on brittle crack propagation and arrest behavior in plate and beam structures. *J.S.N.A. Japan*, 149:217-225,1981.
38. Hiroshi Yajima, Hajime Kawano, Yoshio Urabe. Study on brittle crack propagation and arrest behavior in plate and beam structures (Report II). *J.S.N.A. Japan*, 153:170-176, 1983.
39. Minorsky, V. U. An Analysis of Ship Collisions with Reference to Protection of Nuclear Power Plants. *Journal of Ship Research*, 1959, 3, 1.
40. Jones, N. *A Literature survey on the Collision and grounding protection of ships*. SSC-283. Ship Structure Committee, 1979.

-
41. P. R. Van Mater, Jr., and J. G. Giannotti. *Critical Evaluation of Low-Energy ship Collision-Damage Theories and Design Methodologies. Vol I : Evaluation and Recommendation*. SSC-284. Ship Structure Committee, 1979.
42. P. R. Van Mater, Jr., and J. G. Giannotti. *Critical Evaluation of Low-Energy ship Collision-Damage Theories and Design Methodologies. Vol II : Literature Search and Review*. SSC-284. Ship Structure Committee, 1979.
43. J. Poudret, M. Huther, P. Jean, H. Vauhan. Grounding of a membrane tanker; correlation between damage predictions and observations. *Extreme Loads Response Symposium*. SNAME, 1981.
44. Jones N. Plastic Behavior of Ship Structures. *Trans. SNAME*, 84:115-145, 1976.
45. McDermott, J. F., Kline, R. J., Jones, E. L., Maniar, N. M., Chiang, W. P. Tanker Structural Analysis for Minor Collisions. *Trans. SNAME*, 82:382-414, 1974.
46. Wierzbicki, T., Peer, D.B., Rady, E., The Anatomy of Tanker Grounding. *Marine Technology*, 30,2 71-78, 1993.
47. Egge, E. D., Bockenbauer, M. Calculation of the collision resistance of ships and its assessment for classification purposes. *Marine Structures*, 4:35-56. Elsevier Science Publishers, 1991.
48. Preben Terndrup Pedersen. Ship Grounding and Hull-Girder Strength. *Marine Structures*, 7:1-29. Elsevier Science Publishers, 1994.

-
49. Jones, N., On the dynamic inelastic failure of beams. *Structural failure*. Thomasz Wierzbicki, Norman Jones. Wiley, 1988.
50. Duffey, T. A., Dynamic rupture of shells. *Structural failure*. Thomasz Wierzbicki, Norman Jones. Wiley, 1988.
51. Gifford, L. N., Dally, J.W., Dynamic fracture resistance of metal structures loaded into the plastic regime. *Advances in Marine Structures-2*. C. S. Smith, R. S. Dow. Elsevier Applied Sciences, 1991.
52. Dieter Radaj. *Design and Analysis of Fatigue Resistant Welded Structures*. Abington Publishing, 1990.
53. Daniel J. Maykuth, Ed. *Structural Alloys Handbook*. Mechanical Properties Data Center, Battelle Columbus Laboratories, 1980.
54. J. D. Harrison. Application of fracture mechanics in the prevention of service failures. *Criteria For preventing Service Failure in Welded Structures*. The Third International Symposium of the Japan Welding Society, 1978.
55. Kardomateas, G. A. *Mixed mode I and II fully plastic crack growth from simulated weld defects*. PHD thesis, MIT, 1985.
56. McClintock, F. A. *An Analysis of Tearing a Base Plate from the End of a Stiffener*. Project Report 5 on Rupture Analysis of Oil Tankers in Side Collision, MIT, 1997.

57. Masubuchi, K., McClintock, F. A. and Liang, L *Summary Report on Welding Research from the Tanker Grounding Project* TSR 56, , June 1996
58. Private communication with Mitsubishi Heavy Industries, Ltd.
59. Yurioka, N., and Ohkita, S. *Steel Development for Improving Reliability of Welded Steel Structures*, presented at an International Conference on New Horizons in Welding Fabrication, September 26-27, 1996, MIT.
60. Toyota M, *How Steel Structures Fared in Japan's Great Earthquake*, The Welding Journal, Volume 74, No. 12, pp. 31-42, December 1995.
61. Masubuchi, K., *Chapter 5 Fatigue Fracture*, of a Text being developed for Subject 13.15 Materials for Ocean Engineering, MIT.
62. C. R. Jordan, and C. S. Cochran, *In-Service Performance of Structural Details*, Ship Structure Committee Report SSC-272, 1978.
63. C. R. Jordan, and L. T. Knight, *Further Study of In-Service Performance of Structural Details*, Ship Structure Committee Report SSC-294, 1980.
64. C. R. Jordan, and R. P. Krumpfen, *Performance of Ship Structural Details*, The Welding Journal, Volume 63, No. 1, pp. 18-28, January 1984.
65. Sampos, A. G. *Fracture of Fillet Welds under Extreme Loading*, Naval Engineer Thesis, the Departments Ocean Engineering, MIT, 1996.
66. Wilcox, Robb, *The effect of Weld Penetration on the Tensile Strength of Fillet Welded Joints*, TSR 50, the Departments Ocean Engineering, MIT, 1995.

67. McClintock, F. A., *Fully Plastic Mechanics for Welded T-Joints*, TSR 26, MIT, 1994.
68. Kirkov, K. *Tearing Resistance for Fillet Welds in Ships Exposed to Grounding-A Full-Scale Test and Cost Implications*, TSR 29, MIT, 1994.
69. Middaugh, Regina, *A knowledge-Based Expert System for Analyzing Welded Structures*, TSR 43, MIT, 1995.
70. Atmadja, Juliana, *Weld Failures in Oil Tankers Due to Groundings-Finite Element Approach*, thesis of ocean engineer, MIT, 1995

Appendices

Appendix-1 Literature Survey

Overview

In this project, we have mainly studied the fracture of fillet welded stiffer-plate structure under large load so that the plastic failure becomes main issue. The topics include the tearing work of the side fillet weld, the undercut effect at the toe of the end fillet welds, the very low cycle fatigue problems of the fillet welded structures. We did the literature survey roughly covers this topics. Some of the main literature publications are attached in this appendix.

1 Tearing work of the side fillet weld

App-1-a

H. A. McDonald, *Required Strength and tearing Resistance for Fillet Welds in Ship Exposed to Grounding or Collision Loads*, MS Thesis, Dept. of Ocean Engineering, MIT May 1993.

App-1-b

Frank A. McClintock *Fully Plastic Mechanics of Welded T-joints*, TSR report 26 Joint MIT-Industry Project on Tanker Safety, 1994.

App-1-c

Min Du Chang, K. L. Devries, M. L. Williams. *The effects of plasticity in adhesive fracture*, *Journal of Adhesion*. pp 221-231 1972.

App-1-d

A Needle,an, V, TV erGAARD *A Numerical Study of Void Distribution Effects on Dynamic, Ductile Crack Growth*, *Engineering Fracture Mechanics*, Vol38 pp157-173, 1991.

2 Undercut effect

App-1-e

Yukito Hagawara Evaluation of brittle fracture strength from the surface notch at fillet weld toe based on CTOD criterion. JSNA Japan, 157:pp223-232, 1985.

App-1-f

Masakazu Onozuka, Osamu, Ushirokawa, Yasushi Kumakura *The Influence of Bead Toe Shapes on the Fatigue Strength of Fillet Welded Joints - Fabrication Acceptance Criteria for undercut Depth*, JSNA Japan, vol 170, December 1991.

3. Very Low Cycle Fatigue

App-1-g

Dziubinski J. , Adamiec P., Brunne W. A Welded joint microstructure effect on low-cycle fatigue. *Low Cycle Fatigue and Elastoplastic Behavior of Materials*. K.-T.Rie. Elsevier Applied Science, 1987.

App-1-h

K. Shimada, J. Komotori, M. Shimizu. Fracture mode transition and damage in extremely low cycle fatigue. *Low Cycle Fatigue and Elastoplastic Behavior of Materials*. K.-T.Rie. Elsevier Applied Science, 1987.

App-1-i

Havas I., Czoboly E.. Effect of low-cycle fatigue on the brittle characteristics of a structural steel. *Low Cycle Fatigue and Elastoplastic Behavior of Materials*. K.-T.Rie. Elsevier Applied Science, 1987.

App-1-j

B. N. Leis. A nonlinear history-dependent damage model for low cycle fatigue. *Low Cycle Fatigue*. ASTM STP 942. H. T. Solomon, G.R. Halford, L. R. Kaisand, B. N. Leis. American Society for Testing and Materials, 1988.

App-1-k

Kunihiro Iida. Very low cycle fatigue life influenced by tensile or compressive prestrain. *Low Cycle Fatigue*. ASTM STP 942. H. T. Solomon, G.R. Halford, L. R. Kaisand, B. N. Leis. American Society for Testing and Materials, 1988.

App-1-l

T. Kunio, M. Shimizu, N. Ohtani, T. Abe. Microstructural aspects of crack initiation and propagation in extremely low cycle fatigue. *Low Cycle Fatigue*. ASTM STP 942. H. T. Solomon, G.R. Halford, L. R. Kaisand, B. N. Leis. American Society for Testing and Materials, 1988.

App-1-m

T. Nakatsuji, T. Fujimori. A study on engineering critical assessment of weld defects in steel building constructions-Behavior of welded joints including weld defects under ultra-low cyclic large strain deformations. *Criteria For preventing Service Failure in Welded Structures*. The Third International Symposium of the Japan Welding Society, 1978.

Appendix-2 Experiment Descriptions

Overview

In this project, a series of tests were performed on the fillet weldment. The tests were performed on the Baldwin testing machine with the largest capacity of 60,000lbs. Detail calibration table can be found in appendix -3 equipment descriptions. The Microscope video, Hirox Hi-scope compact Micro Vision System, Model KH2200, was extensively used to monitor record history of crack formation and propagation of the interested area during the tests. Also, it was applied in the post failure analyses after the three point bending tests. The detail information of the Video Microscope can be found in Appendix -2 - HIROX-Hi-Scope Video Microscope.

1 HIROX-Hi-Scope Video Microscope

The Hi-Scope KH-2200 Video Microscope System is a combination of the long history of microscopy and the recent advances in CCD camera technology. The fusion of these optical fields allows the user to easily inspect minute details in ways not possible with conventional microscopes or visual inspection equipment.

The main control unit is the light source and controls the camera functions. The camera unit holds the camera and accepts interchangeable lenses. The lenses allow the user to change magnifications. The lenses accept adapters that vary the working distance, lighting style, and viewing angle. The main unit is connected to the camera via a fiber optic lighting cable and a camera cable. The main control unit also connects to a video monitor to display the image, and to other video devices for storage and manipulation. The versatility of the lenses and adapters that could be used enables the video microscope to be applicable and various fields such as:

- Dermatology
- Consumer goods
- Pharmaceuticals
- Biology
- Police Departments
- Metallurgy

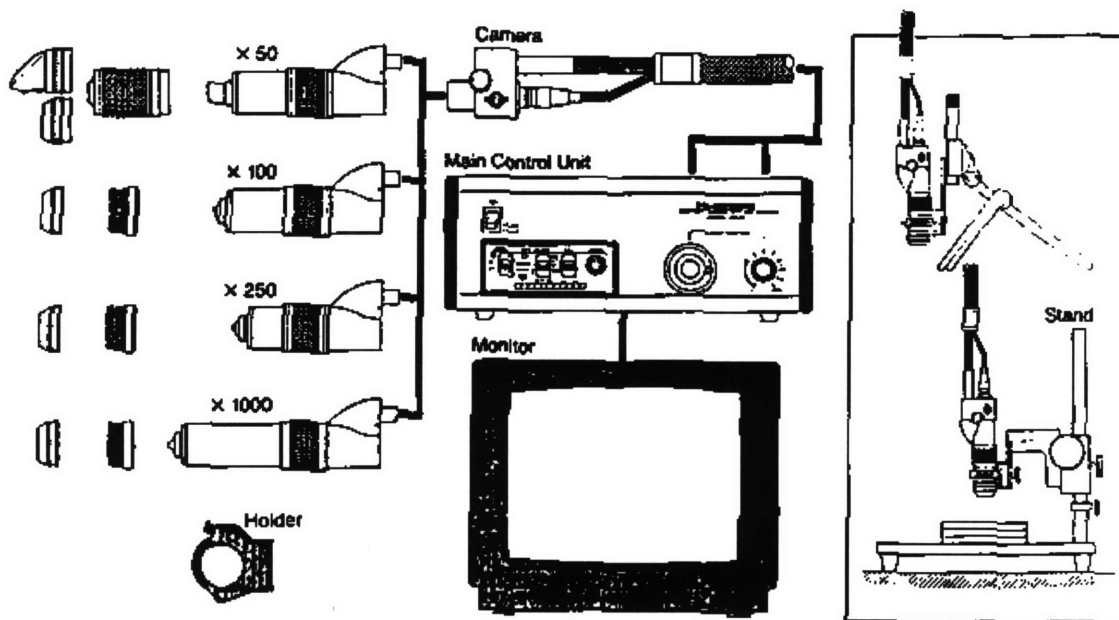
- Mechanical Engineering
- Electrical Engineering
- Chemical Engineering

Especially in Metallurgy which is the application of our interest, the videoscope may give images of surface details comparable to those of a scanning electron microscope. Also it can be used to view metal with nearly perfect vertical lighting, thus doing the job as a metal microscope performing "bright field" imaging.

The main advantages of the video microscope are:

- **Hand-held.** With the Hi-Scopethe sample can be kept where it is, while the optical head is moved to the whole sample. Hi-Scope requires no slicing, polishing, or other processing preparation before viewing the sample.
- **Video System.** Hi-Scope is a video system and the image can be observed on a video monitor. This means the image can be easily saved, printed, or analyzed with suitable processing systems.
- **Continuously Variable Lighting Angle.** According to the application used the lighting angle can be changed for optimum results.
- **Great Depth of Field.** Hi-Scope's depth of field is 10 to 20 times that of a binocular microscope which allows almost a three dimensional viewing.

- **Wide Range of Lenses.** With the Hi-Scope System there is a choice of magnification lenses from less than true size to 1600x. There is also a zoom lens with continuous focus of 20 to 100x.
- **Wide Range of Adapters.** Various adapters are offered to fit the needs of any application.
- **Automatic Lighting Control.** The System features automatic lighting control to ensure optimum lighting instantly.



Video-microscope general set-up.

2. Baldwin TEG Univ. Machine Calibration table

American Calibration & Testing Co., Inc.
 176 Walnut Street
 Lawrence, MA 01841

TESTING MACHINE CALIBRATION REPORT AND DATA

OWNER		Machine Reading lb.	Verification Reading lb.	Machine Error		V.D. Code
				lb.	%	
Name	Mass. Inst. of Technology	600	602.1	-2.1	0.35	1 & 2
Location	Bldg. #1 Room 034	1,000	1,002.7	-2.7	0.27	"
	77 Mass. Ave.	2,000	2,005.0	-5.0	0.25	"
	Cambridge, MA. 02138	3,000	3,006.7	-6.7	0.22	1 & 3
MACHINE		4,000	4,010.1	-10.1	0.25	"
Manufacturer	Baldwin	5,000	5,012.1	-12.1	0.24	"
Type	Model TEG Univ. Machine	6,000	6,014.8	-14.8	0.25	"
Capacity	0-6,000, 0-24,000 & 0-60,000 lbs.					
Serial No.	040-1089	2,400	2,395.9	4.1	0.17	1 & 2
CALIBRATION APPARATUS DATA		4,000	3,993.1	6.9	0.17	1 & 3
Type of Apparatus Used	DJ Instr./Coti Calibration System	8,000	7,981.6	18.4	0.23	"
Manufacturer	DJ Instr./Coti, Inc.	12,000	11,984.1	15.9	0.13	"
Apparatus Verified & Directly Traceable to the NIST, Washington, D.C.		16,000	16,007.1	-7.1	0.04	"
Apparatus Verified in Accordance With ASTM Specification E74		20,000	20,011.9	-11.9	0.06	"
VERIFICATION DEVICE		24,000	24,023.8	-23.8	0.1	"
V.D. Code	Serial No.	Loading Range	Verif. Date Lab. No.			
1	43051	Cal. Ind.	8-14-95 SJT,01/106172	6,000	5,989	11 0.18 1 & 3
2	3330	32 - 600 lbs.	"	10,000	9,982	18 0.18 "
3	5009	1,951 - 25,000	9-28-94 SJT,01/105948	20,000	19,966	34 0.17 "
4	5072	19,960 - 240,000 lbs.	"	30,000	29,949	51 0.17 1 & 4
5				40,000	39,911	89 0.22 "
6				50,000	49,882	118 0.24 "
Compensated Loads Corrected For Temp. of 23° C				58,000	57,854	146 0.25 "

Service Engineer **DATE**
 G. W. Mooney July 12, 1995

A.S.T.M. Spec. E4 Calibration Frequency: 1 Year

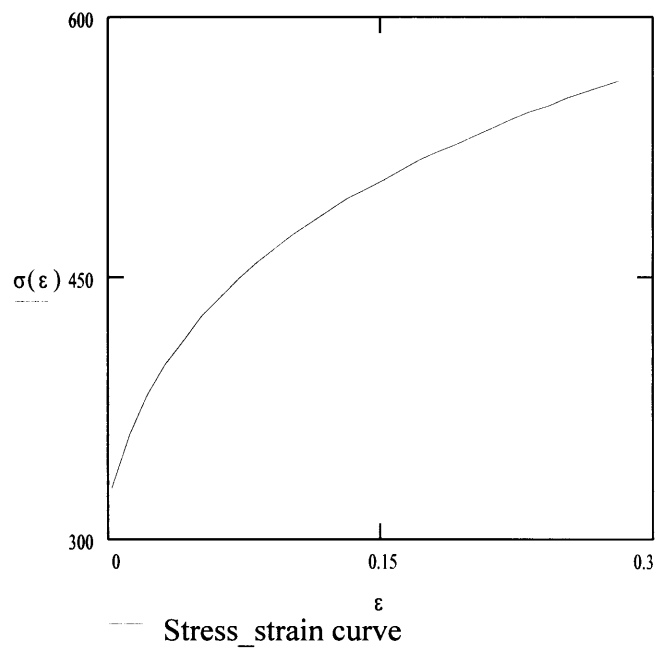
Appendix 3 Calculation (computer programs, etc.)

1. Power law material simulation

$$\epsilon := 0.002, 0.012 \dots 0.29$$

$$\sigma(\epsilon) := 705.54 \cdot (\epsilon + 0.014)^{0.184} \quad \epsilon_{pl}(\epsilon) := \epsilon - \frac{\sigma(\epsilon)}{210000}$$

ϵ	$\sigma(\epsilon)$	$\epsilon_{pl}(\epsilon)$
0.002	329.67	$4.301 \cdot 10^{-4}$
0.012	360.476	0.01
0.022	382.72	0.02
0.032	400.377	0.03
0.042	415.134	0.04
0.052	427.876	0.05
0.062	439.128	0.06
0.072	449.231	0.07
0.082	458.416	0.08
0.092	466.851	0.09
0.102	474.659	0.1
0.112	481.937	0.11
0.122	488.757	0.12
0.132	495.179	0.13
0.142	501.253	0.14
0.152	507.016	0.15
0.162	512.502	0.16
0.172	517.74	0.17
0.182	522.753	0.18
0.192	527.562	0.189
0.202	532.183	0.199
0.212	536.633	0.209
0.222	540.925	0.219
0.232	545.072	0.229
0.242	549.083	0.239
0.252	552.968	0.249
0.262	556.735	0.259
0.272	560.393	0.269
0.282	563.948	0.279



2. Matla program for v_{pe} and v_{pec}

```

clf
  K=0.:0.0001:0.25;
  m=length(K);
  v= 2.371341743*K.^1.4;
  %axes('position',[0.1 0.2 .5 .5]);
  plot(K,v);
  hold on
  i=(0:m-1)/10000;
  vc=0.133*i./i;
  plot(i,vc);
  grid on
  xlabel('K*(t/2)');
  ylabel('vpe/(t/2)');

```

3. Maple program for deduction of the equations

```
restart;
```

```
>
>
>
```

```
> Vpe:=Cvpe*K^(1+2*n)/(((tw+2*d)/w)^2*((1-(tw+2*d)/w))^(1/n));
```

$$Vpe := \frac{Cvpe K^{(1+2n)} w^2}{(tw+2d)^2 \left| 1 - \frac{tw+2d}{w} \right|^{1/n}}$$

```
> Cvpe:=CLpe/((a/n+2)*((1+n/2)*CMpe)^(2+1/n));
```

$$Cvpe := \frac{CLpe}{(a/n+2) \left((1+1/2n) CMpe \right)^{(2+1/n)}}$$

```
> CMpe:=(1+2*n)/(1+n)*(Cb/CLpe^n+Ce*Clpe);
```

```
> CLpe:=(n*Cb/Ce)^(1/(1+n));
```

```
>
```

$$CMpe := \frac{\sqrt{(1 + 2n) \sqrt{Cb} + Ce \sqrt{CLpe}}}{1 + n}$$

$$CLpe := \frac{\sqrt{1 + n} \sqrt{Cb}}{Ce}$$

```
>
> Cb:=((a/n+1)^(n+1))/((1+n)*(1+n/2)*(a/n+a+1));
```

$$Cb := \frac{(1 + n) (a/n + 1)}{(1 + n) (1 + 1/2 n) (a/n + a + 1)}$$

```
>
>
> Ce:=(1.5*n^n*e^(-n))/(a/n+2);
```

$$Ce := 1.5 \frac{n^{-n} e^n}{a/n + 2}$$

```
>
>
> n:=0.2;tw:=38;t:=19;w:=127;a:=0.3;e:=2.718;d:=9.5;
```

n := .2

tw := 38

t := 19

w := 127

a := .3

e := 2.718

d := 9.5

>

>

> **Ce:=1.5*n^n*e^(-n)/(a/n+2);**

Ce := .2543193023

> **Cb:=(a/n+1)^(1+n)/(1+n)/(1+1/2*n)/(a/n+a+1);**

Cb := .8124488868

> **CLpe := (n*Cb/Ce)^(1/(1+n));**

CLpe := .6884497823

```
> CMpe := (1+2*n)/(1+n)*(Cb/(CLpe^n)+Ce*CLpe);
```

```
CMpe := 1.225602479
```

```
> vpe:=Cvpe*K^(1+2*n)/(tw+2*d)^2*w^2/((1-(tw+2*d)/w)^(1/n));  
>
```

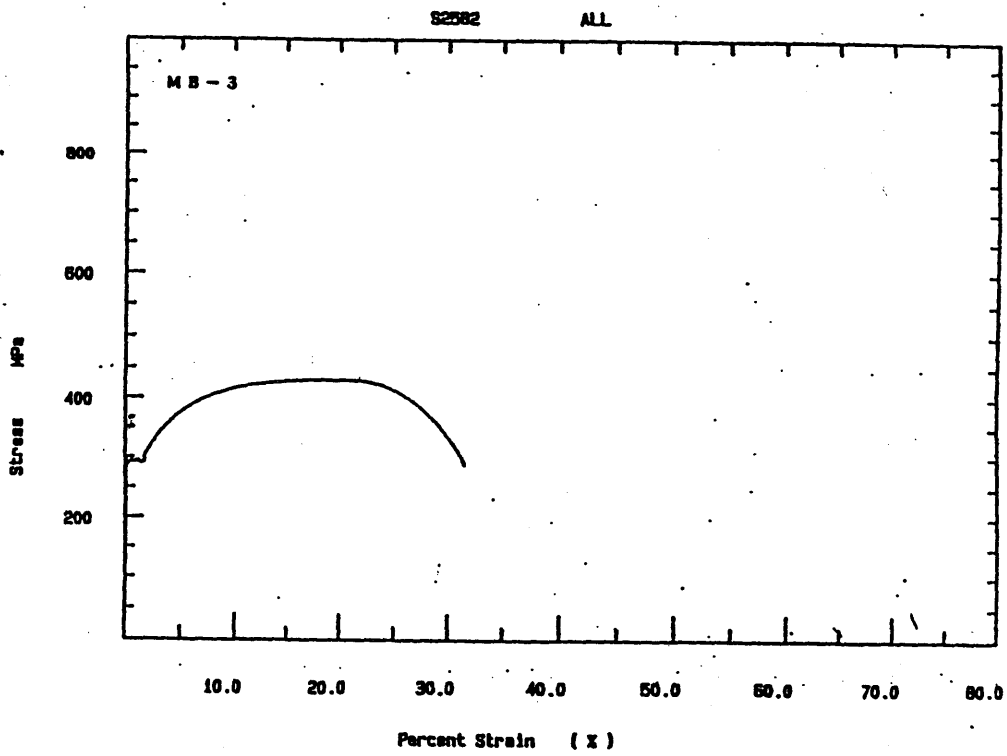
```
1.4  
vpe := 2.371341743 K
```

```
> plot(vpe,K=0..0.25);
```

```
>
```

Appendix -4 Experiment Data

1. Uniaxial tension test data of EH36 steel obtained from Kawasaki Heavy Industries



Page 1

圖 引張試驗結果 (応力-歪曲線)

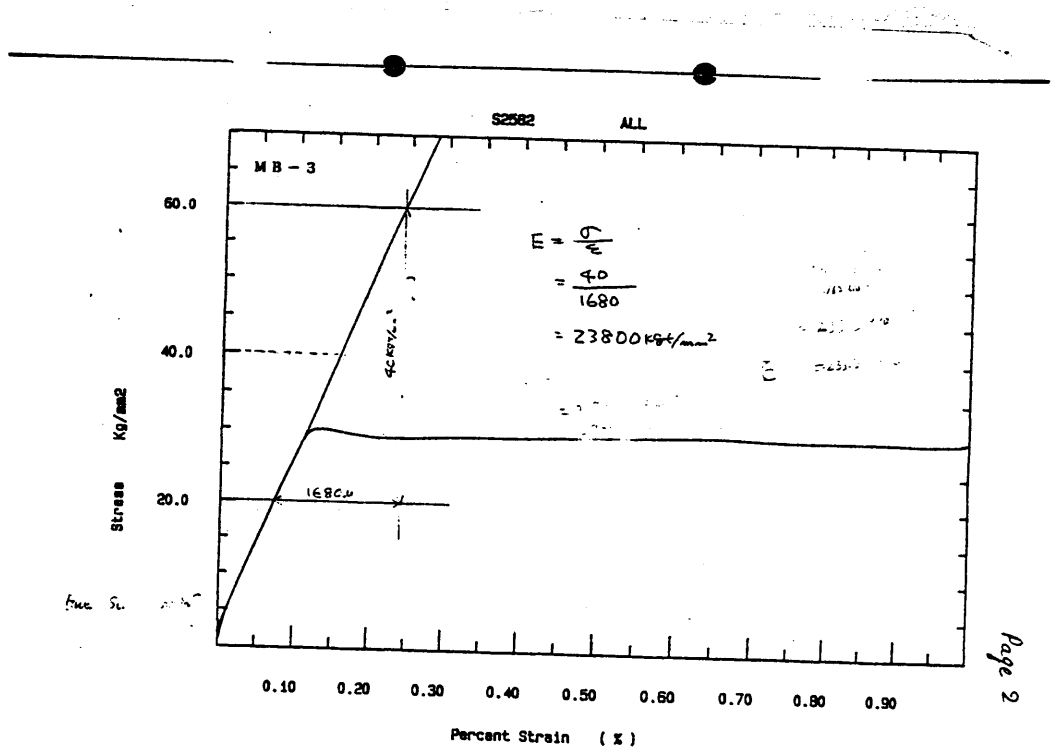


圖 引張試驗結果(応力-変曲線)

2 Load and displacement record

Specimen 1

LOAD (LBS)	DISPLACEMENT (MILS)
0	0
189	2320
255	3200
323	3460
408	3720
429	4000
538	4200
667	4400
782	4520
1001	4600
1211	4700
1345	4800
1513	4820
1846	4700
1907	4700

Specimen 2

FIRST CYCLE

LOAD (LBS)	DISPLACEMENT (MILS)
0	0
1980	90
2800	129
3300	167
3580	219
3800	290
4180	452
4460	585
4700	679
4900	855
5060	995
5190	1052

SECOND CYCLE

LOAD (LBS)	DISPLACEMENT (MILS)
0	0
1600	180
2920	316
4400	525
4840	658
5300	850
5500	1085
5380	1385
5360	1685
4620	1753
4240	1855
4020	1905

Specimen 3**FIRST CYCLE**

LOAD (LBS)	DISPLACEMENT (MILS)
0	0
1220	75
2600	126
3400	181
3740	248
4000	327
4240	433
4560	578
4800	698
4940	803
5100	950
5200	1143
5240	1352

SECOND CYCLE

LOAD (LBS)	DISPLACEMENT (MILS)
0	0
2080	120
3840	258
4720	420
5140	616
5380	853
5360	1155
4440	1258
4250	1340
3960	1440
3700	1588

Specimen 4**FIRST CYCLE**

LOAD (LBS)	DISPLACEMENT (MILS)
0	0
1420	78
3000	143
3900	218
4360	320
4660	433
5040	575
5180	660
5440	880
5600	1175
5640	1225

SECOND CYCLE

LOAD (LBS)	DISPLACEMENT (MILS)
0	0
1600	85
3640	202
4740	370
5240	567
5500	750
5760	935

THIRD CYCLE

LOAD (LBS)	DISPLACEMENT (MILS)
0	0
1980	125
3400	212
4480	350
4960	473
5320	690
5620	1038

Specimen 5**FIRST CYCLE**

LOAD (LBS)	DISPLACEMENT (MILS)
0	0
1000	144
1980	185
2910	237
3300	276
3650	340
3990	446
4235	543
4510	678
4750	860
4900	1045
5000	1189
4945	1267
4910	1376
4900	1499
4875	1614

SECOND CYCLE

LOAD (LBS)	DISPLACEMENT (MILS)
0	0
270	89
1230	128
2440	185
3450	258
4380	399
4780	545
5080	832
5125	1020
5070	1206
4925	1336
4850	1415
4650	1565

Specimen 6**FIRST CYCLE**

LOAD (LBS)	DISPLACEMENT (MILS)
0	0
1035	147
2130	187
3250	259
3825	369
4255	519
4740	803
4950	1022
5060	1210
5100	1439
5000	1743
4850	1886
4720	2008

SECOND CYCLE

LOAD (LBS)	DISPLACEMENT (MILS)
0	27
1160	128
2255	175
3520	253
4650	394
5150	581
5355	778
5360	1019
5330	1053
5250	1183
5140	1325
4950	1431

Specimen 7

FIRST CYCLE

DISPLACEMENT (mils)	LOAD (lbs)
37	0
48	2000
54.5	3000
60	4000
66	5000
71	6000
76	7000
80.7	8000
85	9000
91.3	10000
95.1	11000
105	13000
126.2	16000
158	19000
187	21020
221	23200
233	24900
350	30000
470	35000

SECOND CYCLE

DISPLACEMENT(mils)	LOAD (lbs)
57	0
190	15000
260.1	22500
290	25000
327	27400
385	30000
470	32450
490	32550

THIRD CYCLE

DISPLACEMENT (mils)	LOAD (lbs)
130	0
148	2000
167	5000
173.2	6000
183	8000
195	10000
208	12000
208	12000
239	14000
257.5	16000
267	18000
278	19000
313	20000
346	25000
388	27500
460	30000
510	30100

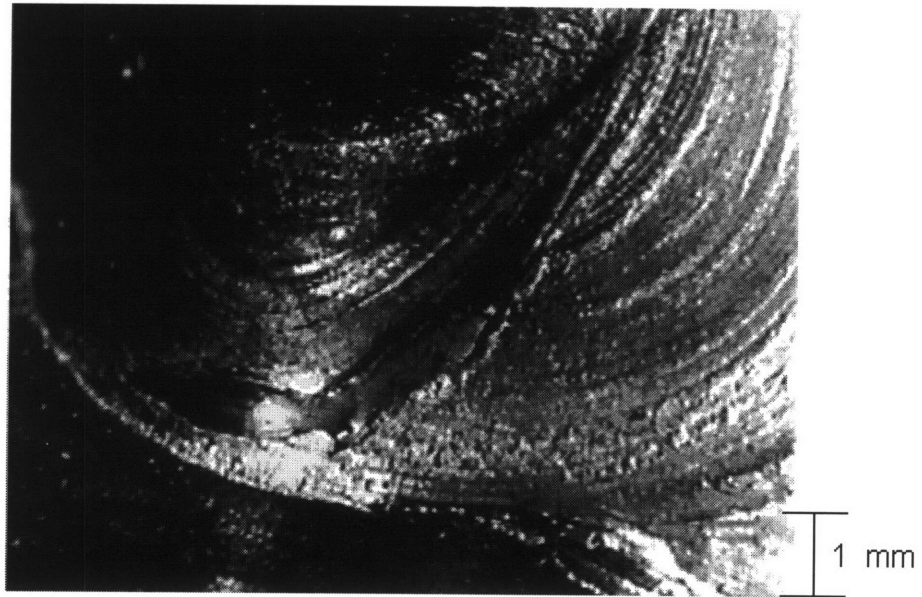
FORTH CYCLE

DISPLACEMENT (mils)	LOAD (lbs)
130	0
148.5	3000
154.5	4000
166.5	6000
170	7000
175	8000
183.5	10000
193	12000
197	13000
209	15000
222	17020
233	19000
248	21000
257	22000
275	24000
285	25000
315	27500
345	30000
380	32400
403	33000
420	35000
470	37500
480	22000

2. Still photos of failure observation

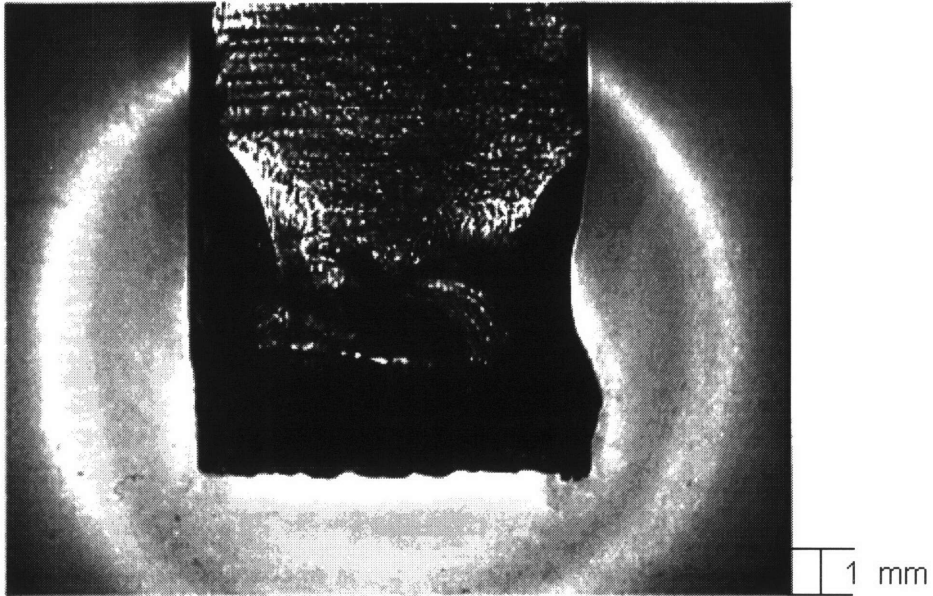
The following picture data were the still photos printed by the Sony Mavigraph color printer. These pictures correspond to the respective loads of each specimen during the tests. Also, the post failure measurements of the cut sections of specimen 2 and specimen 3 are attached in this appendix. The purpose of using this post failure still picture measurement of u_{i+f} is to calculate the values of the tearing work of side fillet weld as the input data. For Specimen 7, strain information could be obtained from the grid marked on the specimen. This information will be used in the calculation.

Specimen 1

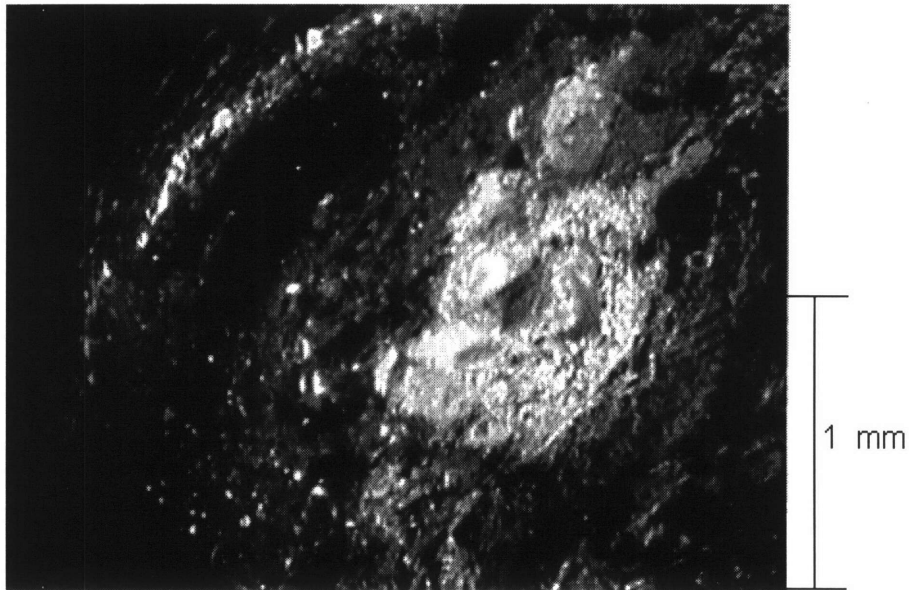


Specimen 1 fractured weld toe.

Specimen 2



General view of specimen 2 weld fractured surface.

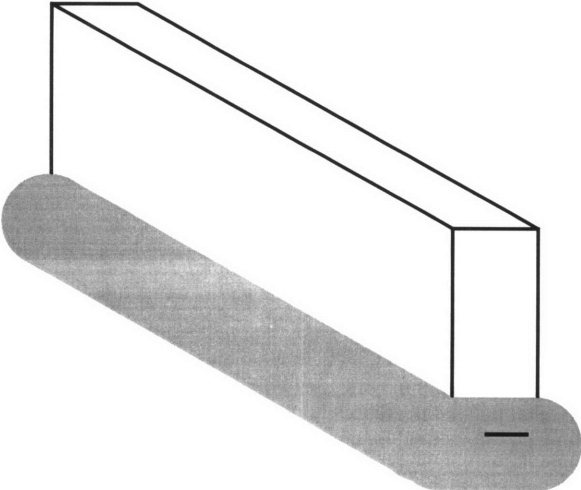


Close view of specimen 2 weld fractured surface

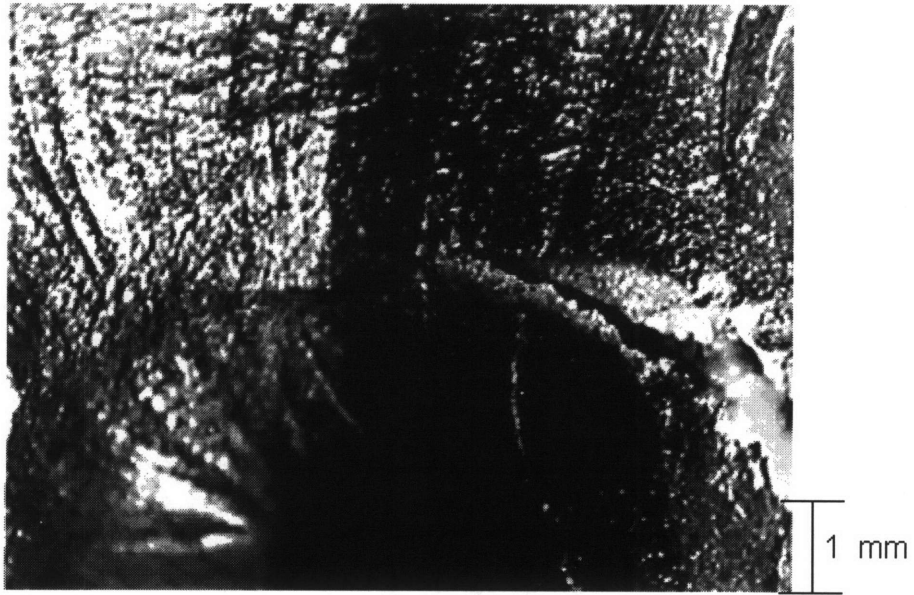
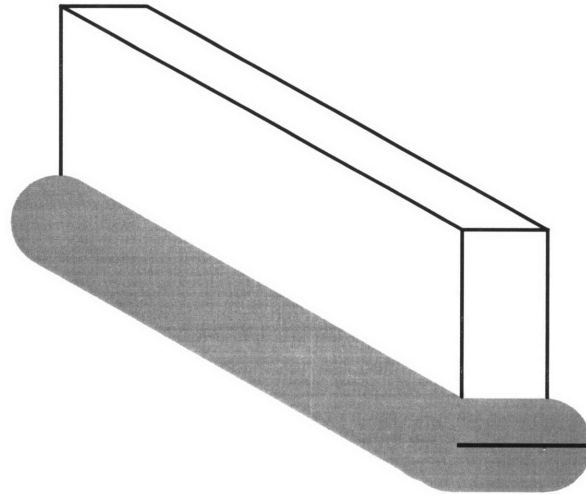
Crack propagation record

Point definition

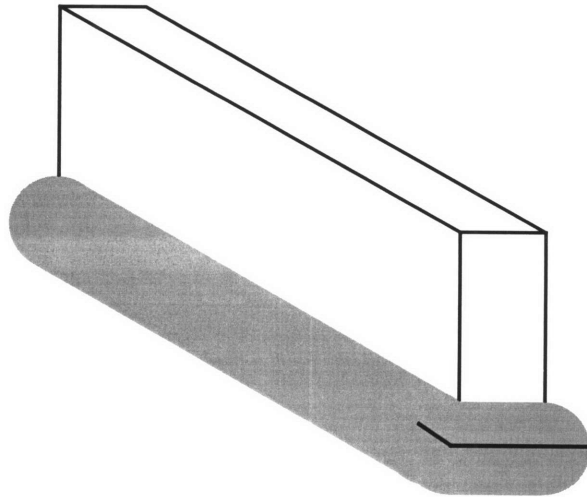
Reference Points	Load (lbs)	Displacement (mils)	Crack length (mm)
B	5380	135	initiation
C	5360	1685	initiation
D	4620	1753	4
E	4240	1855	6.5
F	4020	1905	8.5



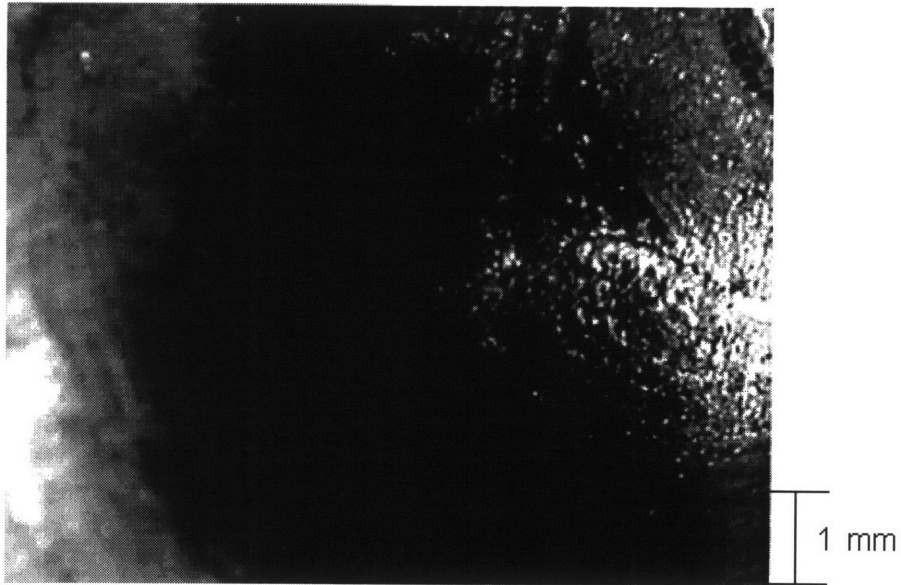
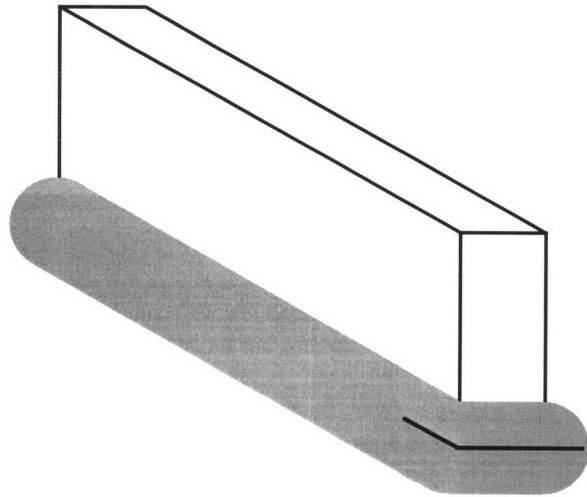
Crack initiation (B)



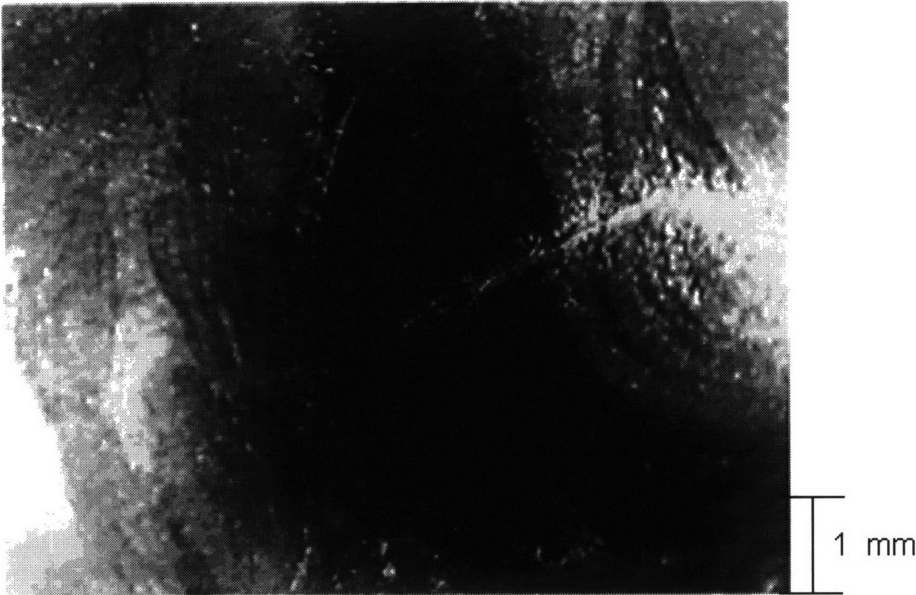
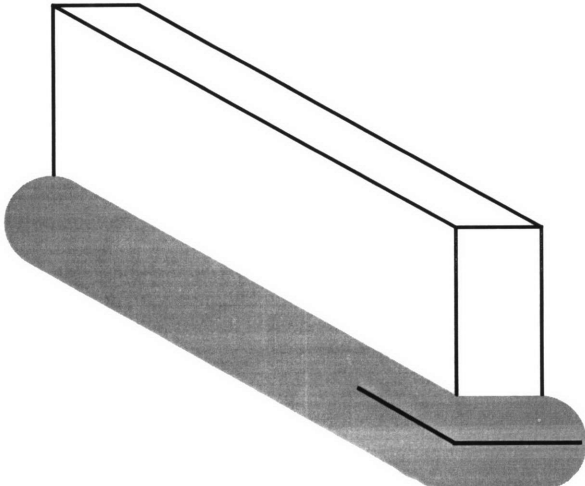
Transverse crack propagation and transition from transverse to longitudinal cracking (C).



Initiation of steady state peeling fracture (D)

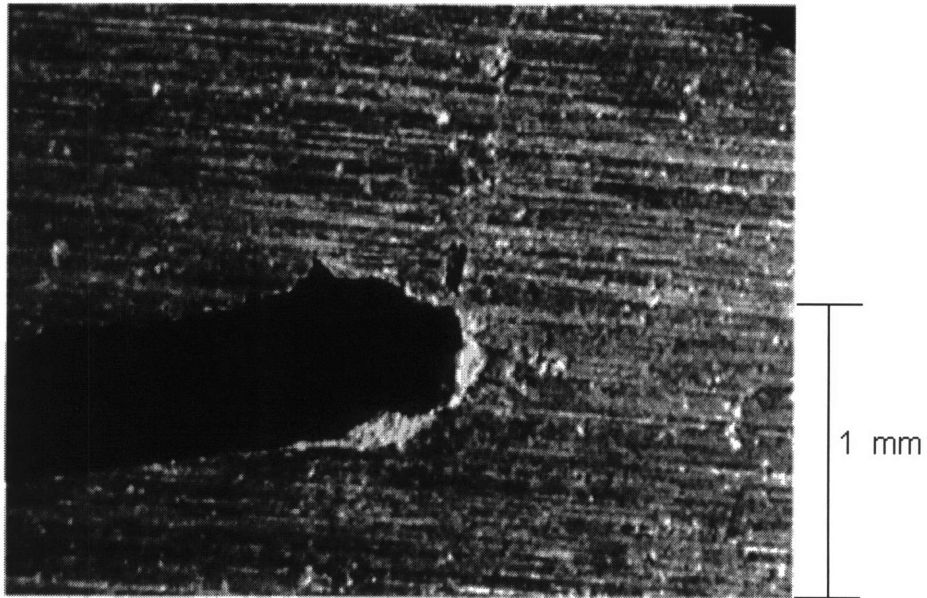


Crack propagation along the weld bead (E)

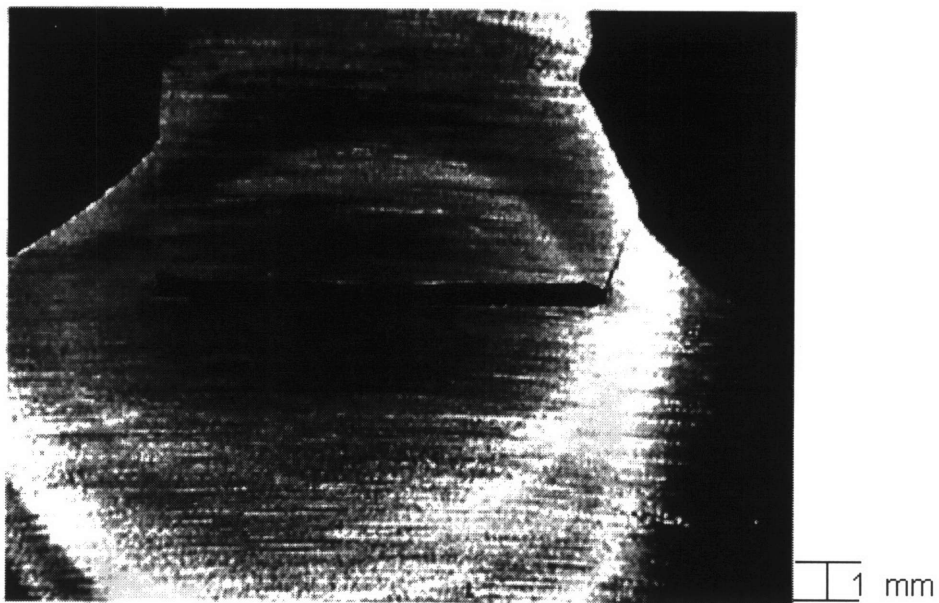


Final stage of crack propagation (F)

After test cut section u_{i+f} measurement



Displacement of the web from the base plate for specimen 2.



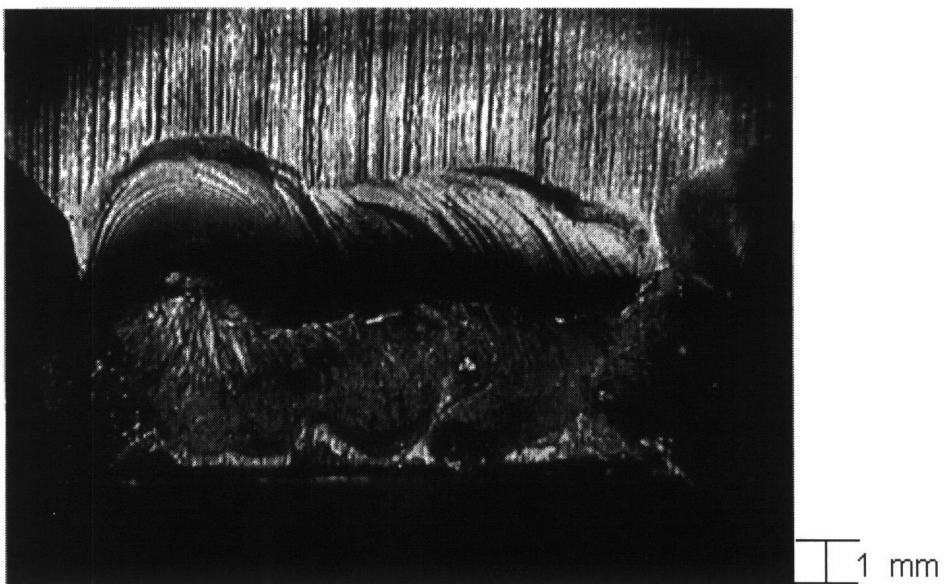
Specimen 2 cross sectional view of the fillet weld after fracture

Specimen 3

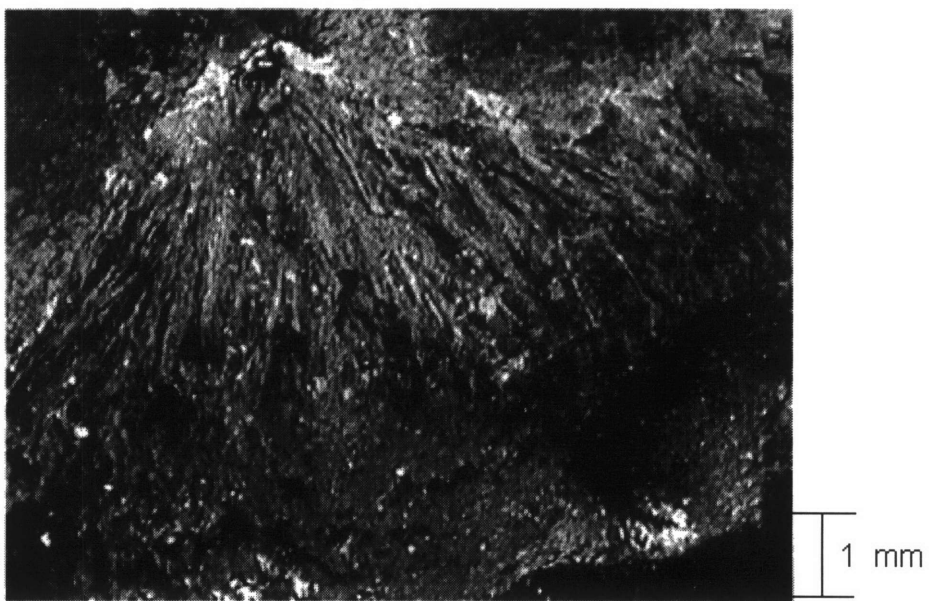
Crack propagation record

Point definition

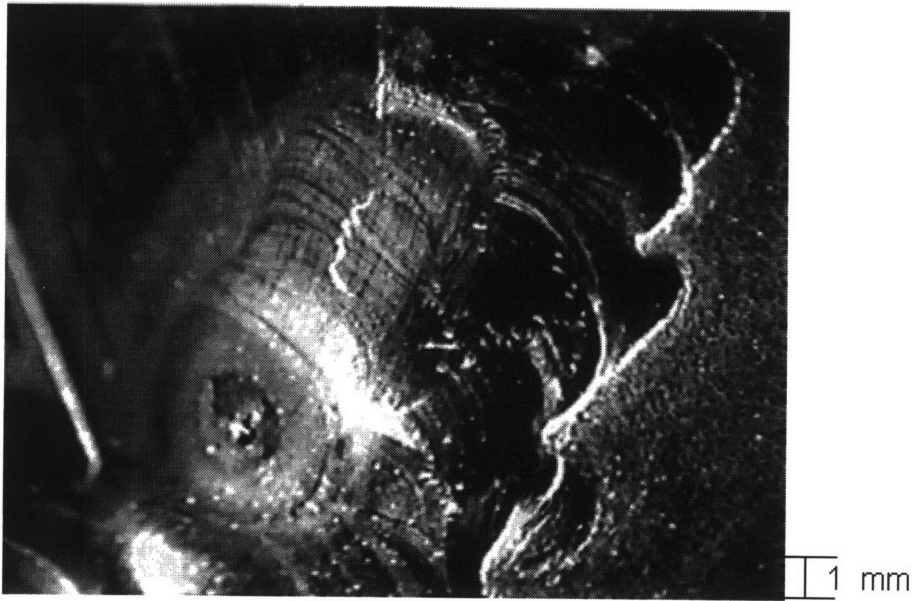
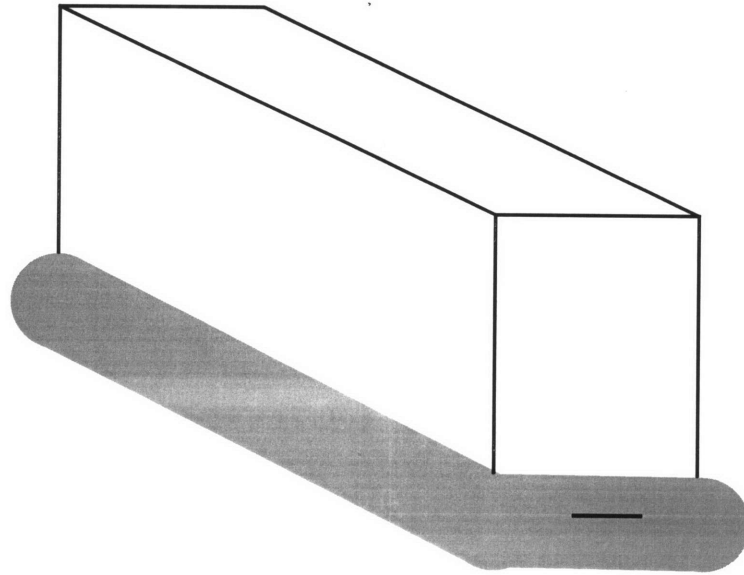
Reference Points	Load (lbs)	Displacement (mils)	Crack length (mm)
B	5380	853	initiation
C	5360	1155	initiation
D	4440	1258	2
E	4360	1340	4
F	3860	1440	10.5
G	3700	1588	12.5



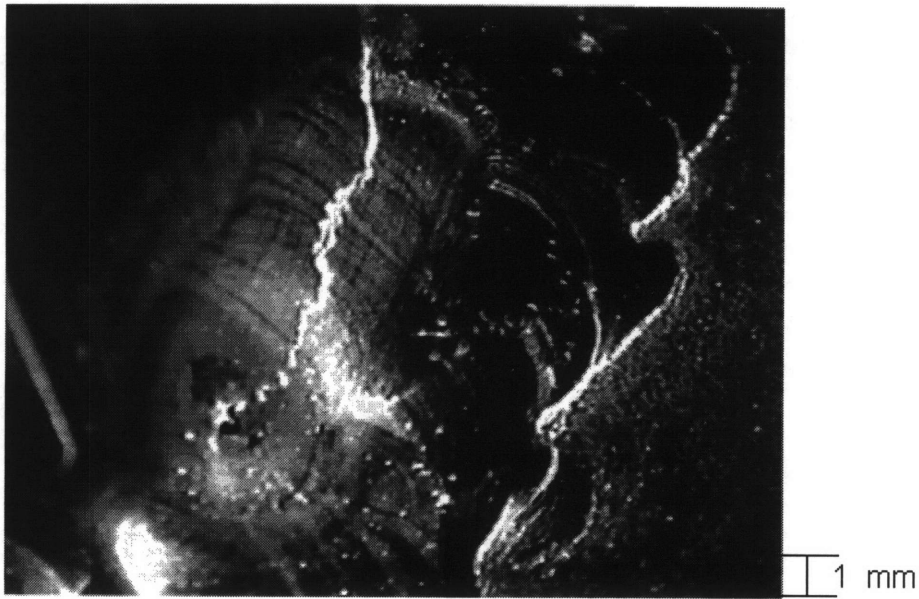
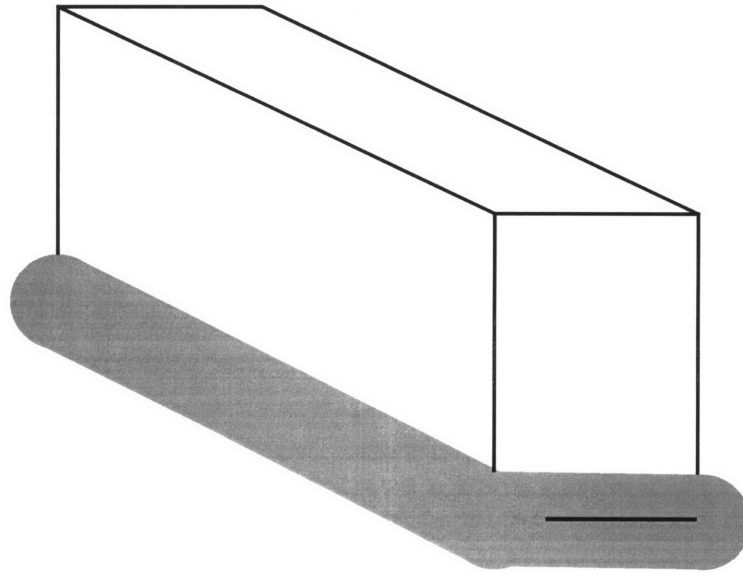
General view of specimen 3 weld fractured surface.



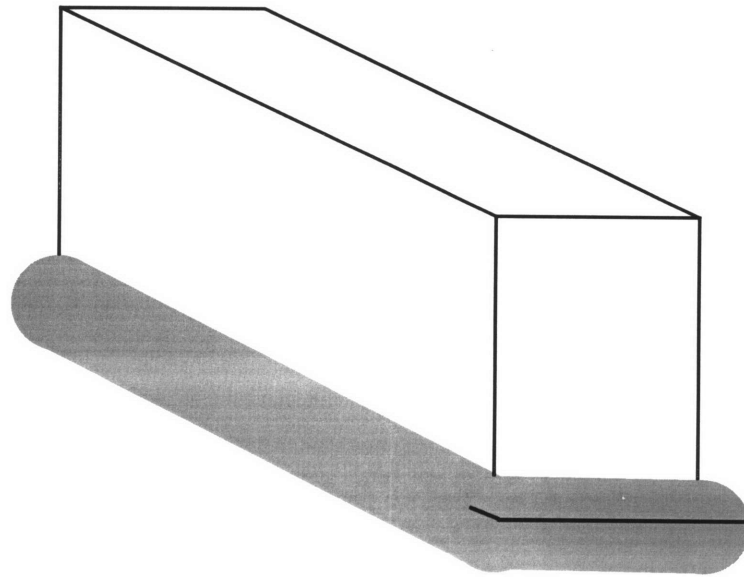
Close view of specimen 3 weld fractured surface.



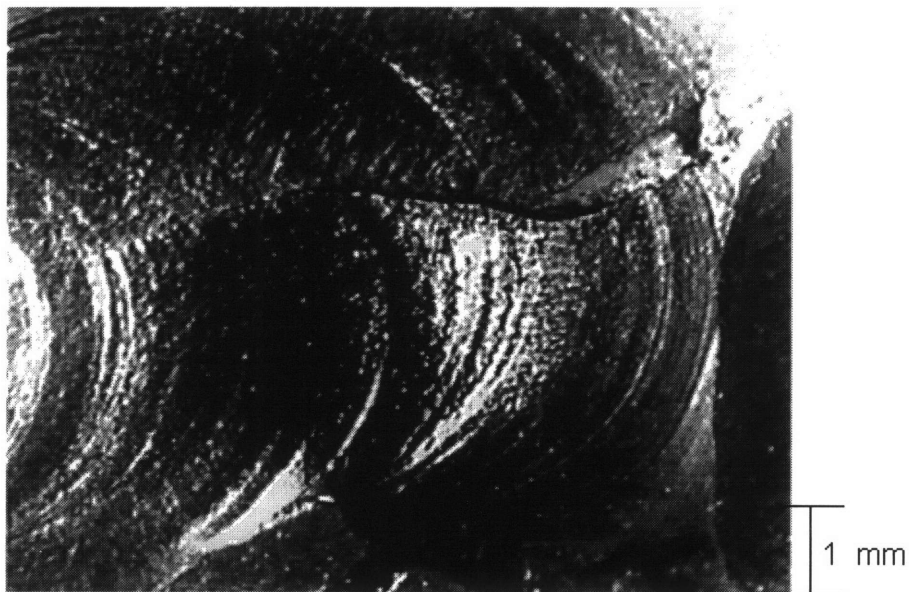
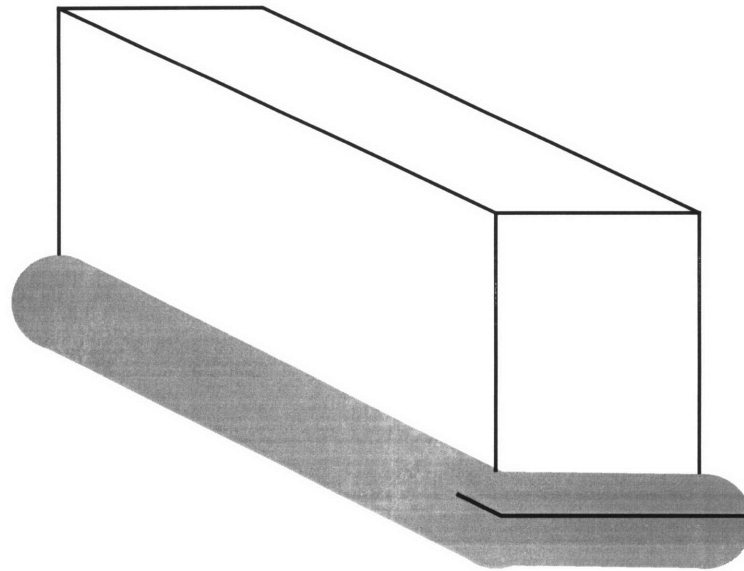
Crack initiation (B)



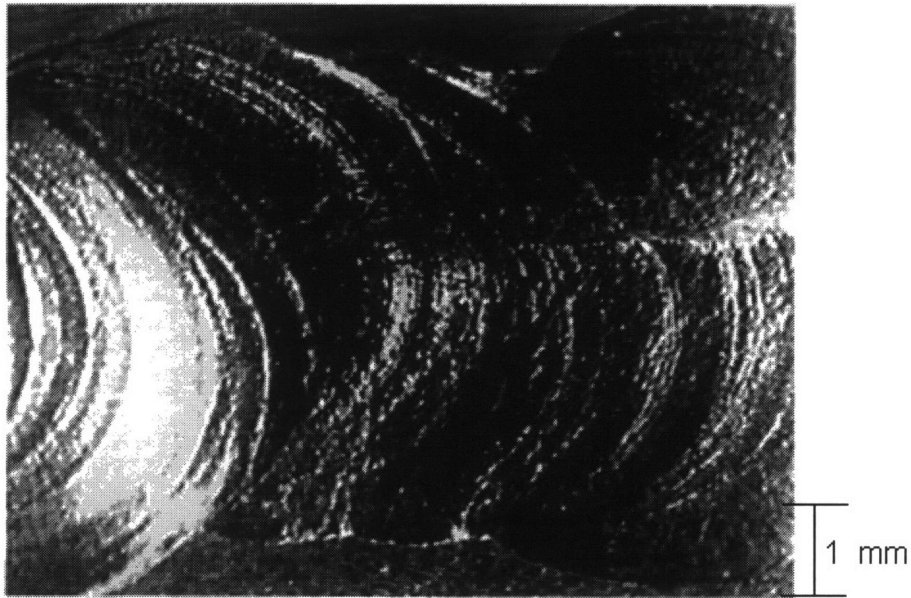
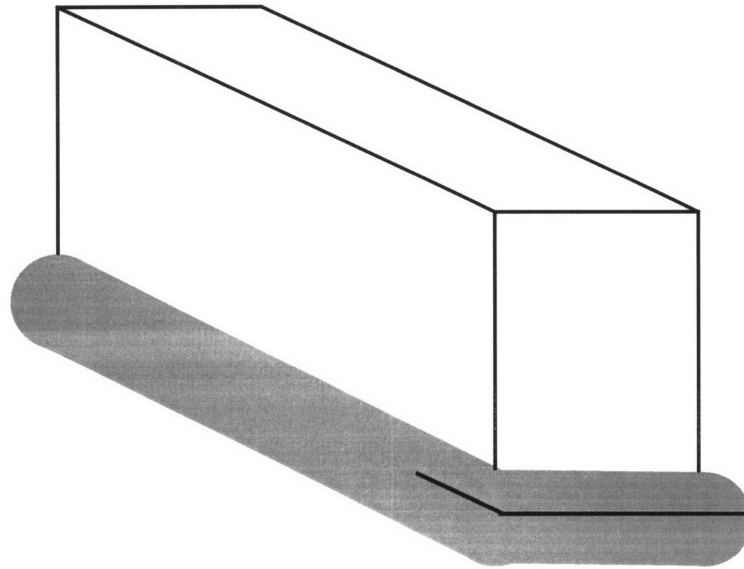
Crack propagation along the width of the weld (C).



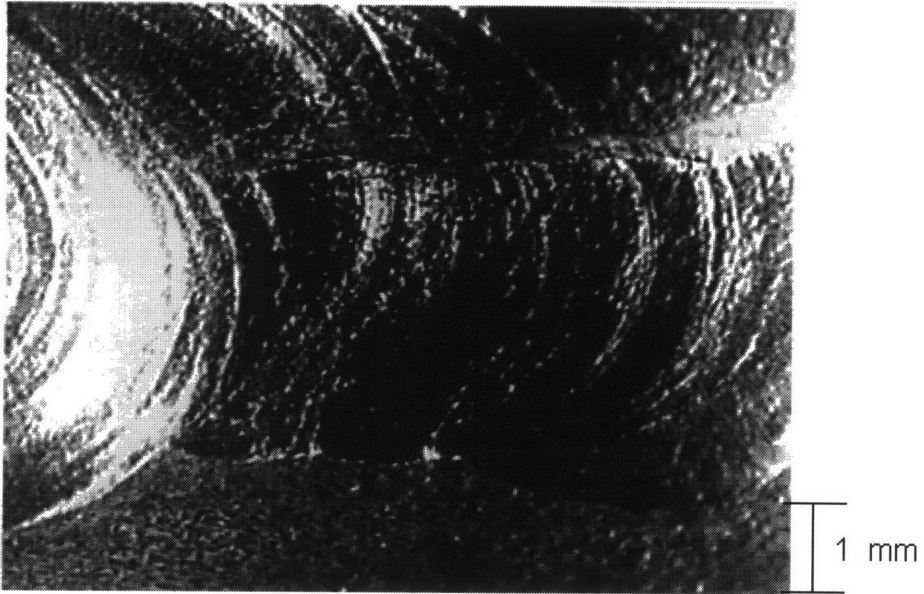
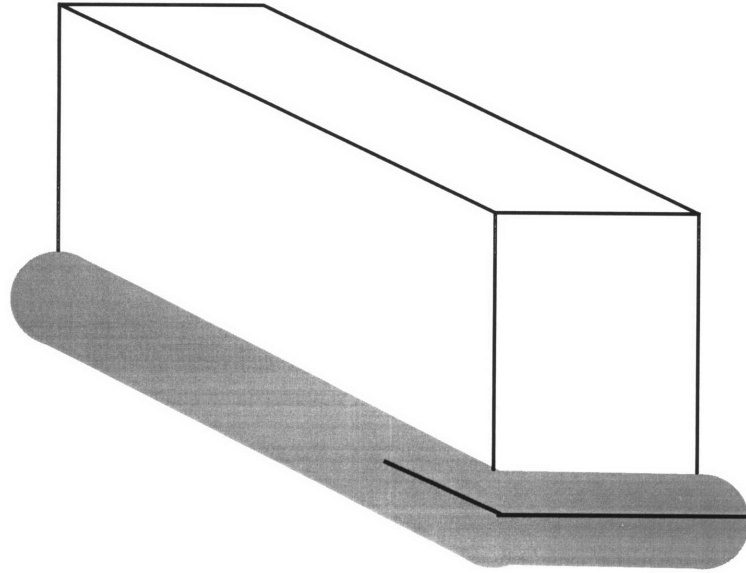
Steady state peeling fracture initiation (D)



Peeling fracture of the fillet weld (E).

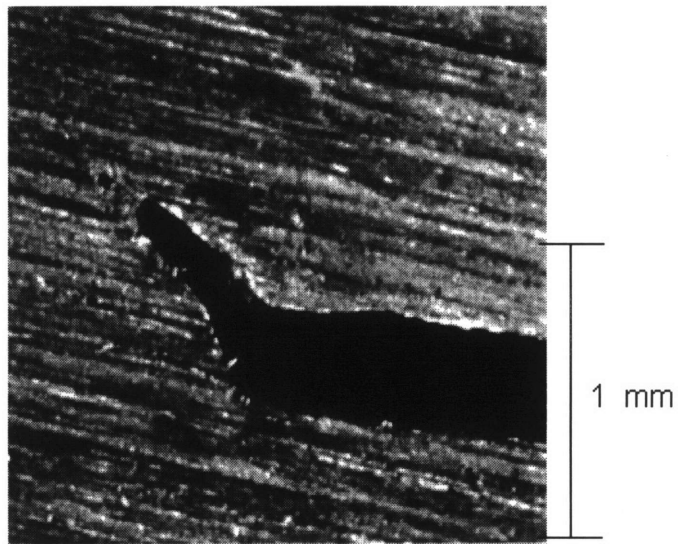


Peeling fracture of the fillet weld (F).

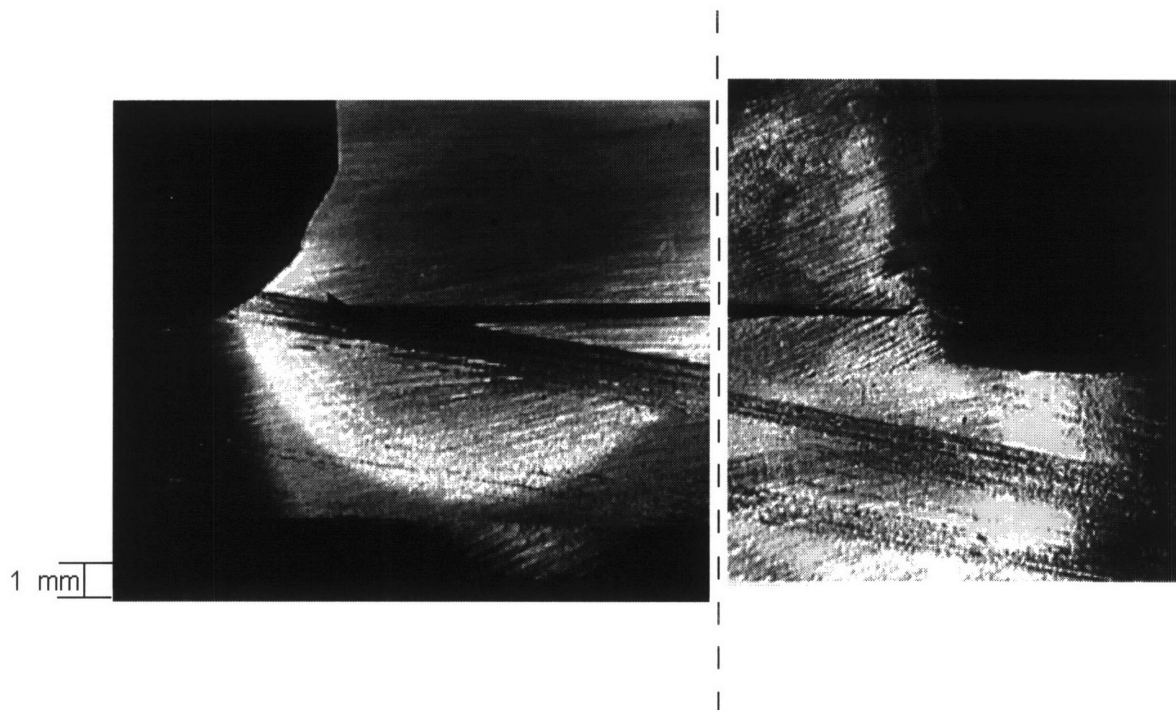


Final point of longitudinal weld tearing (G).

After test cut section u_{i+f} measurement



Displacement of the web from the base plate for specimen 3.

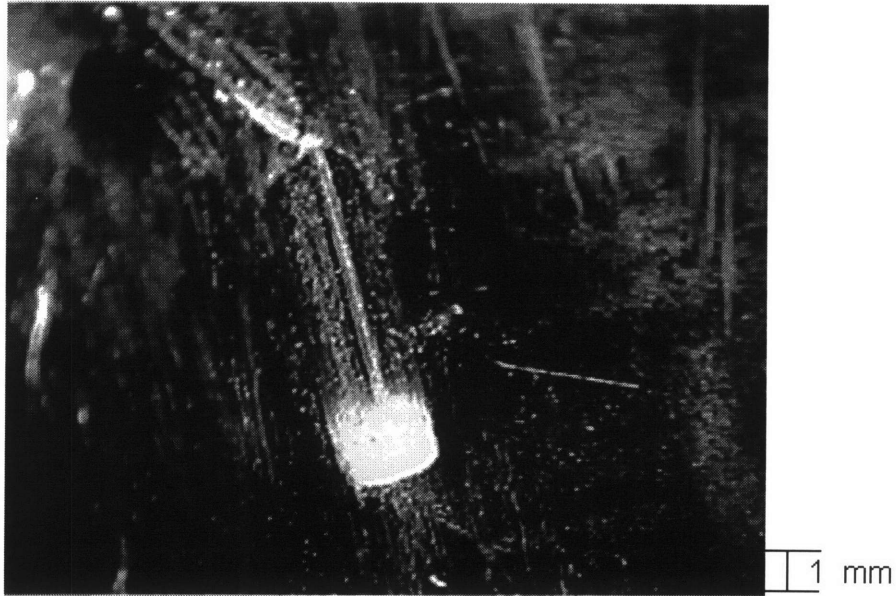


Specimen 3 cross sectional view of the fillet weld after fracture.

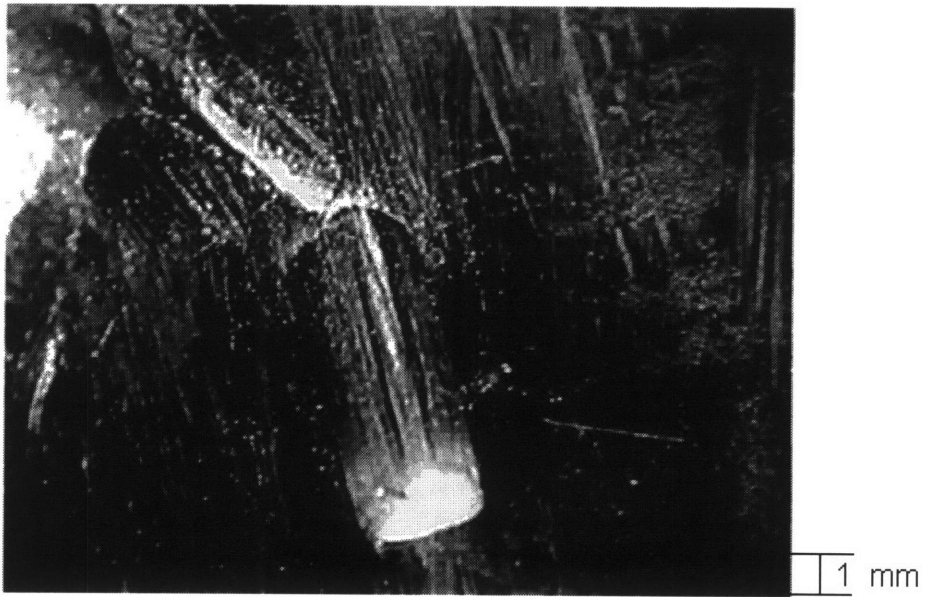
Specimen 5

Reference point definition

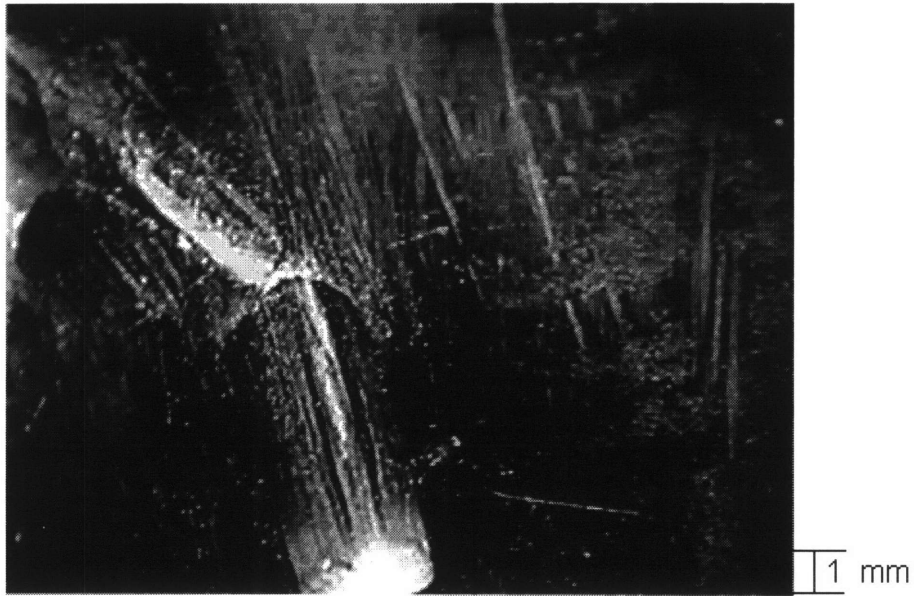
Reference Point	Load (lbs)	Displacement (mils)
A1	4235	543
B1	4750	860
C1	4875	1614
A2	4380	399
B2	5080	832
C2	5125	1020
D2	4925	1336



Crack initiation at the tip of the notch (A1).



Crack appearance at point B1.



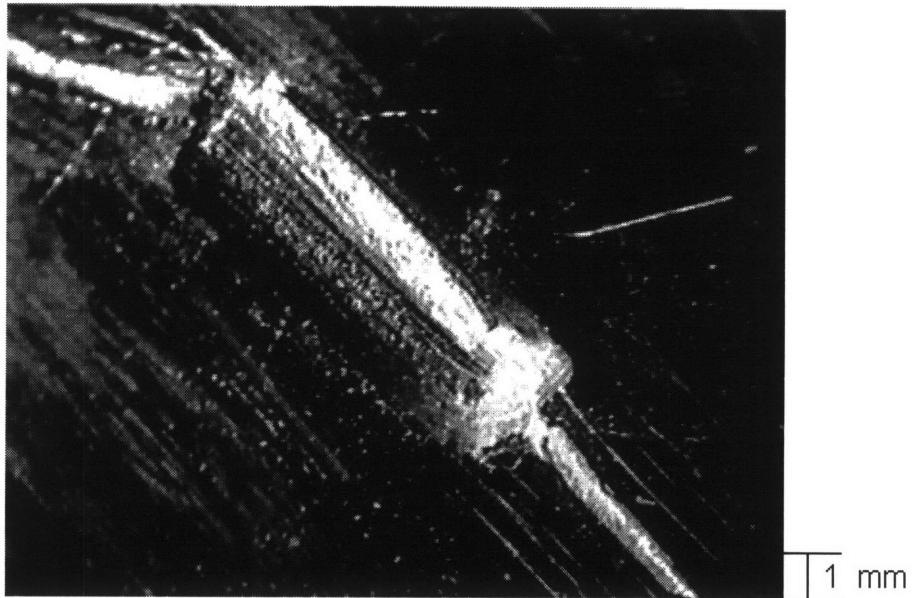
Crack appearance at point (C1).



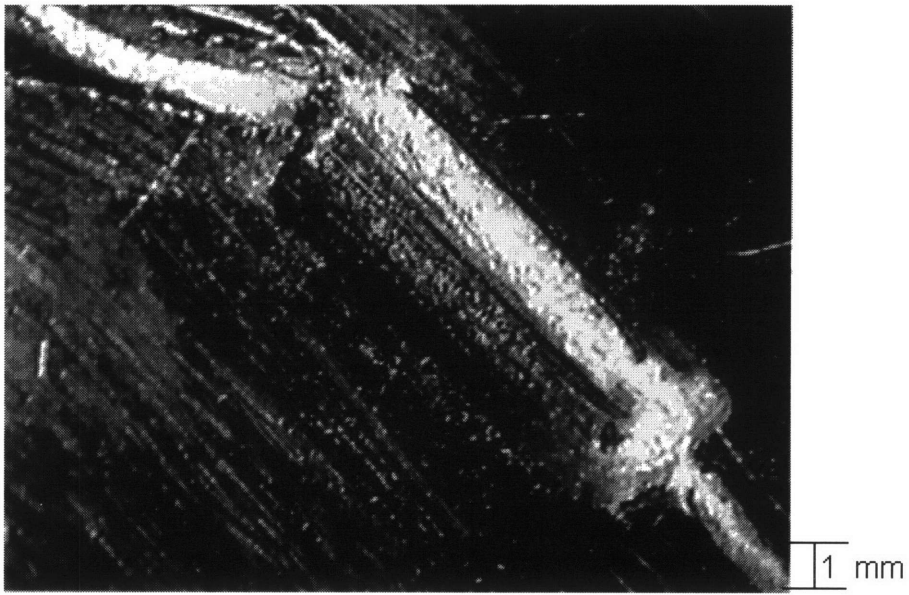
Crack initiation at the low end of the notch at the surface of the base plate (A2).



Crack appearance at point (B2).



Crack appearance at point (C2).

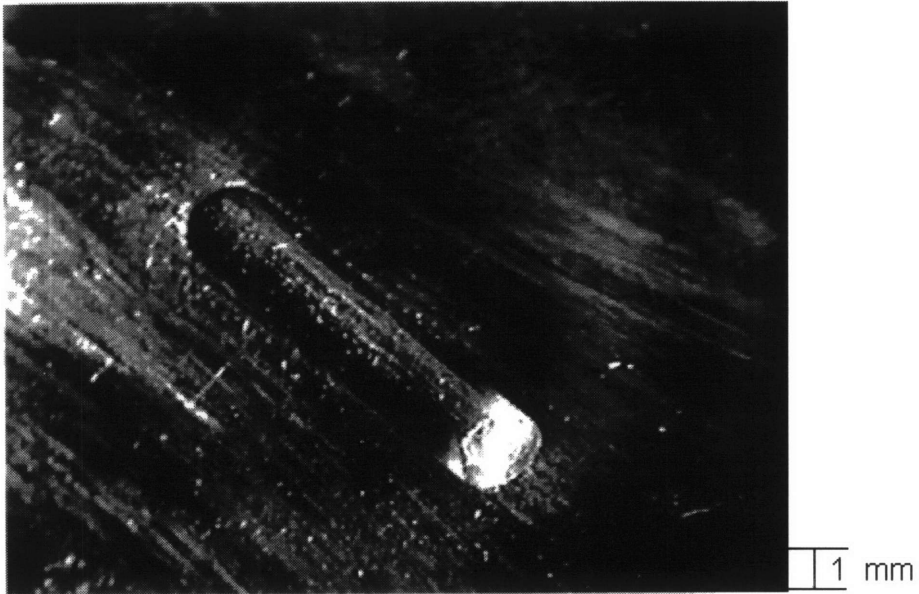


Crack appearance at point (D2).

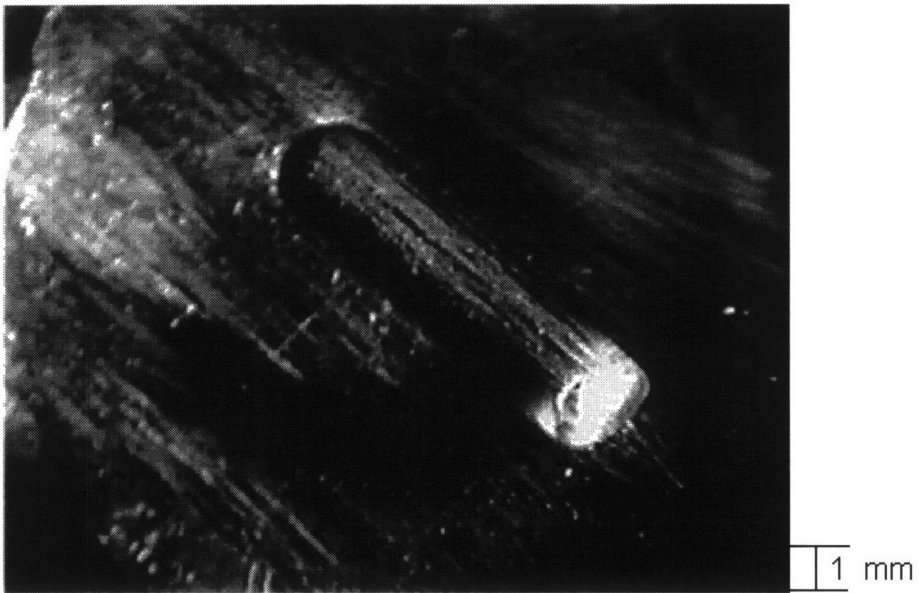
Specimen 6

Reference point definition

Reference Points	Load (lbs)	Displacement (mils)
A1	4740	803
B1	5060	1210
C1	5000	1743
A2	4650	394
B2	5150	581
C2	5360	1019
D2	5140	1325

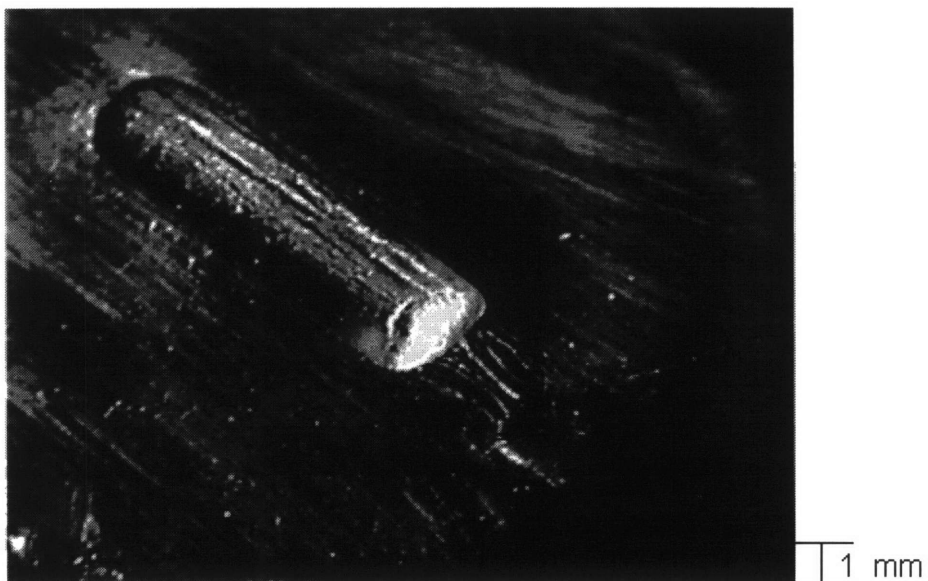


Crack initiation (A1).

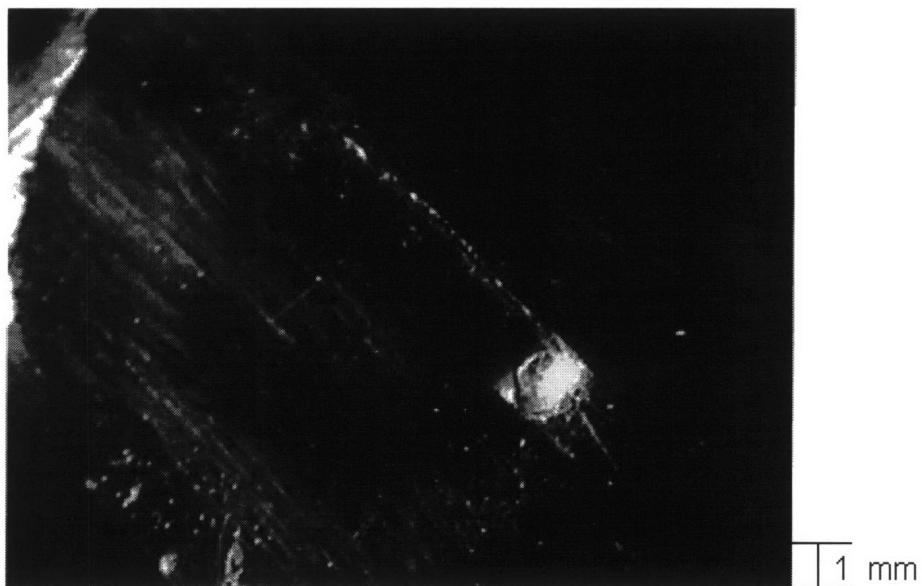


Multiple cracking in the notch and crack initiation at the notch end at the plate surface

(B1).



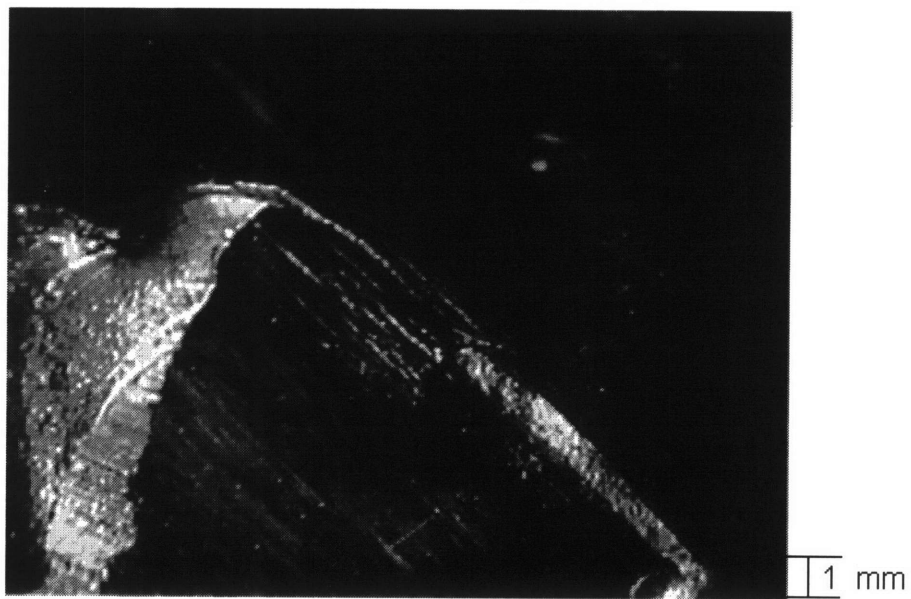
Multiple cracking at the final stage of the first loading cycle (C1).



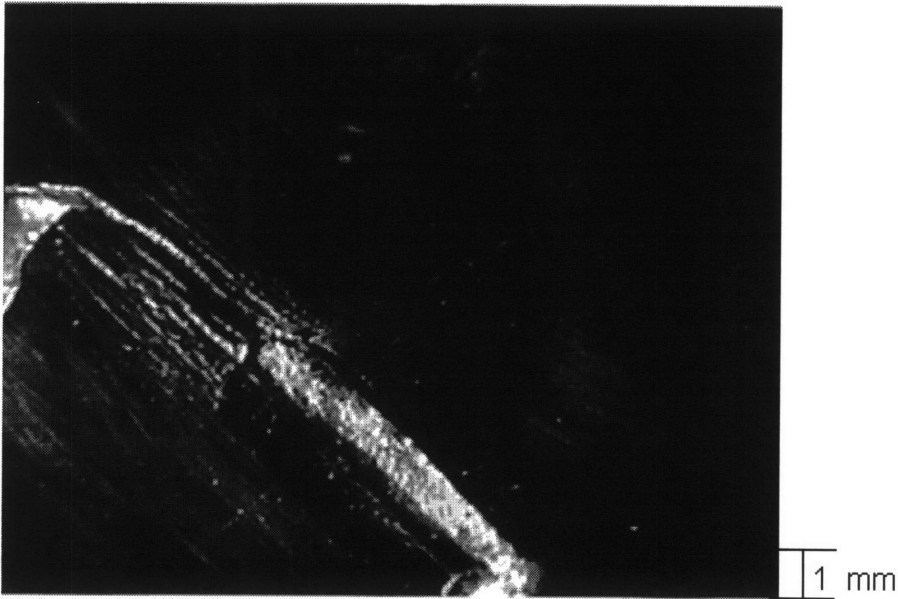
Single cracking appearance at the second cycle (A2)



Crack appearance at point (B2).



Crack appearance at point (C2).



Crack appearance at point (D2).

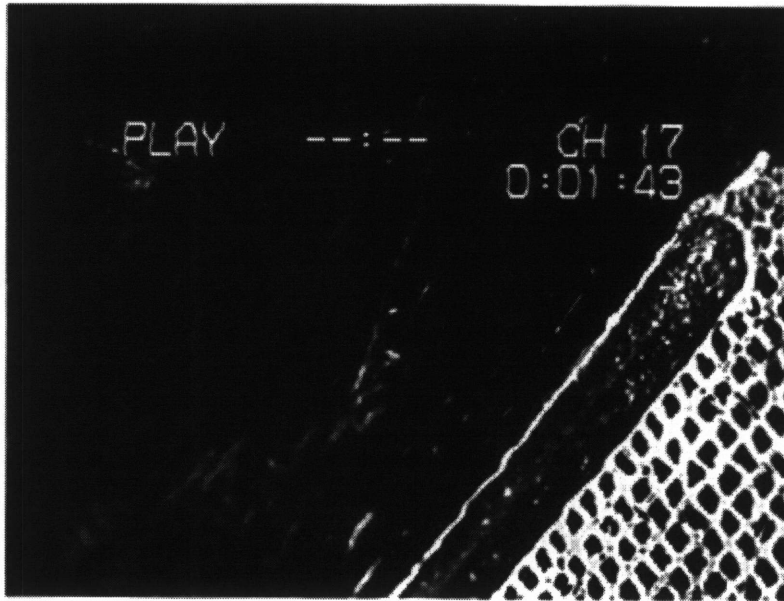
Specimen 7

Reference point definition

Reference Points	Loads (lbs)	Displacement (mils)
A1	0	37
B1	3000	54.5
C1	8000	80.7
D1	9000	85
E1	13000	105
F1	19000	158
G1	25000	233
H1	30000	350
I1	35000	470
A2	15000	190
B2	22500	260.1
C2	25000	290
D2	27400	327
E2	30000	385
F2	32450	470
G2	32550	490
A3	2000	148
B3	5000	167

C3	8000	183
D3	10000	195
E3	14000	239
F3	18000	267
G3	20000	313
H3	25000	388
I3	30000	460
J3	30100	510
A4	3000	148.5
B4	6000	166.5
C4	10000	183.5
D4	13000	197
E4	19000	233
F4	21000	248
G4	25000	285
H4	27500	315
I4	30000	345
J4	33000	403
K4	35000	420
L4	37500	470
M4	20000	480

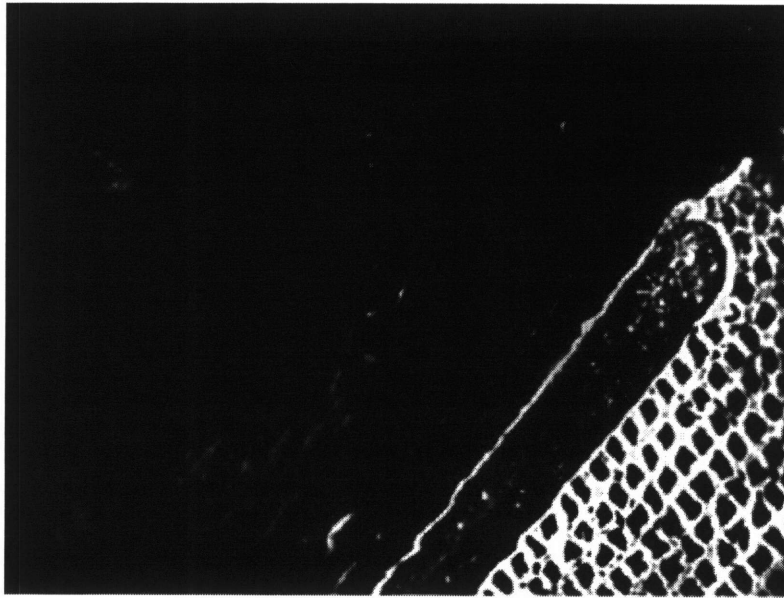
First cycle Load



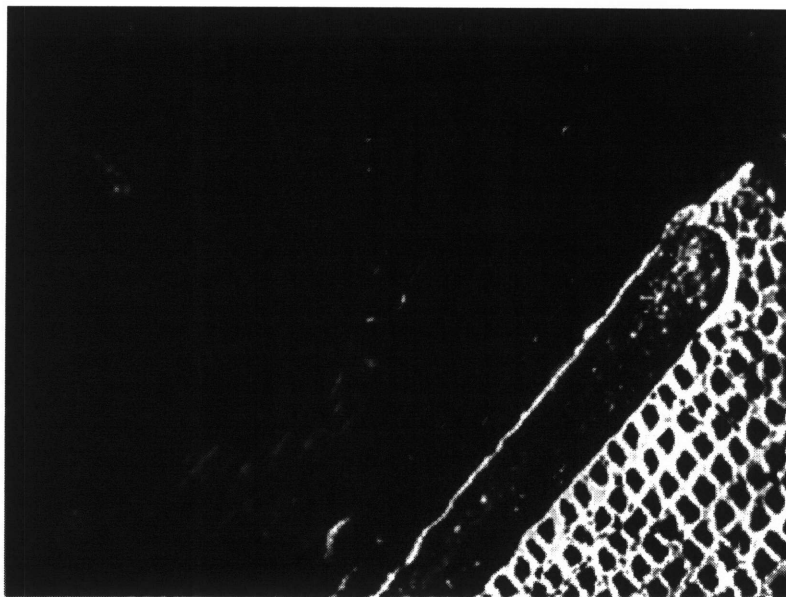
Point A1



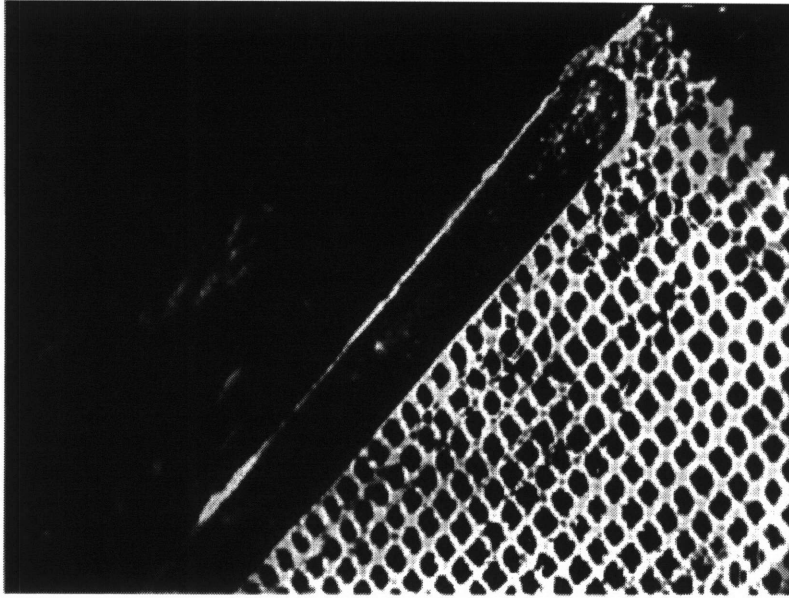
Point B1



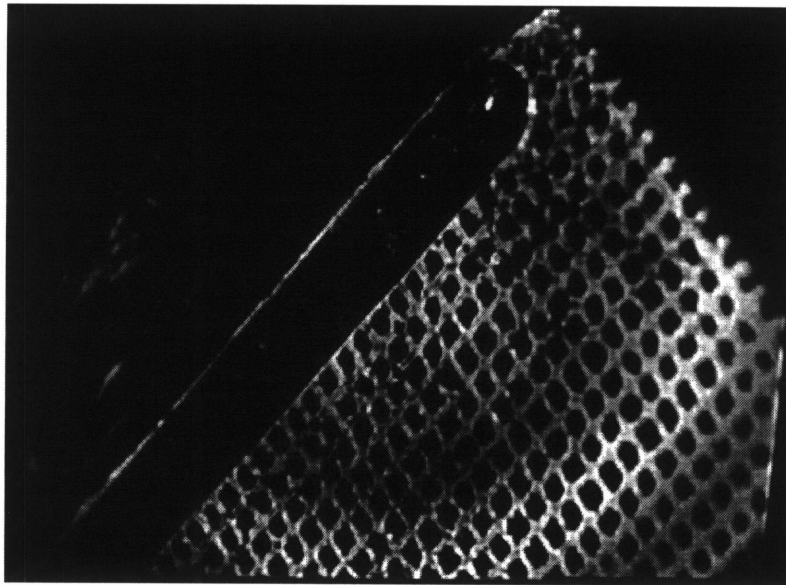
Point C1



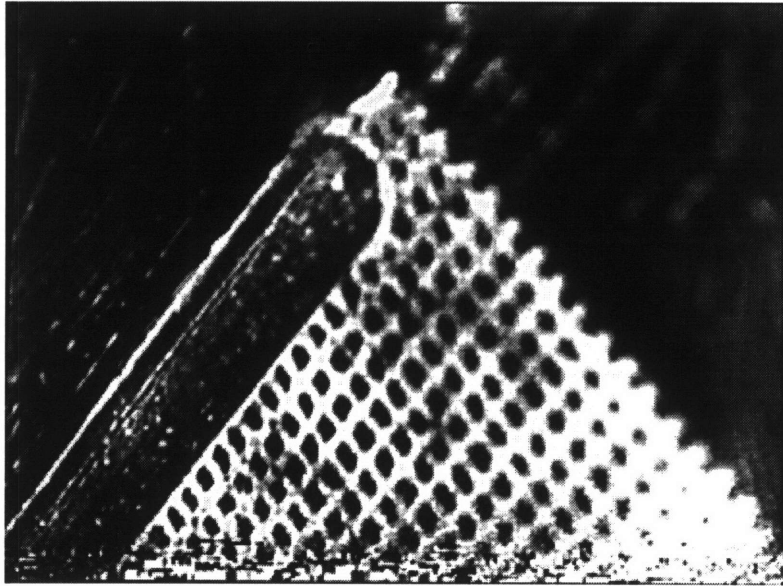
Point D1



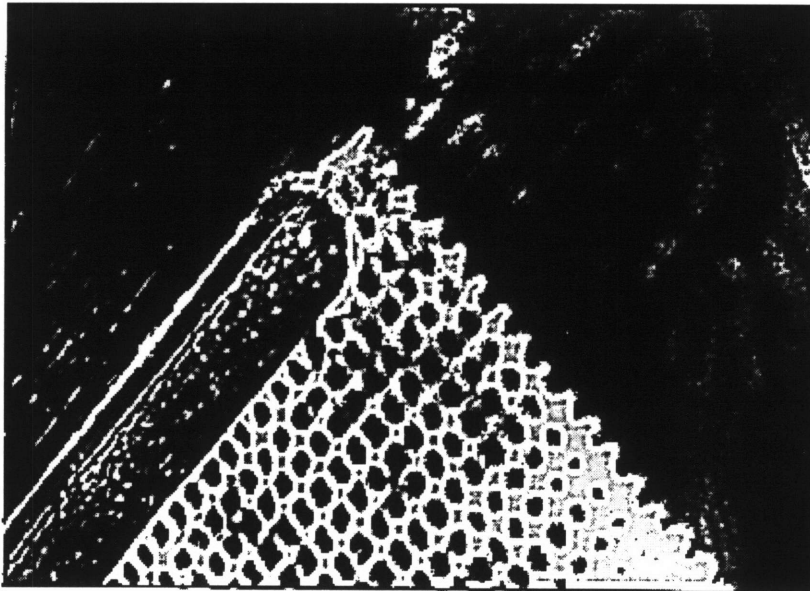
Point E1



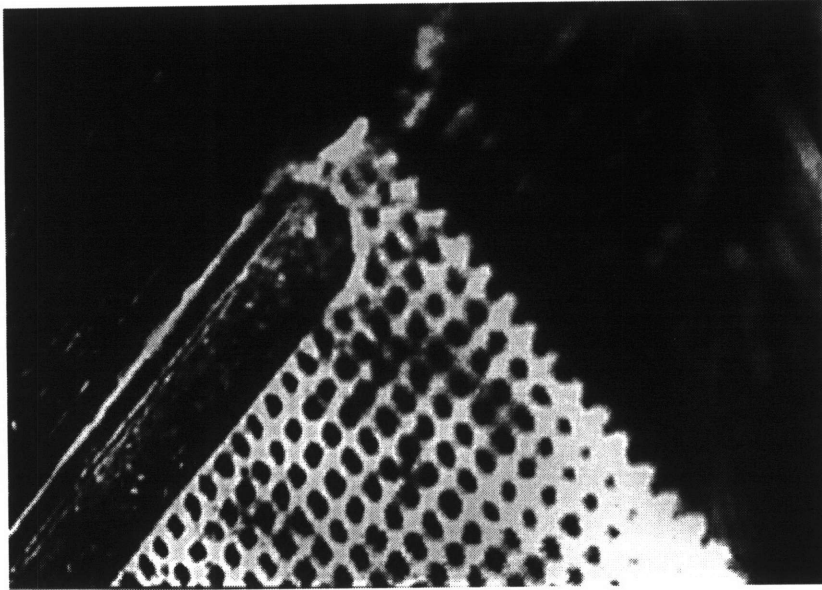
Point F1



Point G1

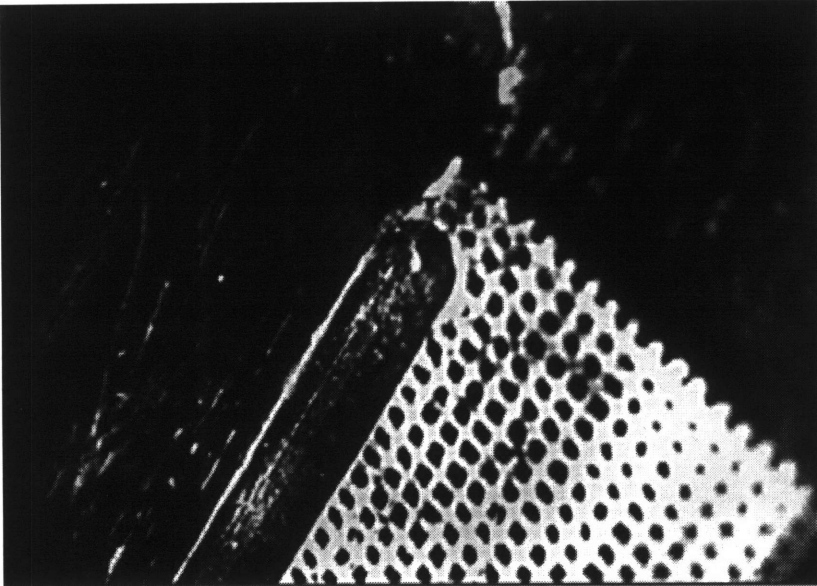


Point H1

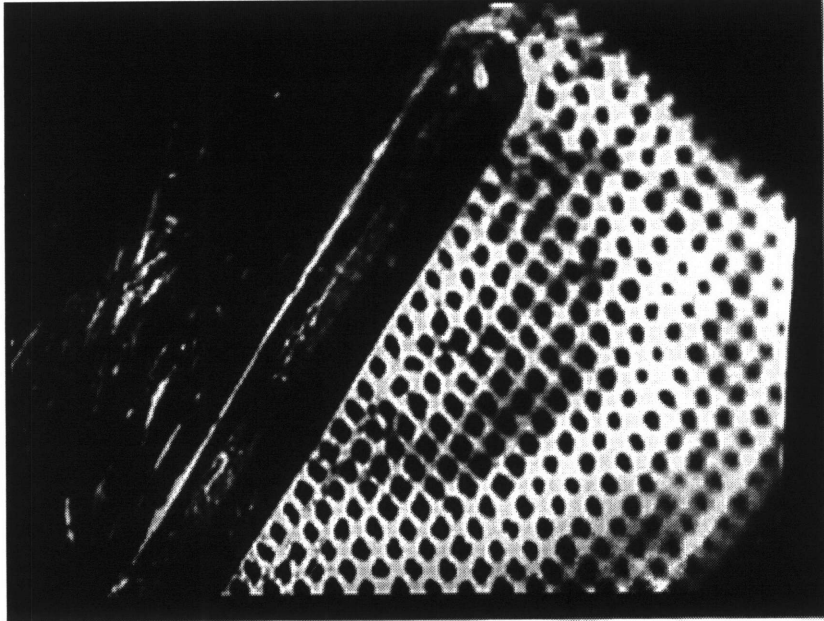


Point I1

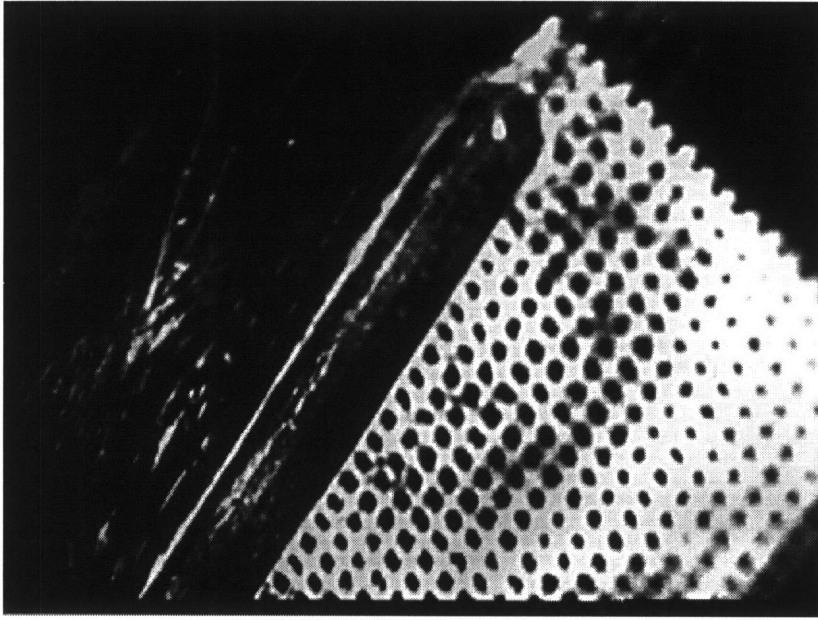
Second Cycle Load



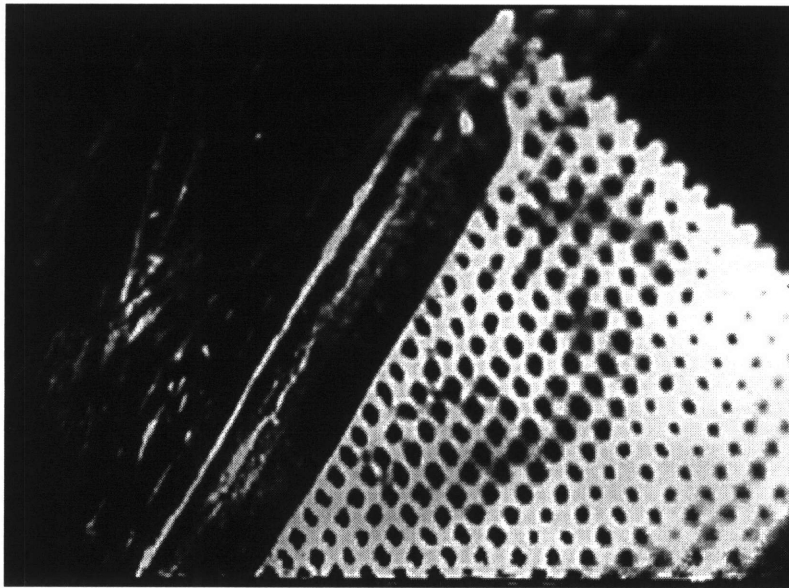
Point A2



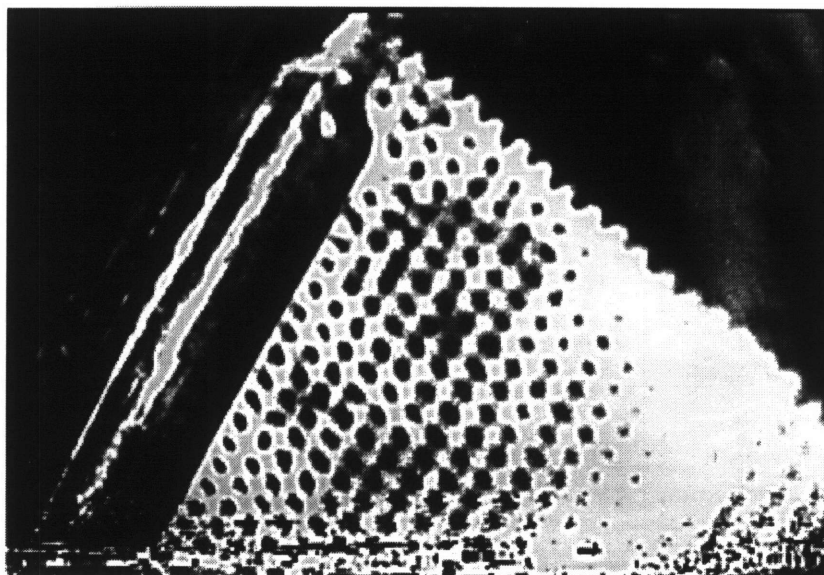
Point B2



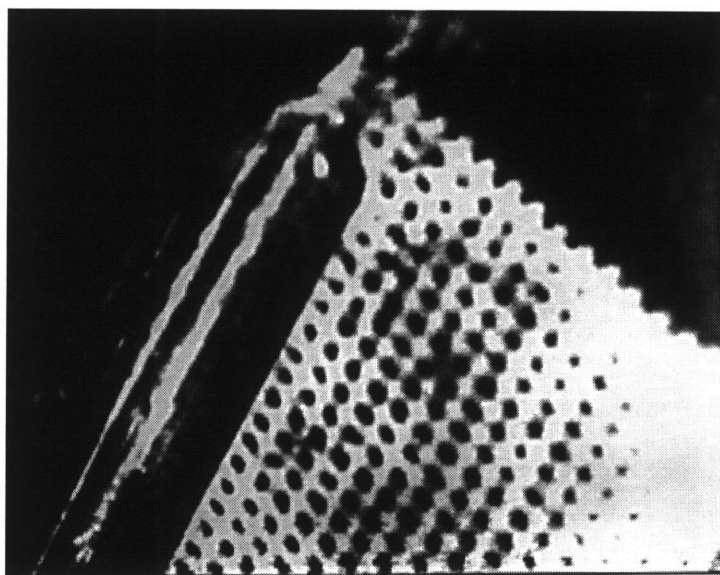
Point C2



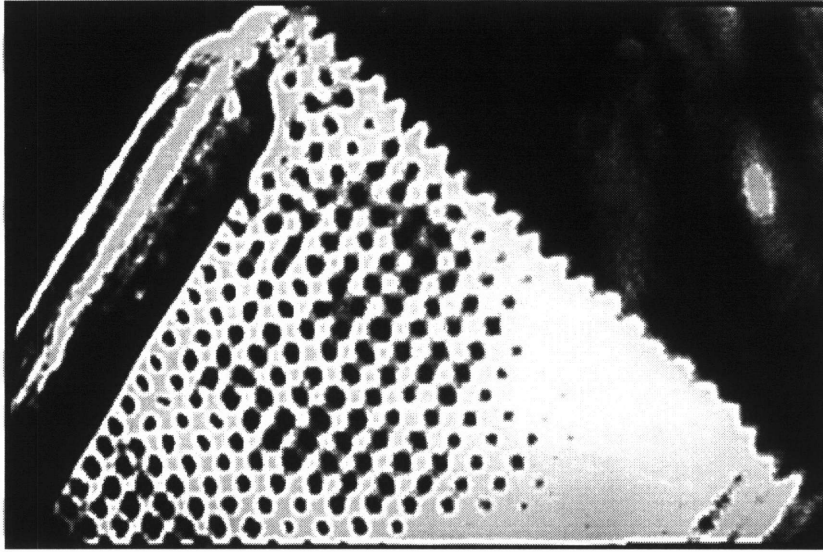
Point D2



Point E2

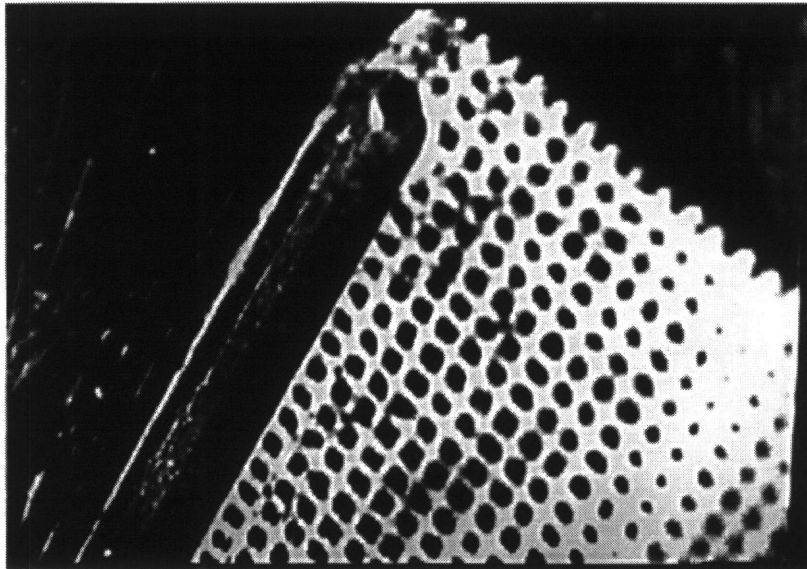


Point F2

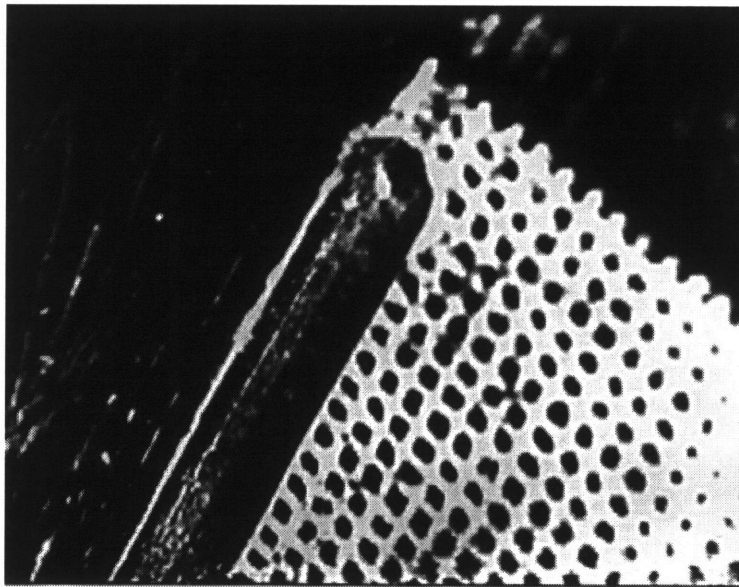


Point G2

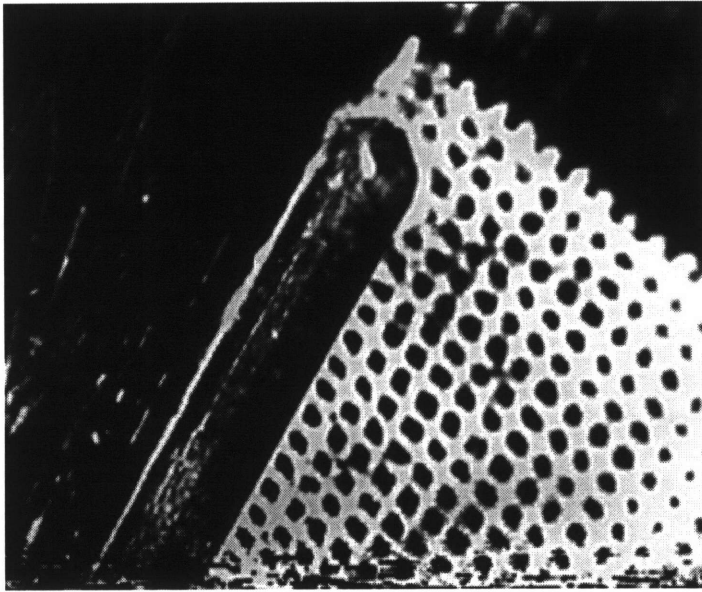
Third cycle Load



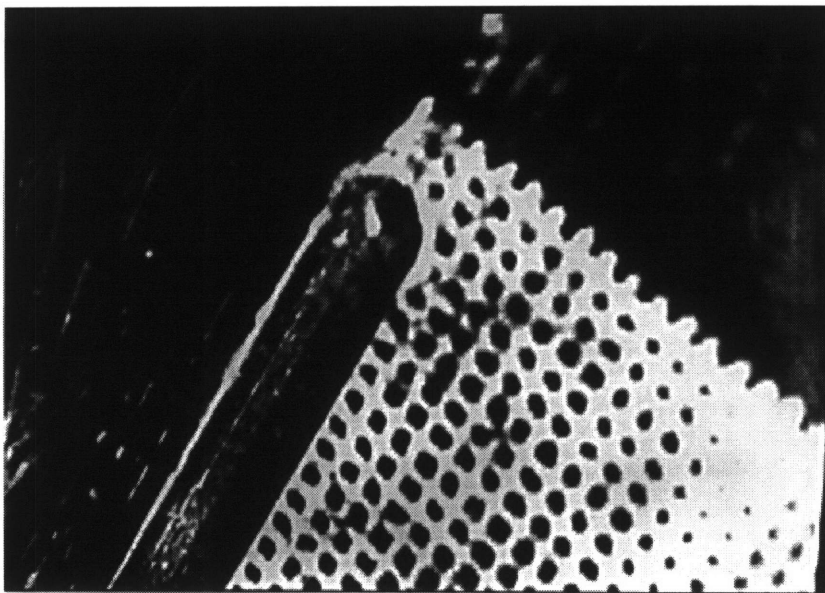
Point A3



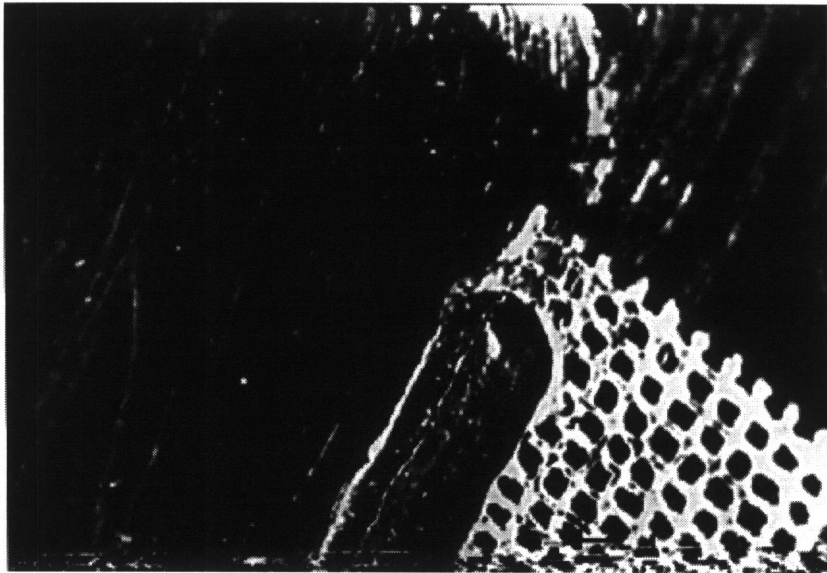
Point B3



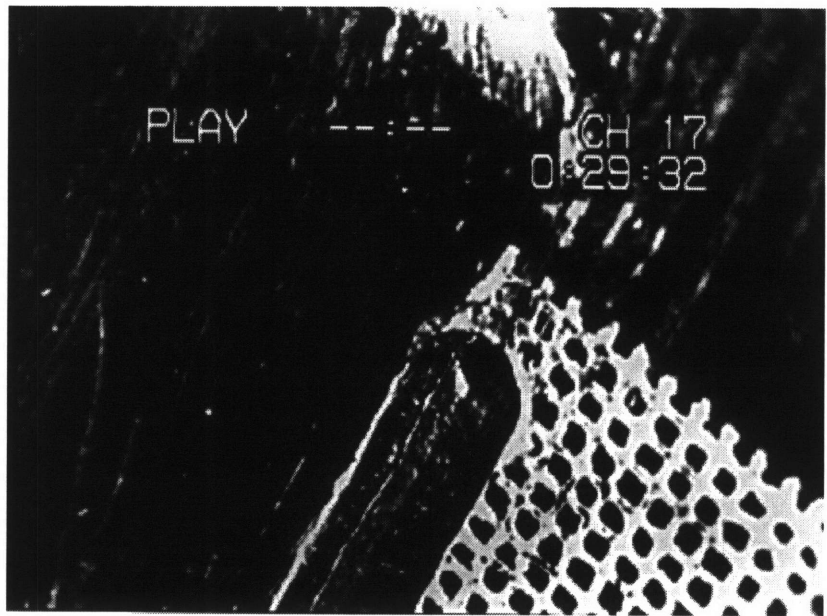
Point C3



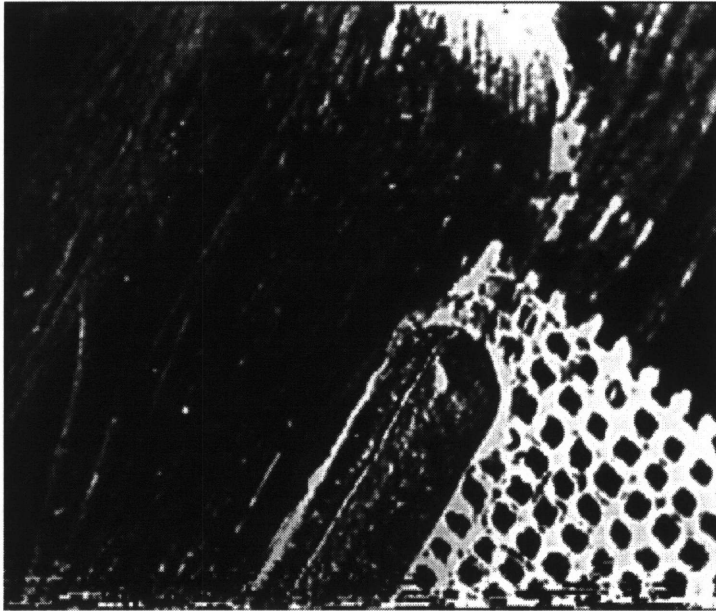
Point D3



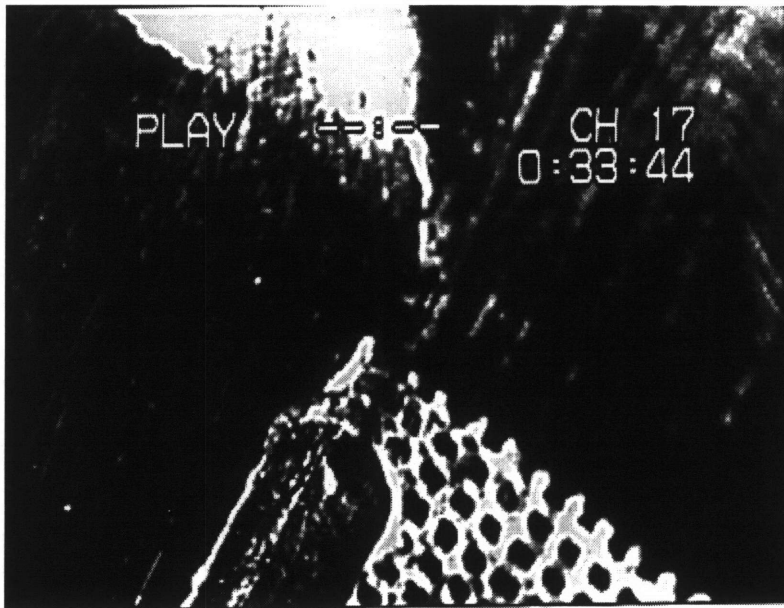
Point F3



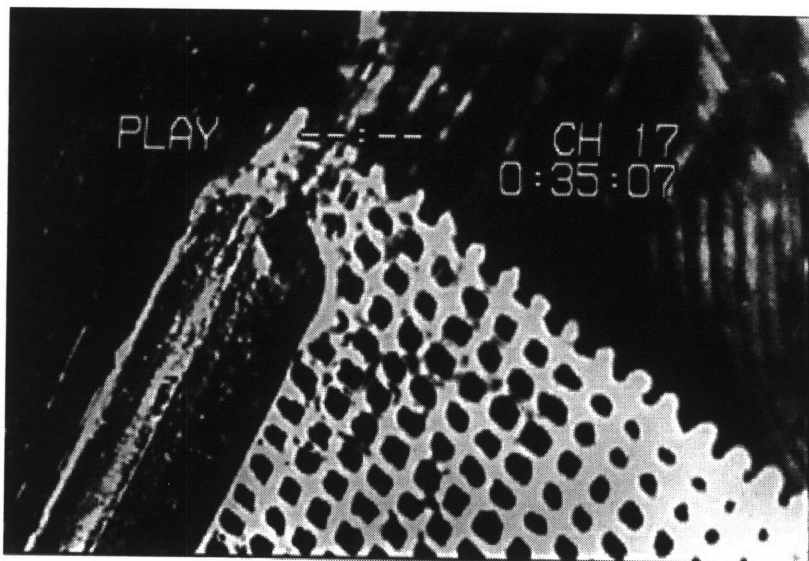
Point G3



Point H3

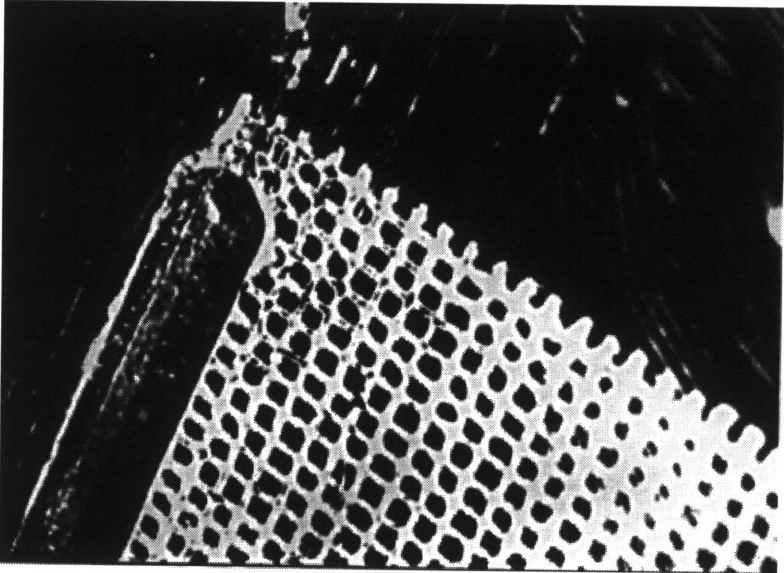


Point I3

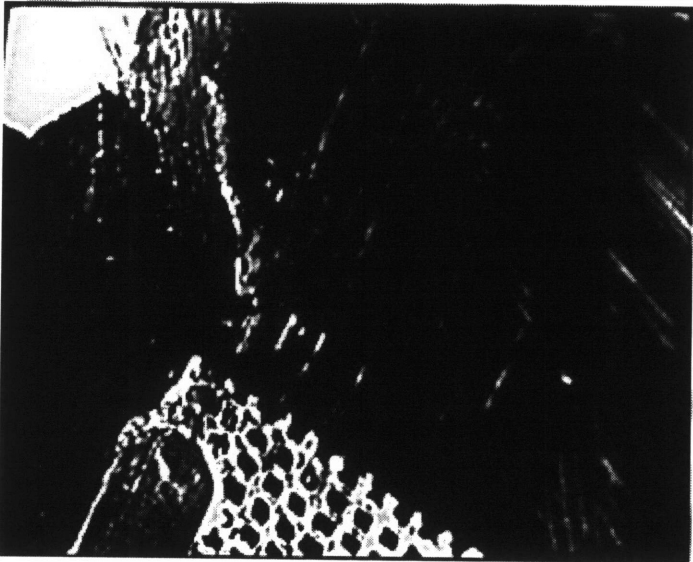


Point J3

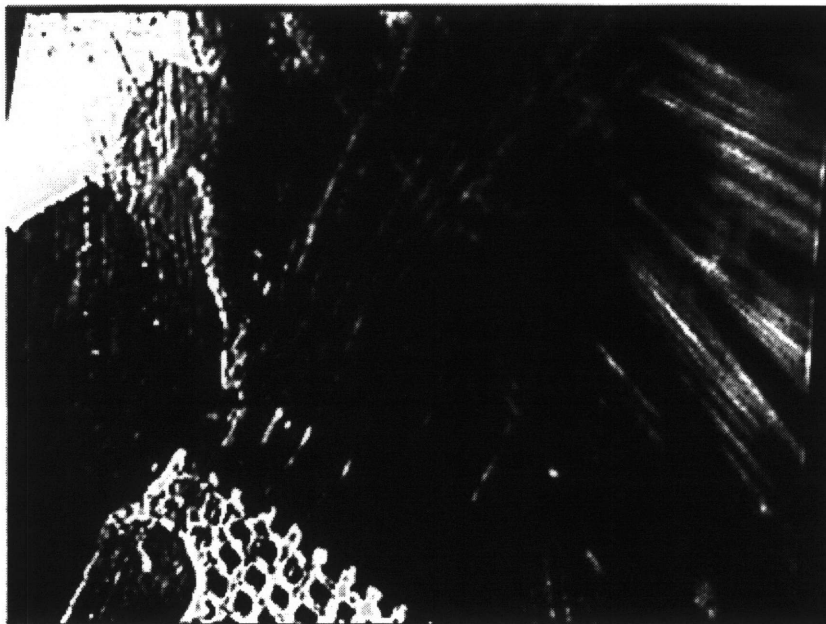
Forth cycle load



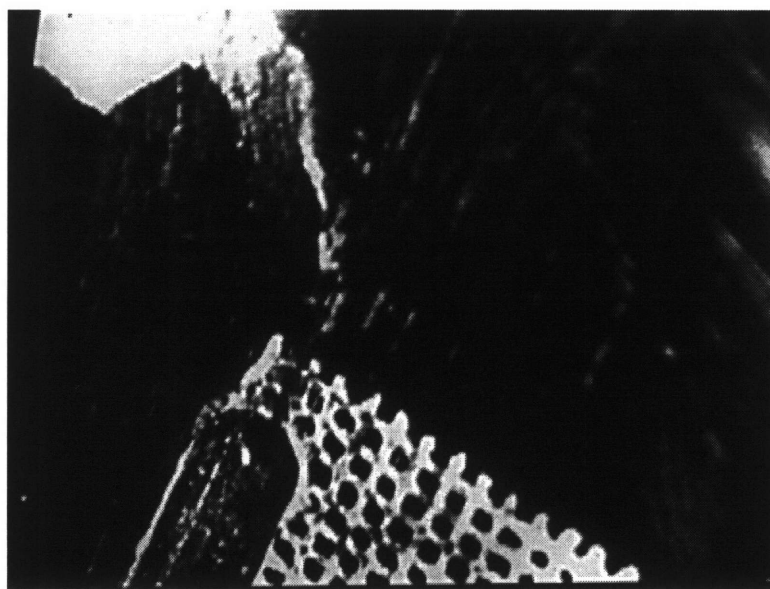
Point A4



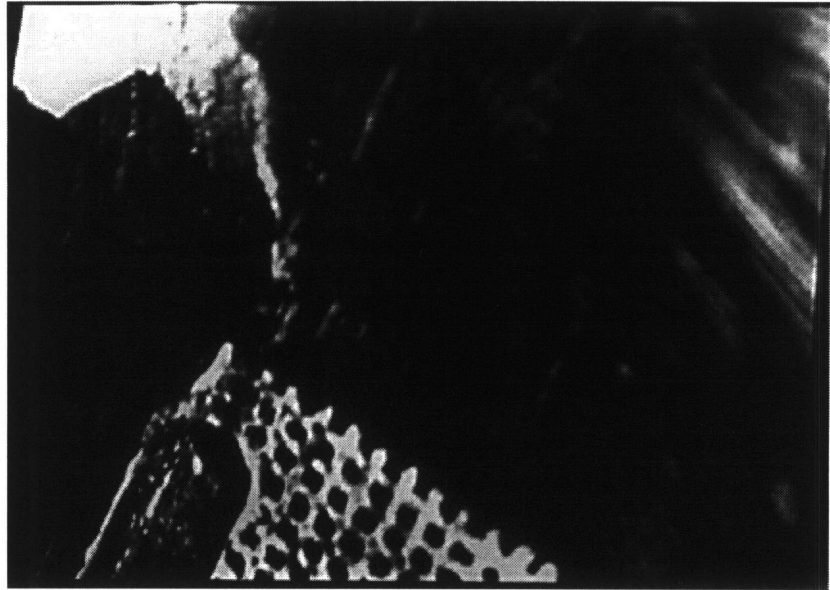
Point B4



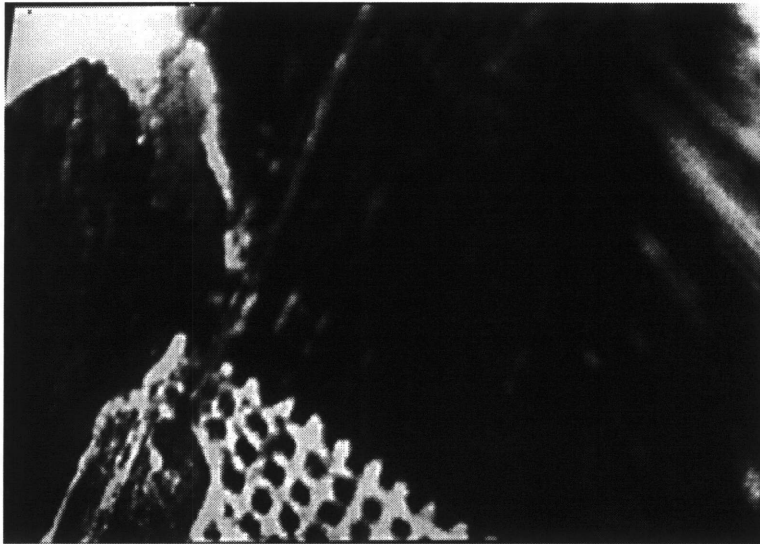
Point C4



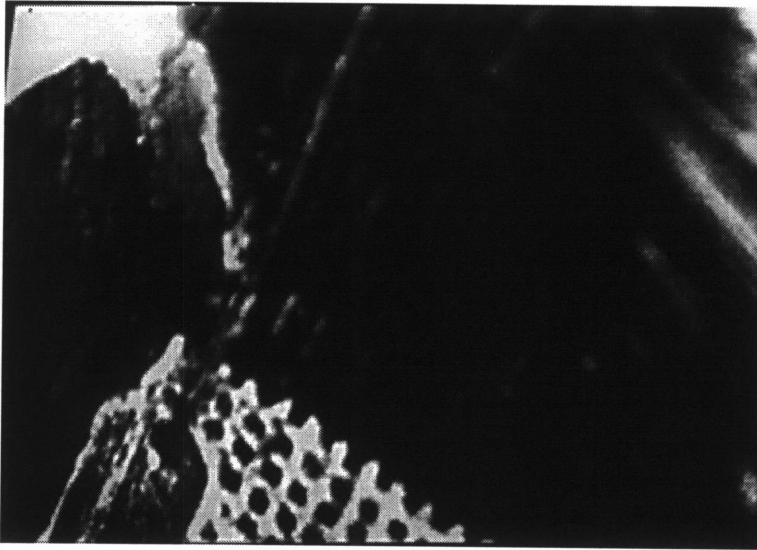
Point D4



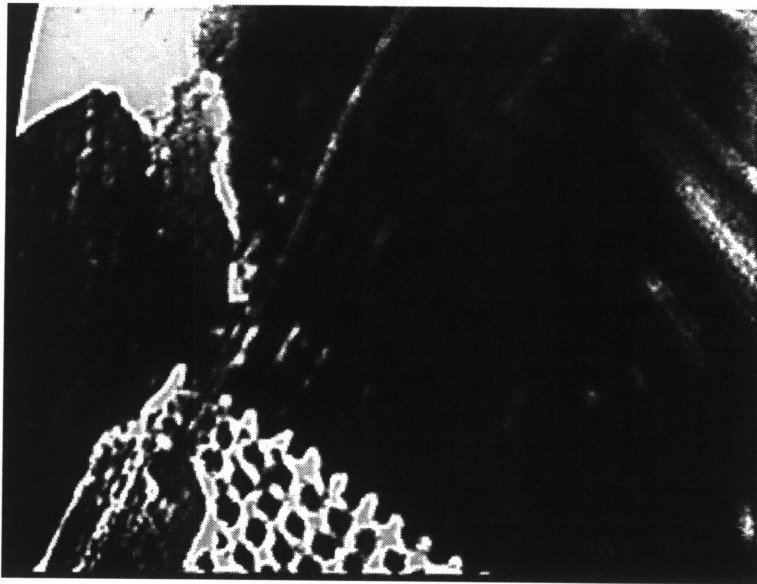
Point F4



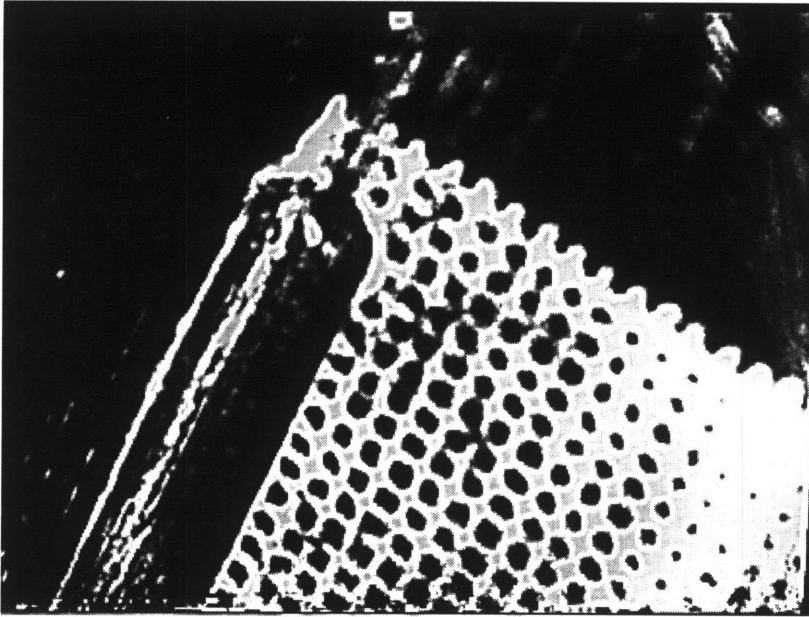
Point G4



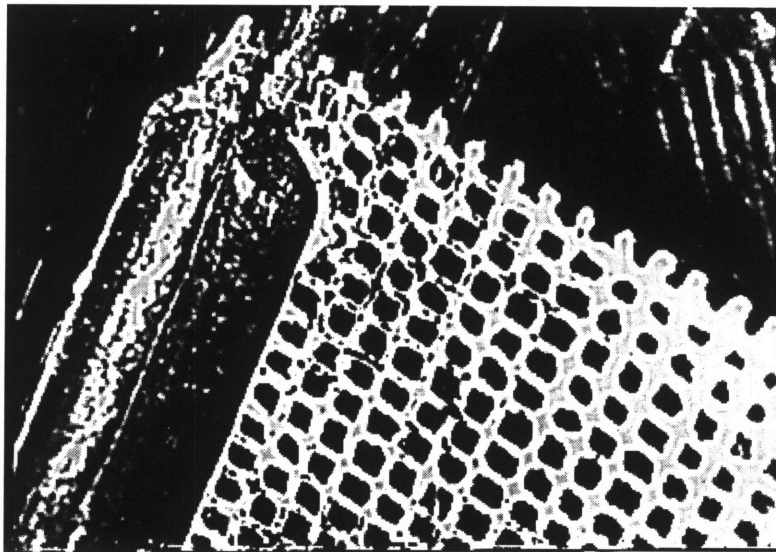
Point H4



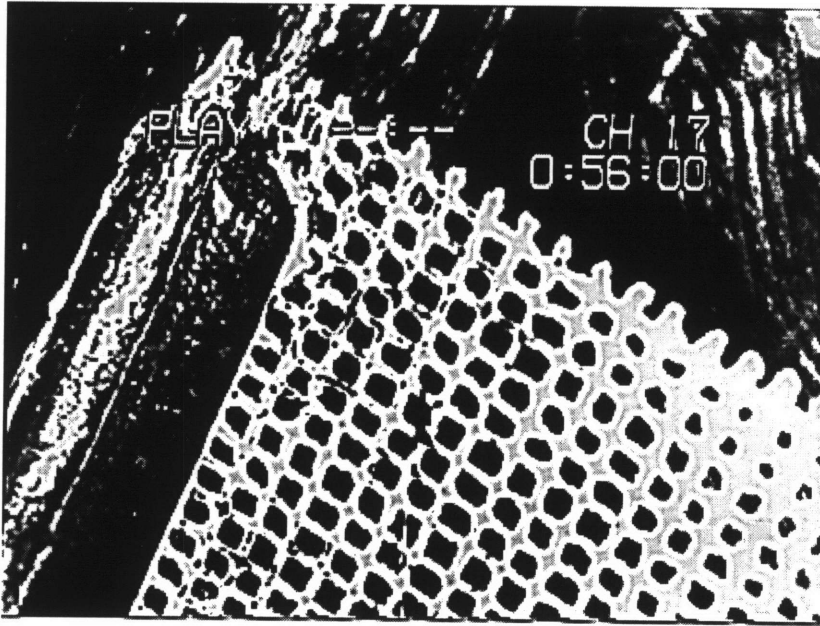
Point I4



Point J4



Point K4



Point L4

Final stage after break

